

RECONFIGURABLE RF/MICROWAVE AND MILLIMETERWAVE CIRCUITS
USING THIN FILMS OF BARIUM STRONTIUM TITANATE AND PHASE
CHANGE MATERIALS

Dissertation

Submitted to

The School of Engineering of the
UNIVERSITY OF DAYTON

In Partial Fulfillment of the Requirements for

The Degree of

Doctor of Philosophy in Engineering

By

Kaushik Annam

Dayton, Ohio

December 2021



**University of
Dayton**

RECONFIGURABLE RF/MICROWAVE AND MILLIMETERWAVE CIRCUITS
USING THIN FILMS OF BARIUM STRONTIUM TITANATE AND PHASE
CHANGE MATERIALS

Name: Annam, Kaushik

APPROVED BY:

Guru Subramanyam, Ph.D.
Advisory Committee Chairman
Professor
Department of Electrical and Computer
Engineering

Andrew Sarangan, Ph.D.
Committee Member
Professor
Department of Electro Optics
and Photonics

Fahima Ouchen, Ph.D.
Committee Member
Adjunct Professor
Department of Electrical and Computer
Engineering

Vamsy Chodavarapu, Ph.D., P.E.
Committee Member
Associate Professor
Department of Electrical and
Computer Engineering

Weisong Wang, Ph.D.
Committee Member
Assistant Professor
Department of Electrical Engineering
Wright State University – Lake Campus

Robert Wilkens, Ph.D., P.E.
Associate Dean for Research and
Innovation
Professor
School of Engineering

Margaret F. Pinnell, Ph.D.
Interim Dean, School of Engineering

© Copyright by
Kaushik Annam
All rights reserved
2021

ABSTRACT

RECONFIGURABLE RF/MICROWAVE AND MILLIMETERWAVE CIRCUITS
USING THIN FILMS OF BARIUM STRONTIUM TITANATE AND PHASE
CHANGE MATERIALS

Name: Annam, Kaushik
University of Dayton

Advisor: Dr. Guru Subramanyam

Tunable passive rf/microwave devices are the building blocks of reconfigurable electronics. Barium Strontium Titanate (BST) based tunable devices are being studied over for two decades now and this technology is very mature. Researchers have tried different material compositions, substrates, and deposition techniques to increase the tunability of the BST thin films. Researchers have also demonstrated reconfigurable devices at rf/microwave frequencies, however with only limited applications.

In this work a novel technique of integrating high tunable dielectric materials such as BST, in combination with a germanium telluride (GeTe) phase change material (PCM) is demonstrated. Integrating phase change material thin films with BST thin films gives additional tuning. The idea of integrating PCM with BST initiates a new era of reconfigurable electronics. These new devices can be implemented with very less fabrication constraints.

A low loss rf switch with 0.23 dB insertion loss and more than 19.75 dB isolation at 15 GHz is presented.

An MIM varactor with increased tunability of about 6.3:1 (57%) is achieved, compared to 4:1 tuning of conventional varactor by integration of BST and GeTe thin films. Analog phase shifters with 360° phase shift in the frequency range of 24 GHz to 50 GHz has been demonstrated with good figure of merit (FOM) of 46.64 degrees/dB at 50 GHz and 19.07 degrees/dB at 24 GHz using MIM varactors with BST and GeTe thin films and 319° phase shift at 24 GHz with FOM 12.8 degrees/dB and more than 360° phase shift at 50 GHz with $FOM_{(2V-10V)} > 21.5$ degrees/dB using MIM varactor with only BST thin films.

A defected ground structure (DGS) band stop filter with enhanced band-rejection behavior with a notch depth of -39.64 dB @ 27.75 GHz by cascading two-unit cells using BST thin films is achieved. Tunable DGS band stop filters were demonstrated by integration of BST and GeTe with 2.25 GHz tunability from 30.75 GHz to 33 GHz (7.32%) using a single filter and 3.25 GHz tuning from 27 GHz to 30.25 GHz (12.04%) by cascading two filters.

Dedicated to my family

ACKNOWLEDGEMENTS

First and foremost, I would like to express gratitude to my advisor Dr. Guru Subramanyam, whole heartedly, for all the support, guidance, encouragement, and suggestions he has given me over the years. He had always given me the freedom to implement new thoughts and work at my own pace.

I would like to thank Dr. Weisong and Dr. Eunsung for their invaluable assistance with my research. Dr. Weisong gave me lot of new ideas and feedback on my research. He is also part of my committee. Dr. Eunsung fabricated all my samples, and he was always willing to share his knowledge and taught me the different deposition techniques.

I would also like to express my gratitude to my other committee members, Dr. Andrew Sarangan, Dr. Vamsy Chodavarapu, and Dr. Fahima Ouchen, for agreeing to serve on my committee and examine my work. I have taken their classes and learnt a lot from their lectures.

I also would like to thank all the other group members Birhanu Alemayehu, Malia Harvey, Jincheng Zhao, Austin Shallcross, Adam Miesle and Dr. Liangyu Li, for all the help and support. I had lot of fun working with them.

Finally, I would like to thank to my parents and my brother for their unending love, support, and encouragement throughout my life. This achievement would not be possible without their encouragement and support.

TABLE OF CONTENTS

ABSTRACT	iv
DEDICATION	vi
ACKNOWLEDGEMENTS	vii
LIST OF FIGURES	xi
LIST OF TABLES	xvi
CHAPTER 1 INTRODUCTION	1
1.1 Motivation	1
1.2 Objectives	5
1.3 Contributions	6
1.4 Outline	9
CHAPTER 2 REVIEW OF BARIUM STRONTIUM TITANATE (BST) THIN FILMS AND APPLICATIONS	10
2.1 Introduction	10
2.2 Barium Strontium Titanate (BST)	10
2.3 General Properties of Ferroelectric Material	11
2.4 Crystal Structure of BST	13
2.5 Deposition Techniques and Process	14
2.6 Thin vs Thick Films	18
2.7 Applications of BST Thin Films	19
2.8 Equivalent Circuit Model	26

CHAPTER 3 OVERVIEW OF GERMANIUM TELLURIDE (GeTe) AND ITS APPLICATIONS	29
3.1 Introduction.....	29
3.2 Deposition.....	31
3.3 Phase Transitions.....	32
3.4 Crystallization	34
3.5 Amorphization.....	41
3.6 RF Switch	44
3.7 Measurement Setup	48
3.8 Measurement Procedure	50
3.9 Circuit Model.....	52
CHAPTER 4 ANALOG PHASE SHIFTERS.....	53
4.1 Introduction.....	53
4.2 2 μm x 2 μm Varactor	55
4.3 Dual Top 2 μm x 2 μm varactor	58
4.4 Phase Shifter using Dual Top Varactor	63
4.5 Phase Shifter with PCM.....	66
CHAPTER 5 TUNABLE BAND STOP FILTER DESIGN USING DEFECTED GROUND STRUCTURE	72
5.1. Introduction.....	72
5.2 Dumbbell DGS.....	75
5.2.1 Influence of the Square Lattice “axb”	76
5.2.2 Influence of the Gap Distance “g”	77

5.3 U-Slot DGS.....	78
5.3.1 Influence of Length “L”	79
5.3.2 Influence of Distance “d”	80
5.3.3 Influence of Width of the Slot “g”	81
5.4 Dumbbell DGS using CPW.....	82
5.5 U-slot DGS using CPW.....	87
5.6 Dumbbell U-slot DGS	90
5.7 Dumbbell U-slot DGS Cascade	93
5.8 Dumbbell U-slot DGS Using BST and PCM	97
5.9 Dumbbell U-slot DGS Using BST and PCM Cascade	104
SUMMARY AND CONCLUSIONS	109
FUTURE WORK.....	111
REFERENCES.....	112

LIST OF FIGURES

Fig.1.1 5G mmWave band usage in different countries	2
Fig.1.2 Beamforming using phased array antenna	4
Fig.1.3 Rf front end module of a mobile device	5
Fig.2.1 Dielectric permittivity vs. temperature of ferroelectric material	12
Fig.2.2 Crystal structure in ferroelectric and paraelectric phase of BST.....	13
Fig.2.3 Schematic diagram of a typical PLD system.....	16
Fig.2.4 Neocera Pioneer 180 large area PLD system in our lab.....	17
Fig.2.5 Variation of the dielectric constant of thick film vs. thin film as a function of temperature	19
Fig.2.6 (a) Interdigitated capacitor (b) Parallel plate capacitor	22
Fig.2.7 (a) Bottom metal (b) Top metal (c) 5 μm x 5 μm varactor	23
Fig.2.8 Measured S_{21} magnitude of a 5 μm x 5 μm varactor.....	24
Fig.2.9 Measured S_{21} phase of a 5 μm x 5 μm varactor.....	24
Fig.2.10 Simulated S_{21} magnitude of a 5 μm x 5 μm varactor.....	25
Fig.2.11 Simulated S_{21} phase of a 5 μm x 5 μm varactor.....	25
Fig.2.12 Equivalent circuit model for the shunt varactor device.....	26
Fig.2.13 Dielectric properties of 0.25 μm BST thin film on sapphire substrate ...	28
Fig.3.1 Heat profiles used for transition to each state	33
Fig.3.2 XRD patterns at different temperatures	34
Fig.3.3 SEM images of samples annealed at different temperatures (a) 220 $^{\circ}\text{C}$ (b) 240 $^{\circ}\text{C}$ and (c) 260 $^{\circ}\text{C}$	35

Fig.3.4 XRD patterns of the as deposited GeTe film and the films annealed at different temperatures	36
Fig.3.5 Atomic force microscopy (AFM) images of GeTe films annealed at a) 240 °C b) 260 °C c) 280 °C d) 350 °C	36
Fig.3.6 XRD pattern of GeTe ₄ film	37
Fig.3.7 XRD spectra for a) C-GeTe annealed in N ₂ b) C-GeTe annealed in air..	39
Fig.3.8 XRD spectra for a) R-GeTe annealed in N ₂ b) R-GeTe annealed in air..	39
Fig.3.9 Temperature vs. resistivity plot	40
Fig.3.10 DC test structure	41
Fig.3.11 GeTe 250 nm as deposited samples exposed to CO ₂ laser at different laser energies	43
Fig.3.12 Infrared transmission properties of (a) Sapphire, (b) Ammonia, and (c) TMAI:NH ₃ adduct, near room temperature	44
Fig.3.13 RF switch (a) with heater coil (b) without heater coil (c) 5µm gap switch without heater coil on wafer	46
Fig.3.14 Fabrication procedure for rf switch	47
Fig.3.15 Measurement setup using GSG probes	48
Fig.3.16 (a) GSG probe (b) calibration standards	49
Fig.3.17 S ₂₁ magnitude ON state	51
Fig.3.18 S ₂₁ magnitude OFF state	51
Fig.3.19 Circuit model shown for 10 µm gap switch in the amorphous state	52
Fig.4.1 2 µm x 2 µm Varactor.....	56

Fig.4.2 Measured S_{21} magnitude of a $2 \mu\text{m} \times 2 \mu\text{m}$ varactor	56
Fig.4.3 Measured S_{21} phase of a $2 \mu\text{m} \times 2 \mu\text{m}$ varactor	57
Fig.4.4 Dual top $2 \mu\text{m} \times 2 \mu\text{m}$ varactor.....	58
Fig.4.5 Measured S_{21} magnitude of a dual top $2 \mu\text{m} \times 2 \mu\text{m}$ varactor	59
Fig.4.6 Measured S_{21} phase of a dual top $2 \mu\text{m} \times 2 \mu\text{m}$ varactor	59
Fig.4.7 Varactor Devices (a) Dual Bottom (b) Dual Top and Bottom (c) Triple Top (d) Triple Bottom	62
Fig.4.8 $3 \mu\text{m} \times 3 \mu\text{m}$ dual top varactor cascade 10 phase shifter	63
Fig.4.9 Measured S_{21} magnitude of dual top $3 \mu\text{m} \times 3 \mu\text{m}$ cascade 10 phase shifter	63
Fig.4.10 Measured S_{21} phase of dual top $3 \mu\text{m} \times 3 \mu\text{m}$ cascade 10 phase shifter	64
Fig 4.11 (a) Modified $3 \times 3 \mu\text{m}^2$ varactor with GeTe (b) magnified drop out	67
Fig.4.12 Measured S_{21} magnitude of dual top $3 \mu\text{m} \times 3 \mu\text{m}$ varactor with PCM	67
Fig.4.13 Measured S_{21} phase of dual top $3 \mu\text{m} \times 3 \mu\text{m}$ varactor with PCM.....	68
Fig.4.14 Dual top $3 \mu\text{m} \times 3 \mu\text{m}$ varactor with PCM cascade 10 phase shifter	69
Fig.4.15 Measured S_{21} magnitude of dual top $3 \mu\text{m} \times 3 \mu\text{m}$ varactor with PCM cascade 10 phase shifter	69
Fig.4.16 Measured S_{21} phase of dual top $3 \mu\text{m} \times 3 \mu\text{m}$ varactor with PCM cascade 10 phase shifter	70
Fig.5.1 Dumbbell DGS on microstrip line	75
Fig.5.2 Influence of rectangular lattice dimension	76

Fig.5.3 Influence of gap distance	78
Fig.5.4 U-slot DGS on microstrip line	79
Fig.5.5 Influence of length L on frequency response of u-slot	80
Fig.5.6 Influence of distance d on frequency response of u-slot	81
Fig.5.7 Influence of width of g on frequency response of u-Slot	82
Fig.5.8 Dumbbell DGS on CPW line	83
Fig.5.9 Simulated frequency response of dumbbell DGS	84
Fig.5.10 Measured frequency response of dumbbell DGS	85
Fig.5.11 Simulated vs. measured S_{21} frequency response of dumbbell DGS	86
Fig.5.12 Circuit model for dumbbell DGS	86
Fig.5.13 U-slot DGS on CPW	87
Fig.5.14 Simulated frequency response of u-slot DGS	88
Fig.5.15 Measured frequency response of u-slot DGS	88
Fig.5.16 Simulated vs. measured S_{21} frequency response of u-slot DGS	89
Fig.5.17 Circuit model for u-slot DGS	90
Fig.5.18 Dumbbell u-slot DGS	91
Fig.5.19 Simulated frequency response of dumbbell u-slot DGS	91
Fig.5.20 Measured frequency response of dumbbell u-slot DGS	92
Fig.5.21 Simulated vs. measured S_{21} frequency response of dumbbell u-slot DGS	92
Fig.5.22 Circuit model for dumbbell u-slot DGS	93
Fig.5.23 Dumbbell u-slot DGS cascade	94
Fig.5.24 Simulated frequency response of dumbbell u-slot cascade DGS	94

Fig.5.25 Measured frequency response of dumbbell u-slot cascade DGS	95
Fig.5.26 Simulated vs. measured S_{21} frequency response of dumbbell u-slot cascade DGS	95
Fig.5.27 Circuit model for dumbbell u-slot cascade DGS	96
Fig.5.28 Schematic model vs. measured S_{21} frequency response of dumbbell u-slot cascade DGS	97
Fig.5.29 Dumbbell u-slot DGS with PCM	98
Fig.5.30 Simulated frequency response of dumbbell u-slot DGS with PCM (a) amorphous PCM (b) crystalline PCM	99
Fig.5.31 Measured frequency response of dumbbell u-slot DGS with PCM (a) amorphous PCM (b) crystalline PCM	101
Fig.5.32 Simulated vs. measured S_{21} frequency response of dumbbell u-slot DGS with PCM (a) amorphous PCM (b) crystalline PCM	103
Fig.5.33 Circuit model for dumbbell u-slot DGS with PCM	103
Fig.5.34 Dumbbell u-slot DGS with PCM Cascade	104
Fig.5.35 Simulated frequency response of dumbbell u-slot DGS with PCM cascade (a) amorphous PCM (b) crystalline PCM	105
Fig.5.36 Measured frequency response of dumbbell u-slot DGS with PCM cascade (a) amorphous PCM (b) crystalline PCM	106
Fig.5.37 Simulated vs. measured S_{21} frequency response of dumbbell u-slot DGS with PCM cascade (a) amorphous PCM (b) crystalline PCM	107
Fig.5.38 Circuit model for dumbbell u-slot DGS with PCM Cascade	107

LIST OF TABLES

Table.2.1 Summary of the attributes and shortfalls of the various complex oxide thin film growth techniques	15
Table.2.2 Extracted parameters for a 5 μm x 5 μm varactor	27
Table.3.1 Deposition parameters using PLD	32
Table.3.2 Extracted component values for switches with 5,10 and 15 μm gaps	52
Table.4.1 Summary of phase shifters using different technologies	55
Table.4.2 Extracted parameters for a 2 μm x 2 μm varactor	57
Table.4.3 Extracted parameters for a dual top 2 μm x 2 μm varactor	60
Table.4.4 Insertion loss of modified varactors @ 10 V DC Bias	60
Table.4.5 Summary of results of dual top 3 μm x 3 μm cascade 10 phase shifter @ 24 GHz	65
Table.4.6 Summary of results of dual top 3 μm x 3 μm cascade 10 phase shifter @ 50 GHz	66
Table.4.7 Extracted parameters of dual top 3 μm x 3 μm varactor with PCM	68
Table.4.8 Summary of results of dual top 3 μm x 3 μm varactor with PCM cascade 10 phase shifter	70
Table.4.9 Comparison of FOM of the phase shifters with and without PCM	71

CHAPTER 1

INTRODUCTION

1.1 Motivation

In the world of communications, wireless communication is the fastest developing technology. The growing popularity of wireless technology is driving up demand for spectrum, particularly in the sectors of wireless communication, navigation, and internet of things (IOT). The concept of wireless communications dates to 1897, when Guglielmo Marconi successfully demonstrated wireless telegraphy by transmitting electro-magnetic waves for a small distance of 100 meters. This demonstration cleared the door for radio communication. The word “Radio” is derived from the word “radiant energy”. After this successful transmission of radio signals trans-Atlantic radio transmission had been established by early 1900’s with Marconi successfully transmitting Morse code messages. Since then, wireless communication and system technology has improved significantly, allowing transmissions over longer distances at lower costs and with fewer expensive devices.

Initially, because of limited number of users and applications, the cellular mobile communications prior to 5G takes place in sub-3 GHz band i.e., LTE frequency band. Ideally LTE can provide speeds up to 300 Mb/s, which has become too crowded to accommodate increasing mobile data traffic. Thus, 5G has evolved. The evolution of 5G has created a challenge to many fields in electronics. One such field is microwave electronics. The spectrum allocation of 5G bands is

in two sets. The Sub-6 GHz, which ranges from 450 MHz to 6 GHz. This frequency band includes LTE frequency range (700 MHz to 2.7 GHz). And the mmWave frequency band from 24.25 GHz to 52.6 GHz. Due to the availability of commercial technology and existing licensed LTE bands the network operators using carrier aggregation for both time division duplex (TDD) and frequency domain duplex (FDD) technologies have started services in the sub-6 GHz frequency bands. However, due to lack of commercial technology and complex design challenges the higher frequency band is still unexplored. Fig.1.1 shows the licensed high frequency 5G spectrum bands in different countries.

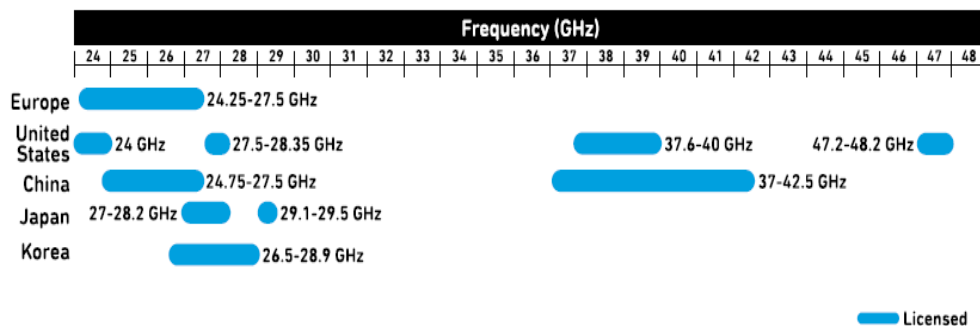


Fig.1.1 5G mmWave band usage in different countries [1]

Conventional CMOS based active and passive devices have various parasitics involved especially at microwave and mmWave frequencies which in turn create modeling issues of active components, as well as layout design issues [2]. This creates a need to explore new technologies for high frequency devices. Using different thin film materials, we can achieve reconfigurable devices. In this dissertation, reconfigurable electronics such as switch, phase shifter, band stop filter at high frequencies are demonstrated.

Installation of base station has always been a tedious task, especially at the 5G frequencies where the signal strength decays fast. Beam steering or beamforming shown in fig.1.2., is the crucial stage for 5G base stations. At higher frequencies while all the electronic components are very small in size, commercially available phase shifters are bulky and expensive, which increases the overall size and cost of the base station installation. Phase shifters with good Figure of Merit (FOM defined by ratio of the maximum phase shift in degrees to the maximum insertion loss) at high frequencies are currently not available, especially at higher frequencies where the new 5G spectrum is licensed. Up to now, several researchers have been working on the phase shifters using MEMS [3], diodes [4], magnetic nanostructures [5], ferrites [6]-[7] and ferroelectric materials [8]-[12]. Ferroelectric materials-based phase shifters have several advantages over ferrite and semiconductor-based phase shifter such as high speed, low losses, and high-power handling capability. The problem with MEMS based phase shifters are they are bulky and expensive as it needs special packaging. Phase shifters with 360° phase shift for a wide frequency spectrum would reduce the number of base stations as the signal can be directed in any angle which in turn reduces the cost.

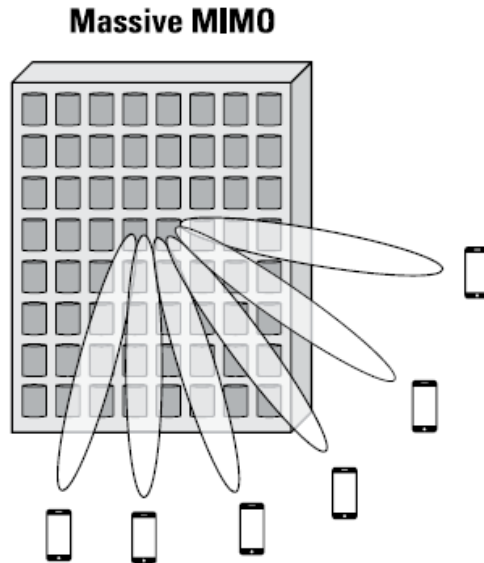


Fig.1.2 Beamforming using phased array antenna [13]

Other devices that play crucial role in the operation of communication systems are switches and filters. Fig.1.3. shows a generic rf front end module of a mobile device. A simple module requires several switches and filters, especially at 5G frequencies more stringent specs needs to be met. Filters are used to remove unwanted components and reduce the interference and noise. Commercially available acoustic filters such as SAW/BAW filters can address frequencies up to 6GHz and requires complex fabrication process. Though the semiconductor-based switches like CMOS silicon-on-insulator (SOI) and silicon-on-sapphire (SOS), GaAs MMIC with multi pole multi throw (MPMT) configuration with high speed and low power consumption are commercially available, however the power handling capacity and the complex fabrication are the major drawbacks. To increase the power handling capacity of a CMOS switch, number of stacks of FET's are increased [14]. However, this is not an optimal solution as it increases the overall size of the switch and in turn increases cost.

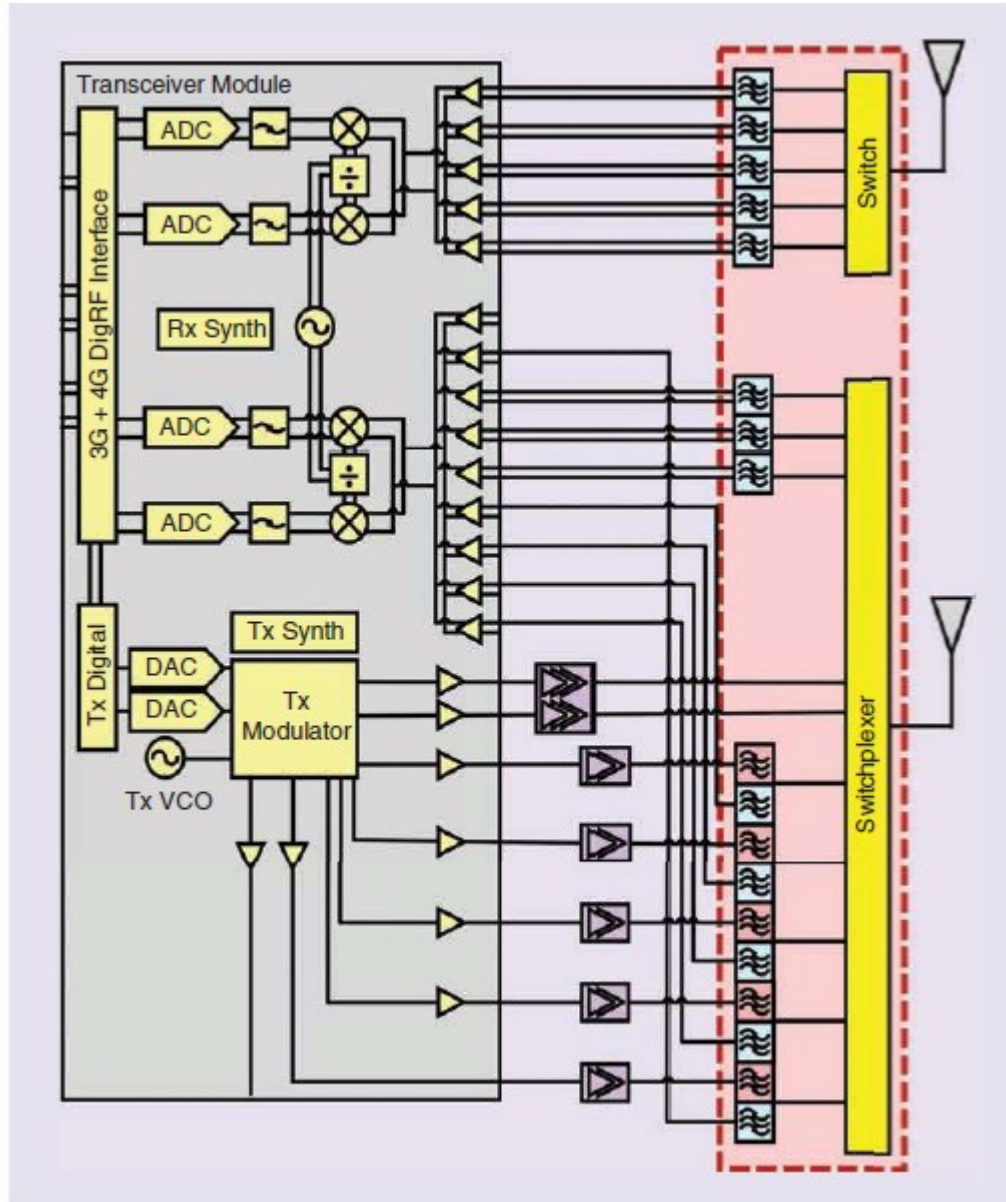


Fig.1.3 Rf front end module of a mobile device [15]

1.2 Objectives

As mentioned earlier, semiconductor devices have major drawbacks for implementation at higher frequencies. Reconfigurable devices can play a vital role, the number of filters in the RF front end module can be reduced significantly using reconfigurable filters and the complex CMOS switches can be easily replaced by

low loss, low cost and easy to implement devices. This reduces the overall cost, size of the module and provides flexibility and ease in system-level applications. Our group has recently focused on reconfigurable technologies that are both feasible to implement and advantageous to traditional micromachining techniques [16-23]. Though the signal processing is done at an intermediate frequency (IF) in a mobile phone, the receiver circuit still needs high frequency components in order to receive, filter, and down convert the mmWave frequencies of 5G spectrum. The main objectives of the proposed project are:

- Design and demonstrate low insertion loss and high isolation rf/microwave switch with low cost, small size, based on coplanar waveguide transmission line using Germanium Telluride (GeTe) phase change material thin films.
- Integrate high dielectric tunable Barium Strontium Titanate (BST) thin films with germanium telluride thin films to improve the spectrum utilization of reconfigurable circuits.
- To design and demonstrate reconfigurable devices such as phase shifters, and band stop filters using thin films of BST and GeTe.

1.3 Contributions

This dissertation provides designs of tunable passive rf/microwave components, such as a switch, a phase shifter, and a filter using thin films of BST and GeTe PCM. A simple rf/microwave switch with low insertion loss and high isolation is presented. Modified Metal-Insulator-Metal (MIM) varactor designs are implemented by integrating BST and GeTe materials for higher tuning, low losses,

and low control voltages with reduced size for high frequency applications. Phase shifters using modified varactors for low losses and high FOM at high frequency applications are demonstrated. Also, tunable Defected Ground Structure (DGS) band stop filters at higher frequencies are presented with superior tunable stopband performance. GeTe films with five orders of magnitude ratio between the amorphous (high resistance) and crystalline state (low resistance state) were achieved and these thin films are used for additional tuning. The main contributions can be described in detail as follows:

- Low insertion loss of 0.23 dB and high isolation 19.75 dB rf switch at 15 GHz with ease of fabrication and small size up to 15 GHz is implemented.
- Single units of MIM varactors with modified topology using BST and GeTe thin films for higher tuning and low losses with significantly reduced size are designed and characterized. With capacitive tuning ratio of 6.3:1 by applying 0-10 V DC bias with loss tangent under 0.01 up to 50 GHz is achieved.
- Analog phase shifters realized with modified MIM varactors are demonstrated with continuous 360° phase shift for wide frequency range (24 GHz to 50 GHz). With good FOM of <math><46.64</math> degrees/dB at 50GHz and 19.07 degrees/dB at 24 GHz using MIM varactors with BST and GeTe thin films and 319° phase shift at 24GHz with FOM 12.8 degrees/dB and more than 360° phase shift at 50 GHz with $FOM_{(2V-10V)} >21.5</math> degrees/dB using MIM varactor with only BST thin films.$

- Dumbbell U-slot DGS structure is demonstrated on CPW transmission line on top of BST thin film. Two unit cells were cascaded to enhance the band-rejection behavior. The notch depth of -39.64 dB @ 27.75 GHz is achieved. By integrating the DGS with GeTe a tunable stop band characters are demonstrated. A shift in resonance from 30.75 GHz to 33 GHz is seen, a frequency shift of 2.25 GHz is achieved, i.e., 7.32% tuning is achieved using single dumbbell u-slot structure and a shift in resonance from 27 GHz to 30.25 GHz is seen, a frequency shift of about 3.25 GHz is achieved i.e. 12.04% of tuning is achieved by cascading of two unit cells. Which overcomes the problem of high DC bias requirement to tune BST thin films using planar structures.

In conclusion, each of the projects mentioned above has improved performance for reconfigurable rf/microwave and millimeter wave frequency applications.

The related publications so far are listed below:

- K.Annam., D.Spatz., E.Shin., and G.Subramanyam., "Experimental Verification of Microwave Phase Shifters Using Barium Strontium Titanate (BST) Varactors," IEEE National Aerospace and Electronics Conference (NAECON), pp.no – 63-66. July 2019.
- K.Annam., S.K.Khah., S.Dooley., C.Cerny and G.Subramanyam., "Experimental Design of Bandstop Filters Based on Unconventional Defected Ground Structures," Microwave and Optical Technology Letters., vol.58.,no.12.,pp.no 2969-2973., Dec 2016.

Following publications are currently being prepared:

- K.Annam., E.Shin., and G.Subramanyam., “Phase Shifter Circuits in the Millimeter Wave Spectrum”
- K.Annam., E.Shin., and G.Subramanyam., ”Modified Varactor Design for Improved Tuning Using Barium Strontium Titanate and Germanium Telluride Thin Films”
- K.Annam., E.Shin and G.Subramanyam., “Tunable Bandstop Filters Based on Unconventional Defected Ground Structures,”

1.4 Outline

A review of BST thin films and applications are addressed, and a varactor device using BST thin film is presented in chapter 2. Chapter 3 gives the overview and process optimization for Germanium Telluride thin films, crystallization and amorphization techniques used, and rf/microwave switch design using GeTe.

In chapter 4 a new technique for increasing tunability for varactor devices by integrating phase change materials with BST has been demonstrated and phase shifter that provides 360° phase shift for wide range of frequencies (24GHz – 50GHz) has been experimentally verified.

In chapter 5, tunable band stop DGS filters with improved performance and tunability using BST and PCM materials have been demonstrated.

Finally, Summary and conclusion of the dissertation work is given along with scope for future work.

CHAPTER 2
REVIEW OF BARIUM STRONTIUM TITANATE (BST) THIN FILMS AND
APPLICATIONS

2.1 Introduction

The use of high permittivity ferroelectric materials for rf and microwave applications have become a common practice. The need for smaller size, high power handling capability and low-cost frequency and phase agile components is growing, especially at the new 5G mmWave frequencies. The electric field dependent ferroelectric thin film-based varactors, phase shifters, and filters etc. are of primary interest. Barium strontium titanate (BST) ferroelectric thin films are the most popular among this group.

2.2 Barium Strontium Titanate (BST)

$Ba_xSr_{1-x}TiO_3$ is a composite of barium titanate ($BaTiO_3$) and strontium titanate ($SrTiO_3$). Thin films of BST have been investigated for reconfigurable rf and microwave devices for over many years [24-29]. It has an advantage of tunable dielectric constant, i.e., when a dc bias voltage is applied either positive or negative the dielectric permittivity is varied in a non-linear fashion. This tuning can be achieved at room temperature with low power which makes it an interesting material for rf and microwave reconfigurable electronics. To understand the tunability of dielectric constant in a nonlinear fashion, basics of ferroelectric properties are to be reviewed.

2.3 General Properties of Ferroelectric Material

Ferroelectrics are a group of materials that has spontaneous polarization which can be reversed by an electric field. Due to this response of polarization to external field nonlinear dielectric permittivity properties are exhibited as a function of electric field (E) or bias voltage (V) [30].

Ferroelectrics may or may not have iron ions, the term ferro was used in the early stages because of the hysteresis loop which is like ferrites. Ferroelectrics may be in polar (ferroelectric) or non-polar (paraelectric) phase and is characterized by a polarization vs electric field curve. From the fig.2.1, we can see that ferroelectric in the polar phase show hysteresis loop, whereas in the paraelectric phase it doesn't show hysteresis. Due to this hysteresis behavior the ferroelectrics in the polar phase are mainly used in the memory applications, where the two equilibrium states of the spontaneous polarization (+Pr & -Pr) in the hysteresis loop are used to store binary information. In the paraelectric phase the spontaneous polarization is zero and the permittivity is high and is mainly used in the tunable microwave devices, the nonlinear behavior without hysteresis is used for tuning of the dielectric permittivity. As shown in fig.2.1., the dielectric constant increases as the temperature increases in the ferroelectric phase whereas the dielectric constant decreases with increase in temperature in the paraelectric phase obeying the Curie-Weiss Law [30].

$$\epsilon_r = \frac{C}{(T-T_0)} \quad 2-1$$

Where C , is the Curie constant, T_0 is Curie-Weiss phase transition temperature ($T_0 \leq T_c$), T_c is the curie temperature and T is the temperature at which ϵ_r is measured.

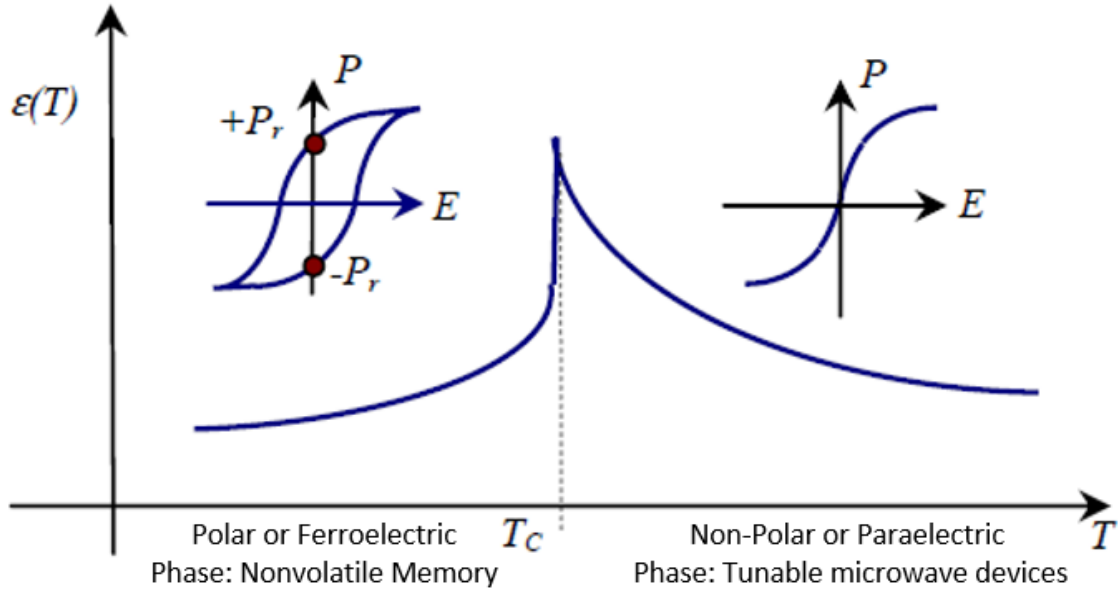


Fig.2.1 Dielectric permittivity vs. temperature of ferroelectric material [30]

In the paraelectric state ($T > T_c$), $\tan \delta$ is lower due to the absence of hysteresis loop which is optimal for microwave applications. Operating just above the T_c can yield large tunability. The high dielectric permittivity in the paraelectric phase mainly depend on temperature, external applied electric field, and mechanical stress. Field dependence permittivity $\epsilon(E)$ and electric field E at a given temperature can be approximated as [30],

$$\epsilon(E) = \frac{\epsilon(0)}{1 + \left(\frac{E}{E_0}\right)^2} \quad 2-2$$

Where $\epsilon(0)$ is the permittivity at zero bias and E_0 is a material parameter.

2.4 Crystal Structure of BST

BST belongs to the perovskite family. Perovskites such as Titanates (BaTiO_3 , CaTiO_3 etc.), Niobates (KNbO_3) and Tantalites (KTaO_3) etc. have a common chemical formula ABO_3 and all have the same crystal structure [30]. It has tetragonal structure in the polar phase and cubic structure in the paraelectric phase as shown in fig.2.2.

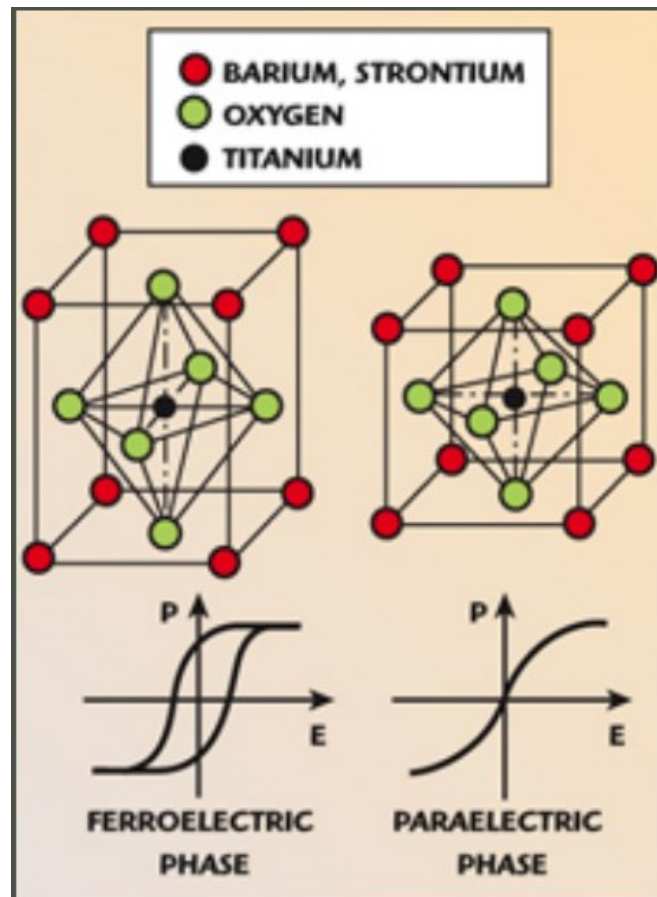


Fig.2.2 Crystal structure in ferroelectric and paraelectric phase of BST [31]

The Ba^{2+} and Sr^{2+} atoms occupy the corner positions which give rise to 0.5 Ba and 0.5 Sr shared atoms per unit cell. The 6 oxygen atoms are face centered which implies there are 3 atoms per unit cell. Ti^{4+} ions located in the center of the cell and is responsible for the spontaneous polarization of BST [32-33].

2.5 Deposition Techniques and Process

Several deposition techniques such as pulsed laser deposition (PLD) [34-36], metal organic chemical vapor deposition (MOCVD) [37], sol-gel [38-39], sputtering [37,39,40,41], chemical solution deposition [42-43] and molecular beam epitaxy (MBE) [44] have been investigated for depositing thin films of BST. Achieving a large area deposition with low cost and high throughput is very significant. Table.2.1 shows summary of attributes and disadvantages of each of the film growth techniques. In this work, PLD technique is used for the deposition of BST thin films. Our group was able to demonstrate deposition of large area BST thin films (up to 4" in diameter) with uniform film thickness, grain size, crystal structure, orientation, and dielectric properties [34]. Due to its ease of operation, excellent stoichiometry transfer of the material from target to substrate as well as the rapid deposition time, PLD is more popular deposition technique for complex oxides such as BST thin films [45]. High quality crystalline films, epitaxial films, multi-layer with high deposition rates can be achieved using PLD. Due to the advancements in the laser technology, high repetition rate and short pulse durations have made PLD a very feasible option to grow complex crystalline oxide films with complex stoichiometry. However, the PLD technique is not standard to the semiconductor industry and is not part of a typical semiconductor foundry fabrication line [45].

Table.2.1 Summary of the attributes and shortfalls of the various complex oxide thin film growth techniques [45]

Complex oxide film growth techniques					
Method attributes	PLD	RF sputtering	MBE	CSD	MOCVD
Industry standard	No	Yes	Yes	Yes	Yes
Large area (>4 in. diameter)	No	Yes	Yes	Yes	Yes
Throughput	Moderate	High	Low	High	High
Deposition rate	High	High (low for off axis)	Low	High	High
Equipment cost	Moderate	Moderate	High	Low	Moderate
Compositional control	Excellent	Moderate	Excellent	Excellent	Excellent
Large area compositional uniformity (4-in. wafer)	Fair ^a	Fairly good	Good	Good	Excellent
Large area thickness uniformity (4-in. wafer)	Fair (<7%)	Moderate	Good	Good	Good
Microstructure	Highly oriented to epitaxial	Highly oriented/textured	Highly oriented, epitaxial, single crystal	Polycrystalline to highly oriented/textured	Highly oriented to epitaxial
Large area uniformity	Fair	Good	Good	Good	Good
Surface morphology (surface smoothness)	Moderate	Moderate smoothness	Excellent (very smooth surfaces)	Excellent (very smooth surfaces)	Good (fairly smooth surfaces)
Film adhesion	Excellent	Excellent	Excellent	Good	Good
Conformal deposition	No	No	No	Yes	Yes
Processing temperatures	High-moderate	High-moderate	High-moderate	Moderate to low	Moderate

^aWith beam profile control.

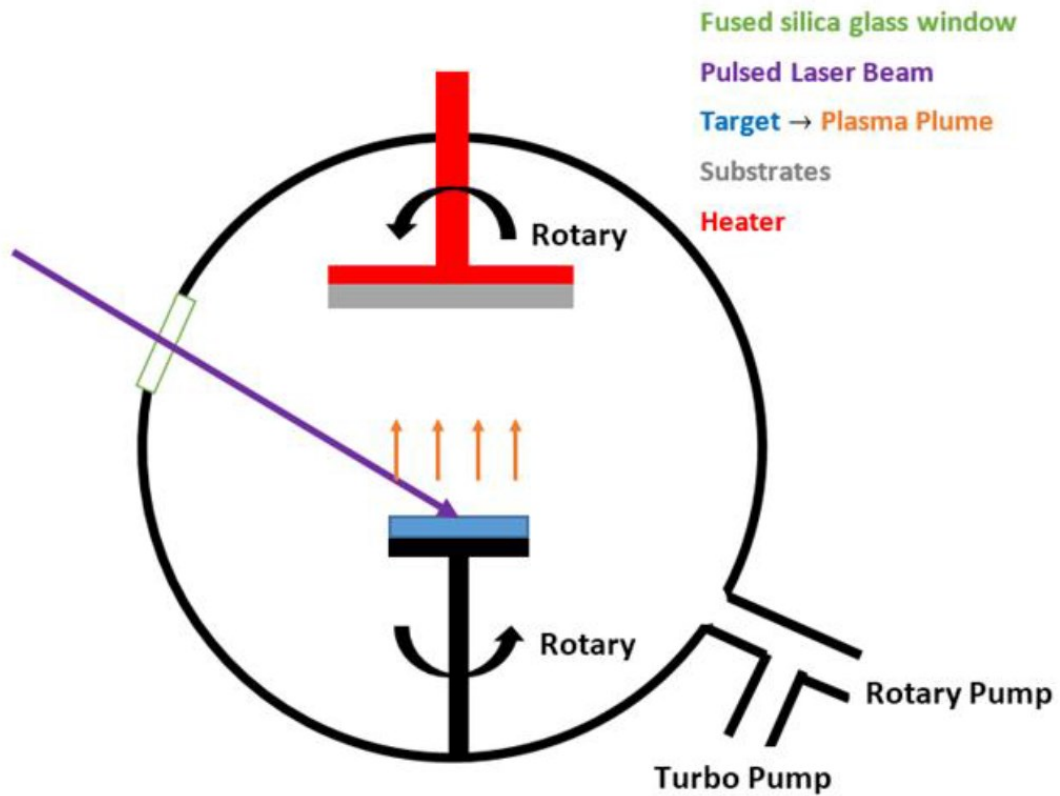


Fig.2.3 Schematic diagram of a typical PLD system [46]

Deposition process for BST thin films used in this work is as follows. Initially the chamber is evacuated using rotary pump and high vacuum turbo pump to avoid any contamination. Oxygen gas is then released and is maintained at 75 mTorr partial pressure during the deposition. A beam of high-power laser pulses, typically 175 mJ – 180 mJ energy with 30 Hz frequency are directed towards a rotated target through lens to increase the intensity of the pulse. As the laser pulse hits the target the material is vaporized from the target (laser pulse plume) which deposits it as a thin film on the substrate placed above the target as shown in fig.2.3. As the laser pulse hits the target, the material ablates and vaporize from the target creating a laser plasma plume. This vaporized material then deposits as a thin film on the substrate placed above the target. The substrate is rotated at a constant

speed to achieve uniform thickness. The substrate is heated to 900 °C before the deposition and kept at this temperature during the deposition. The film properties such as thickness, uniformity, quality is controlled by the laser parameters, pulse repetition rate, optics, chamber temperature as well as oxygen pressure inside the chamber. Fig.2.4 shows large area PLD system from our lab.

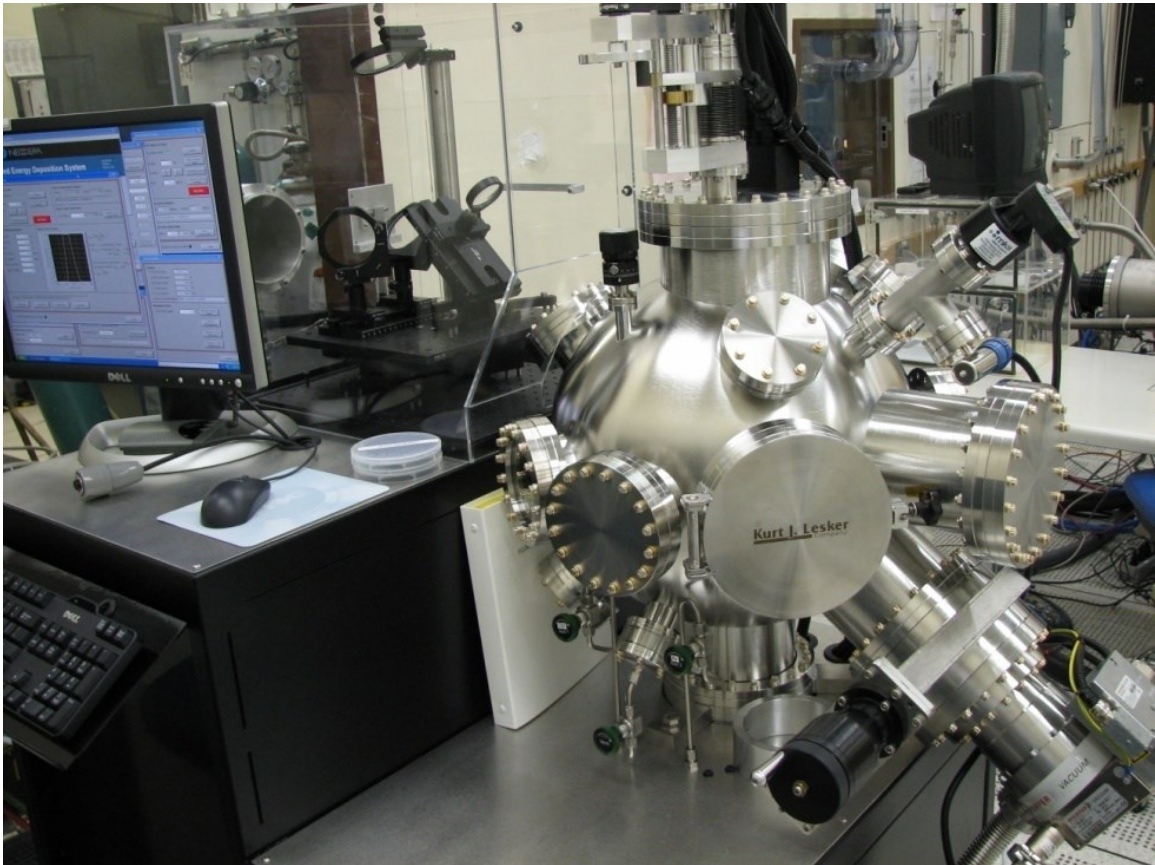


Fig.2.4 Neocera Pioneer 180 large area PLD system in our lab

2.6 Thin vs Thick Films

Ferroelectric thin films have different dielectric properties than thick films (typically thickness greater than 1 μm). Thin films have lower permittivity and tuneability compared to thick films (typically $\epsilon_r > 1000$). But however thick films are temperature dependent. Thin films have stable dielectric constant and relatively temperature insensitive which is an advantage over thick films. Moreover, the tuning ratio η , phase transition temperature T_0 are also lower for thin films compared to thick films. Increasing the strontium concentration, the temperature (T_0) decreases linearly at a rate of 3.4 $^{\circ}\text{C}$ per mole %, which gives an advantage to optimize the thin films over a wide range to meet the specifications of various applications. A comparison of variation of the dielectric constant as a function of temperature of $\text{Ba}_{0.7}\text{Sr}_{0.3}\text{TiO}_3$ films is presented in [47]. As shown in fig 2.5, the dielectric constant for thick films is maximum at phase transition temperature. It undergoes paraelectric to ferroelectric phase transition near room temperature [47]. Whereas in thin film the change is less significant.

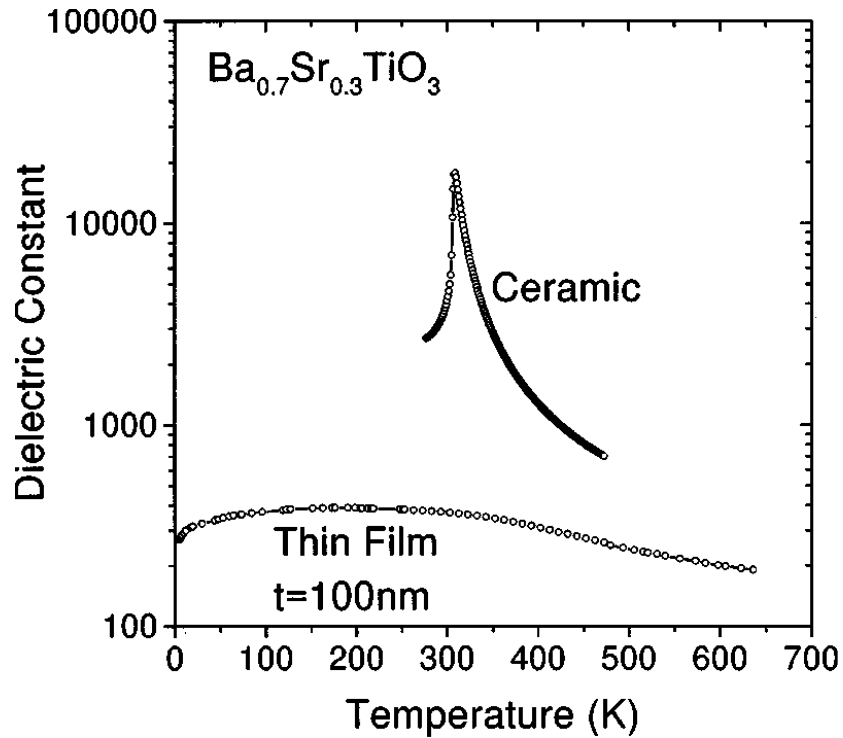


Fig.2.5 Variation of the dielectric constant of thick film vs. thin film as a function of temperature [47]

As mentioned earlier, $\text{Ba}_{0.6}\text{Sr}_{0.4}\text{TiO}_3$ composition has the best tuneability. Moreover, our frequencies of interest in this work are from 24 GHz to 50 GHz, where the lower dielectric constant values of thin films are not significant as at these frequencies, as the values of capacitance required are small.

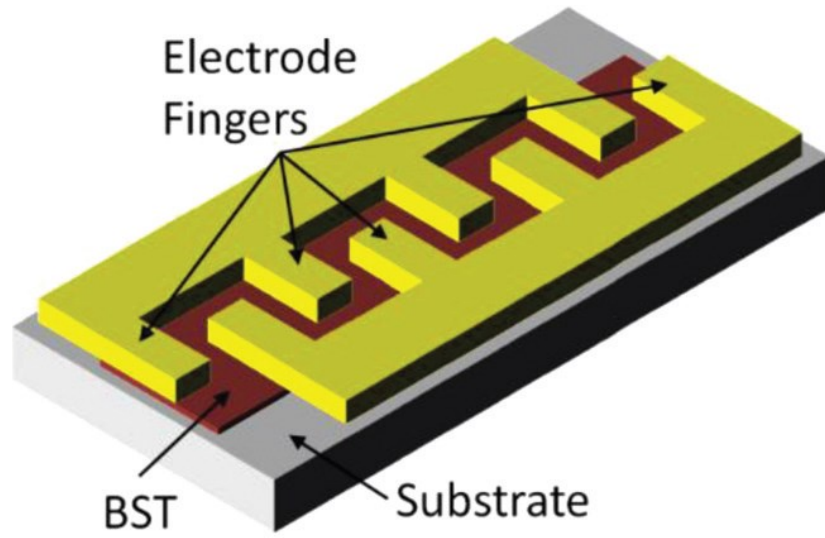
2.7 Applications of BST Thin Films

BST thin films have been used in various applications such as tunable filters [48-50], acoustic wave resonators [51-53], voltage-controlled oscillators (VCO) [54-55] and phase shifters [27,56-57] etc. In [48] a tunable lowpass and bandpass lumped element filters using BST capacitors were presented. The lowpass filter with 2 dB insertion loss and a tunability of 40% (120-170 MHz) with the application

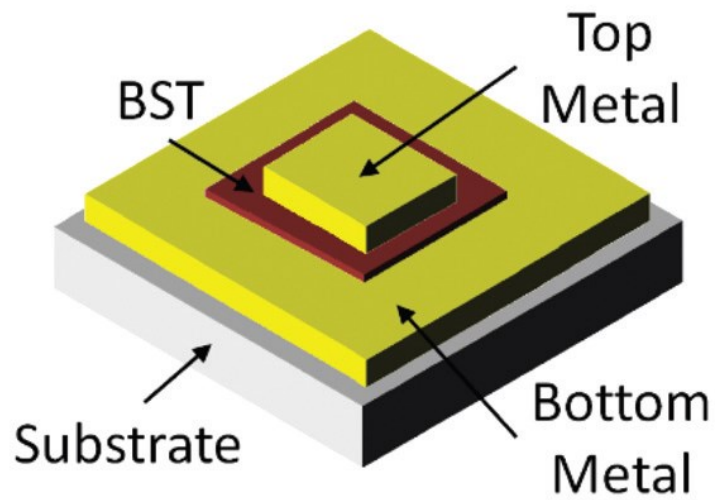
of 0-9 V DC bias as well as the bandpass filter with an insertion loss of 3 dB and a tunability of 57% (176-276 MHz) with the application of 0-6 V DC were demonstrated. Similarly, in [49] a third order combline band pass filter implemented with a parallel plate BST discrete capacitor packaged using conductive epoxy is reported and tuning of central frequency from 1.35 GHz to 1.45 GHz is reported with application of 3 V bias is achieved. A tunable band pass filter to reduce the temperature coefficient of capacitance, graded BST films using MOCVD deposition has been demonstrated on sapphire wafers in [50]. BST is also used in acoustic wave resonators as piezoelectric material. In [51] $Ba_{0.8}Sr_{0.2}TiO_3$ is used as the piezoelectric layer and a Surface Acoustic Wave (SAW) device is implemented. Where as in [52-53] BST is used in Bulk Acoustic Wave (BAW) resonators. In [52] BST is used as free standing piezoelectric films between metal electrodes and in [53] the substrate is acoustically isolated using Bragg reflectors. High Q factor of BST varactors causes lower phase noise, this is a critical factor in VCO circuits. In [54] Victor et.al. used BST varactors to tune Colpitt VCO which operates between 40-50 MHz and in [55] Jamil et.al. used BST varactors in differential VCOs. Which has a tuning range from 205 MHz to 216.3 MHz. BST based varactors are widely used in phase shifter circuits. In [27] previously our group has demonstrated a phase shifter up 15 GHz, 360° phase shift was achieved cascading 15 varactor units with low losses. In [56] Baki et.al., phase shifter circuit using BST thin films are demonstrated, a 265° phase shift with an insertion loss of 5.8 dB at 20 GHz and 180° phase shift with an insertion loss of 4 dB at 30 GHz was achieved. In [57] Mohsen et.al., two designs of compact tunable phase shifters

are presented using screen printed BST thick films. More than 360° phase shift with $51^\circ/\text{dB}$ FOM was achieved.

BST based varactors such as coplanar interdigitated capacitor (IDC's) and parallel plate capacitors are the most used in rf/um reconfigurable electronics. The interdigitated capacitors are easier to fabricate as it only requires one patterned metal layer on the top of BST thin film compared to parallel plate capacitors which requires two metal layers. The parallel plate capacitor type varactor has higher electric field compared to interdigitated type for the same DC bias applied between the electrodes. Thus, large tunability is achieved using parallel plate varactors ($>60\%$) compared to the interdigitated capacitors [45]. For IDCs the tuning is achieved by the electric field between the fingers which tunes the BST thin film. Fig.2.6 show IDC and varactor device.

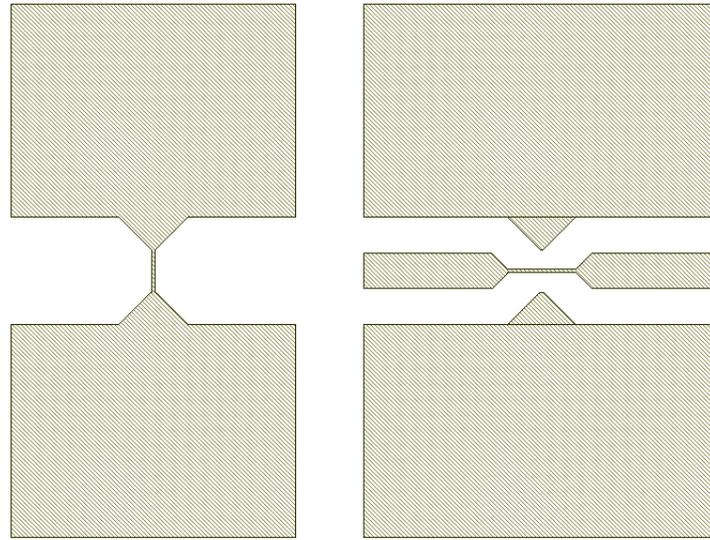


(a)



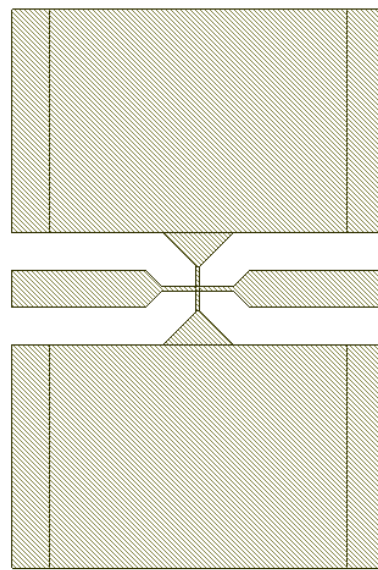
(b)

Fig.2.6 (a) Interdigitated capacitor (b) Parallel plate capacitor [45]



(a)

(b)



(c)

Fig.2.7 (a) Bottom metal (b) Top metal (c) 5 μm x 5 μm varactor

The standard varactor shunt device used in our lab is shown in fig.2.7. BST layer is sandwiched between top and bottom metal. The center area is the varactor area, where the overlap is formed. The magnitude and phase response of the 5 μm x 5 μm varactor are shown in fig.2.8.

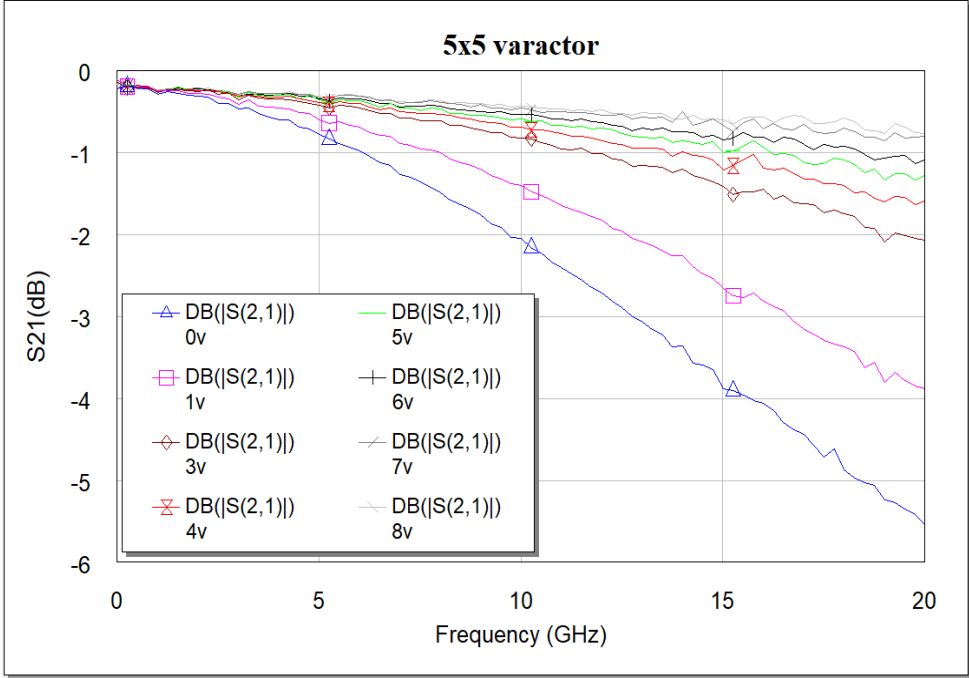


Fig.2.8 Measured S₂₁ magnitude of a 5 μm x 5 μm varactor

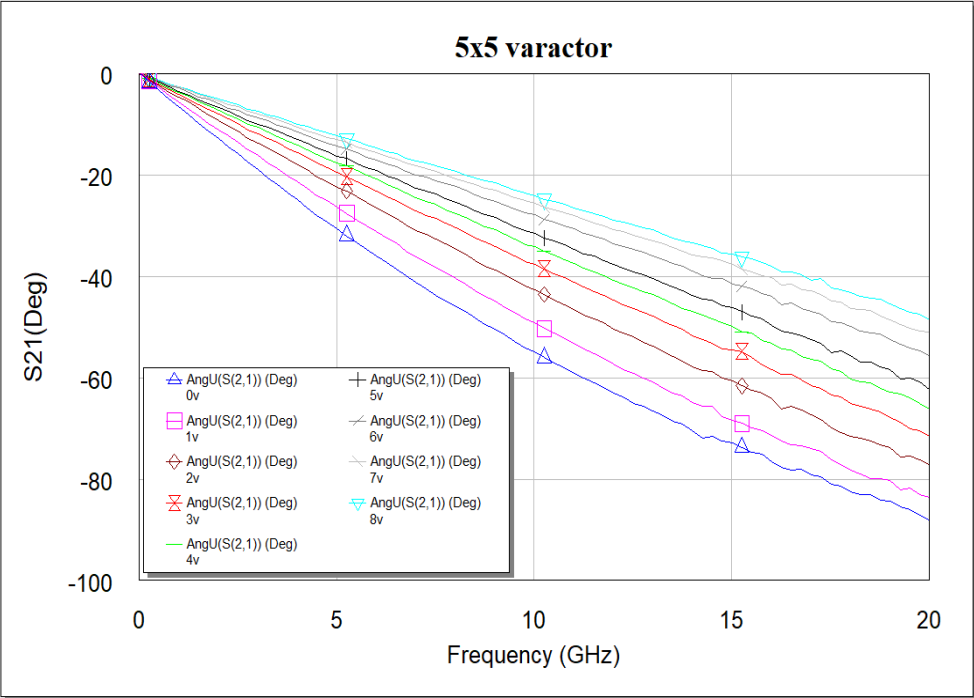


Fig.2.9 Measured S₂₁ phase of a 5 μm x 5 μm varactor

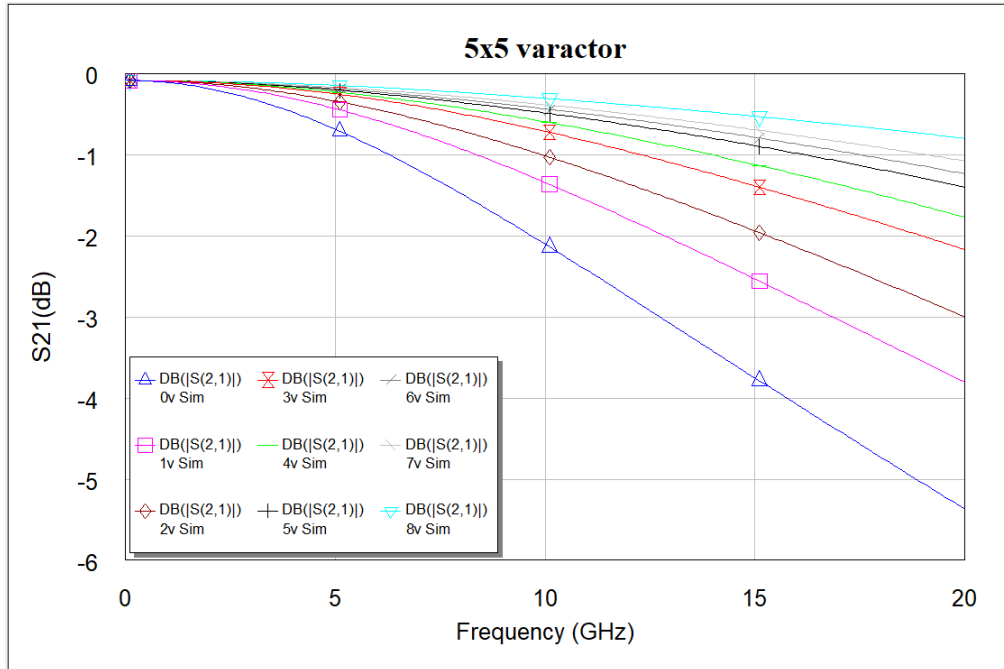


Fig.2.10 Simulated S₂₁ magnitude of a 5 μm x 5 μm varactor

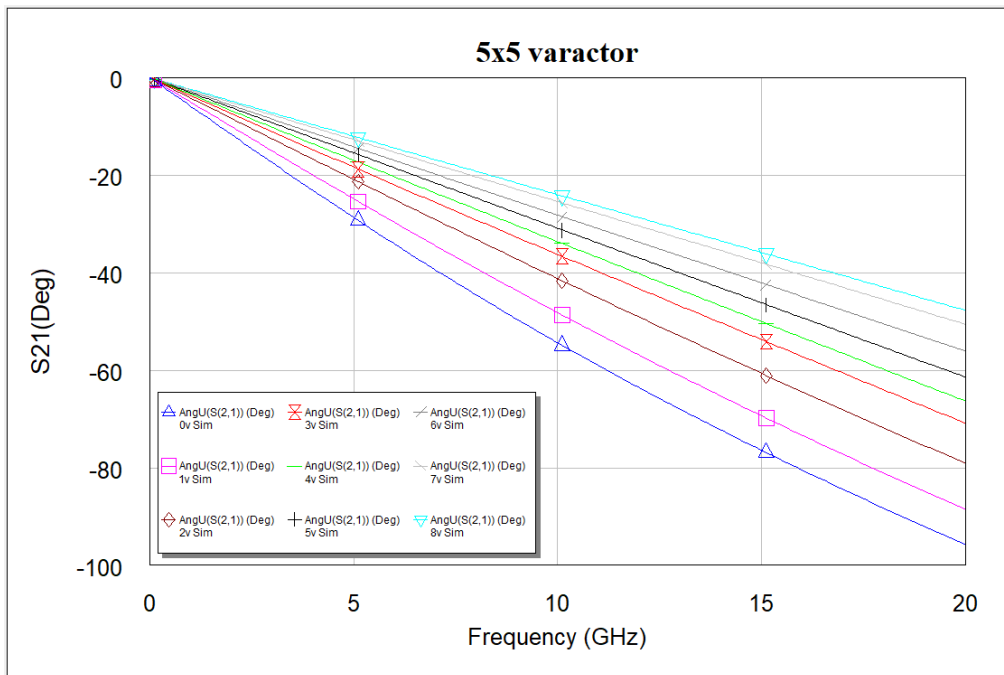


Fig.2.11 Simulated S₂₁ phase of a 5 μm x 5 μm varactor

2.8 Equivalent Circuit Model

The varactor device can be represented electrically using the equivalent circuit model as shown in fig.2.12. The model was first demonstrated in [58]

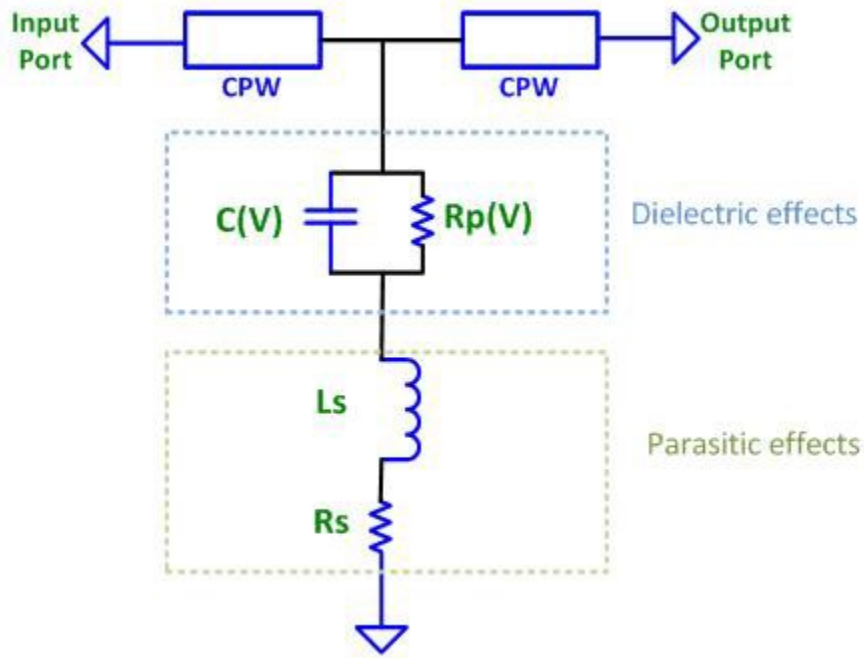


Fig.2.12 Equivalent circuit model for the shunt varactor device

Where $C(V)$ – represents the voltage dependent capacitance of the varactor

$R_p(V)$ - is the shunt resistance of the varactor, modeling the leakage of BST thin film

L_s – Parasitic series inductance associated with the varactor

R_s – Parasitic series resistance of the varactor due to metal electrodes.

Each of these values can be calculated based on the geometry of the parallel plate varactor as follows:

$$C(V) = \frac{\epsilon_0 \cdot \epsilon_r \cdot A}{d} \quad 2-3$$

Where ϵ_r is the relative dielectric permittivity of BST thin film

ϵ_0 is the dielectric permittivity of free space

A is the overlap area of the top and bottom electrodes

d is the thickness of the BST

$$R(V) = \frac{1}{\omega \cdot C \cdot \tan \delta} \quad 2-4$$

Where ω is the angular frequency in radians

C is the varactor capacitance

$\tan \delta$ is the dielectric loss-tangent of the BST layer

$$R_s = \frac{l}{\sigma \cdot w \cdot t} \quad 2-5$$

Where l is the length of bottom electrode metal layer

σ is the conductivity of the bottom metal layer

w is the width of the electrode layer

t is the thickness of the bottom metal layer

Table.2.2 Extracted parameters for a 5 μm x 5 μm varactor

Voltage	C (pF)	Rp (Ohms)	Ls (nH)	Rs(Ohms)
0v	0.5	3000	0.01	0.5
1v	0.41	3000	0.01	0.5
2v	0.33	3000	0.01	0.5
3v	0.28	3000	0.01	0.5
4v	0.24	3000	0.01	0.5
5v	0.2	1000	0.01	0.5
6v	0.16	1000	0.03	0.5
7v	0.13	1000	0.05	0.5
8v	0.11	1000	0.04	0.5

The device shows dielectric tuning from 825 to 200 which gives about 4:1 tuning. The parasitic inductance is typically negligible. The value of inductance is predominant at higher frequencies. Keeping the device small, smaller inductance values can be achieved. The varactor presented in this section has smaller inductance value, but it is not negligible at higher DC bias voltages. Further optimization is required to design a varactor at higher frequencies especially at mmWave frequencies. The longer signal trace introduces inductance which will cause more insertion loss, especially for the application is of phase shifters at higher frequencies. Varactor area also needs to be reduced to mitigate the dielectric leakage which could make the device lossy. Fig.2.13 shows relative dielectric constant vs applied bias for a 0.25 μm thick BST thin film on a sapphire wafer.

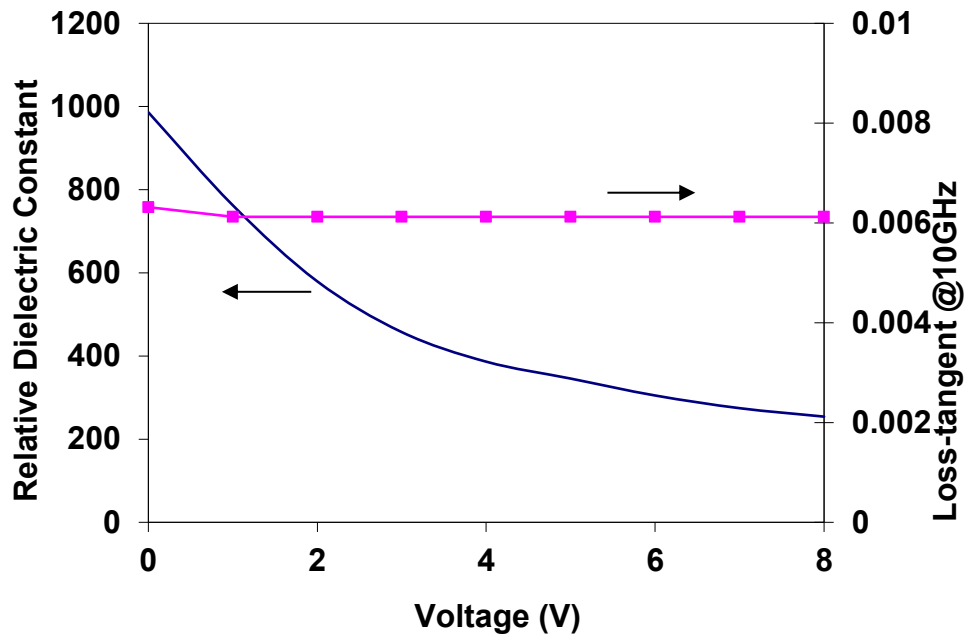


Fig.2.13 Dielectric properties of 0.25 μm BST thin film on sapphire substrate

CHAPTER 3

OVERVIEW OF GERMANIUM TELLURIDE (GeTe) AND ITS APPLICATIONS

3.1 Introduction

Germanium Telluride (GeTe) is a chalcogenide phase change material which can be transformed in between crystalline or amorphous states [59] and is famous for their unique optical characteristics. It has wide applications in memory-based industries for improved switching speed over flash memory. Phase change memory materials based on chalcogenide alloys are widely utilized commercially as active layers for optical storage media such as rewritable compact discs and digital video discs [60-61], and their usage in non-volatile electronic memory is expanding in importance [62]. The change in reflectivity is used to store the information as dark or shiny spots. Non-volatile memories using change in resistance have also been introduced [63-66]. The significant changes in optical and electrical properties that occur during the reversible crystallization of amorphous thin films give them their distinct characteristics.

Ovshinsky [67] identified the unusual phase transition processes between disordered amorphous and ordered crystalline states in Te based alloys in 1968, and since then, significant research of these alloys have taken place [68]. In today's world the most used memories are nonvolatile memories. These are based on the principle of charge storage. The major problem memory industries are facing is the miniaturization problem [69]. The magnetic and ferroelectric random-access memories have scalability problems. Data in PCM's are stored in a glass

containing chalcogens like S, Se or Te or pnictogens like Sb [69]. To switch the material between crystalline and amorphous states different approaches can be used and one such way is to use a low voltage like ultra-fast laser pulses. The crystalline state where the atoms are arranged is considered as 'on' state and the amorphous state where the atoms are disordered is considered as 'off' state.

Ge-Sb-Te family is the most interesting in general and $\text{Ge}_2\text{Sb}_2\text{Te}_5$ (GST) has been considered as the reference for PCM applications [70]. Low crystallization temperature (about 140 °C) is one of the major drawbacks for GST [71]. Operating at moderate temperatures can cause reduced data retention time. For automotive applications GST is inapplicable as the operating temperature would be around 150 °C [72]. To overcome this problem more study has been done on different materials, the binary compound GeTe has attracted the attention for such applications [73]. It has significant improvement in the crystallization speed and data retention temperature and moreover it has very good contrast in terms of electrical resistivity between two states [73-76]. The crystal structure of GeTe is a rhombohedrally distorted NaCl type structure with Ge and Te atoms each occupying a face centered cubic sublattice, whereas the amorphous structure of GeTe is usually assumed to possess a randomized rhombohedral structure, which is close to the crystalline state locally but without any long-range order [70,77].

3.2 Deposition

Deposition of GeTe can be done using both sputtering and PLD, in [69–70,78] PLD is used for growing GeTe films, [79-82] have used sputtering and chemical vapor deposition (CVD) method is used in [83-86] to grow the thin films. Chalcogenide films in general are known to exhibit deposition dependent electrical properties as well as heating rate dependent amorphous to crystalline transition temperatures. Using PLD as the method of growing GeTe thin films have some advantages over sputtering and CVD. The electrical properties of the target are not crucial when compared to DC sputtering. PLD enables precise control over the growth rate and moreover PLD allows the deposition of films with unusual composition and with stoichiometric transfer of a target material to the film [70]. In [78] Hao et. al. has used PLD to grow GeTe₄ films on Si (111) substrates. In [73] Sun et.al. have studied the structural and optical properties of the films and their phases transformations induced by pulse irradiation of the GeTe thin films. They have used Si (100) substrate and the deposition was carried out at room temperature. PLD deposition technique is used in this work. The deposition parameters we have used are given in table.3.1.

Table.3.1 Deposition parameters using PLD

Substrate	SiO₂/Si
Temperature	Room temperature
Laser Fluence	3.6 J/cm ²
Pulse Repetition Frequency	10 Hz
Pressure	5 x 10 ⁻⁶ Pa (vaccum)
Rate of deposition	~ 128 nm/min

3.3 Phase Transitions

Transition between amorphous and crystalline state is accomplished different ways. The general theme is to heat and cool the PCM. When the PCM is in crystalline state, the transition to amorphous state is achieved by heating it beyond its melting temperature (T_{melt}) as a liquid, the atoms are randomly distributed relative to their neighbors and quenching it to solidify the atoms in the amorphous state. When the PCM is in amorphous state, it is in a high electrical resistance state. The transition to the crystalline state is achieved by heating the material above its crystalline temperature (T_{cryst}), which is the temperature at which nucleation and growth of crystalline grains is enabled [87]. Fig.3.1 shows the heat profiles used for transition of each state.

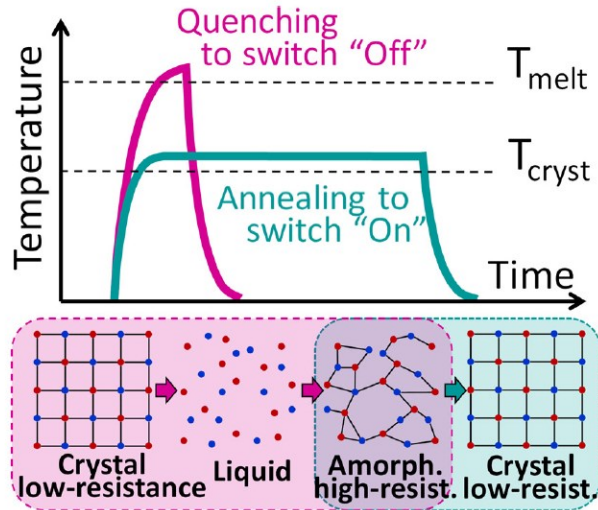


Fig.3.1 Heat profiles used for transition to each state [59]

In [73], the amorphous to crystalline and vice versa phase transition of GeTe films grown by PLD were achieved by irradiation with 20 ns laser pulses at a wavelength of 248 nm. A reversible phase transition is realized by using pulse numbers greater than or equal to five at fluences above the threshold fluence between 11 and 14 mJ/cm² for crystallization process and a single pulse at a fluence between 162 and 182 mJ/cm² for amorphization.

Where as in [87] the transition from crystalline to amorphous and vice versa are achieved using Joule heating (I^2R), the electric current raises the temperature of the PCM. Lower intensity current pulses are used to crystallize the material and higher intensity pulses are used to amorphize the material with switching speeds on the order of nanoseconds. A detail analysis regarding the joule heating is done in [88].

3.4 Crystallization

For crystallizing the deposited film, the samples were annealed in the vacuum chamber for 20 minutes at different temperatures. The XRD of the as-deposited films and thin films annealed for 20 min. in vacuum is shown in fig 3.2.

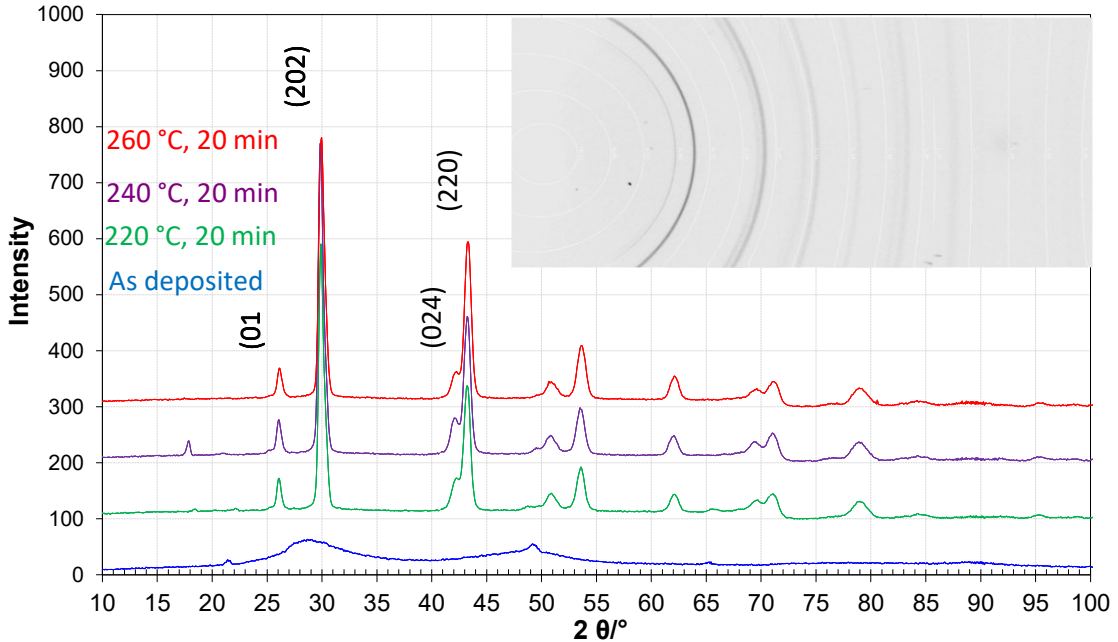


Fig.3.2 XRD patterns at different temperatures

From fig.3.2, we can see that the XRD patterns for the films annealed at different temperatures. The as-deposited film shows that it is in amorphous state. We can see that the film annealed at 220 °C for 20 min. started crystallizing. This can be noticed from the higher intensity spike at 29.9 degrees in 2θ and for the sample which is annealed at 240 °C for 20 min, which tells us that 220 °C was not sufficient for annealing. Different diffraction peaks at angles 26.1°, 29.9°, 42.4°, 43.3°, 51.4° and 53.9° emerge, which are correlated to lattice planes (012), (202), (024), (220), (006) and (042) of rhombohedral GeTe respectively [70]. However,

with further increase of the annealing temperature up to 260 °C the intensity of the spike at 29.9° gradually decreases. This might be because of the partial evaporation of the films in the vacuum. Fig.3.3 shows the SEM images of samples annealed at different temperature. All three samples show smooth crystallinity, however sample annealed at 240°C is the optimum crystallization temperature.

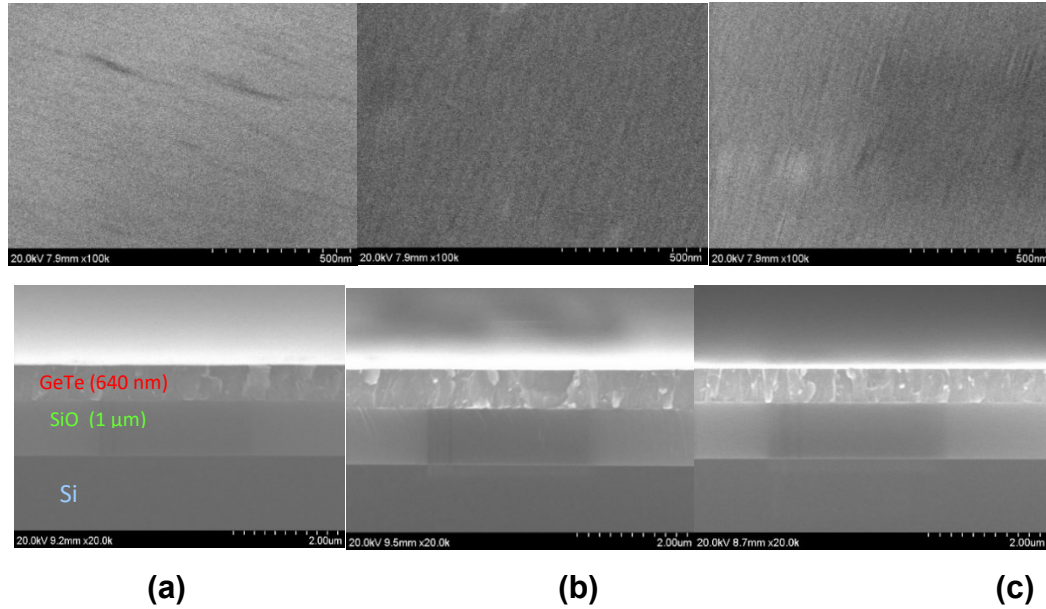


Fig.3.3 SEM images of samples annealed at different temperatures (a) 220 °C (b) 240 °C and (c) 260 °C

Similar properties were observed by Sun et.al. in [70] but at different annealing temperatures. From fig.3.4, we can see that the films annealed at 200 °C and 220 °C show a very broad peak in 2θ range between 25 and 30 degrees, typically suggesting amorphous state of the film. At 240 °C the film started crystallizing and the maximum intensity was seen at 280 °C. Further increase in the temperature the intensity gradually decreases. There is no peak seen for the film annealed at 380 °C this is due to the complete evaporation of the film.

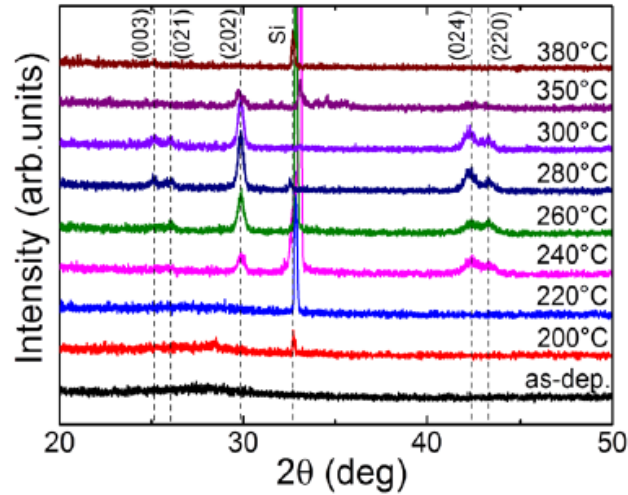


Fig.3.4 XRD patterns of the as deposited GeTe film and the films annealed at different temperatures [70]

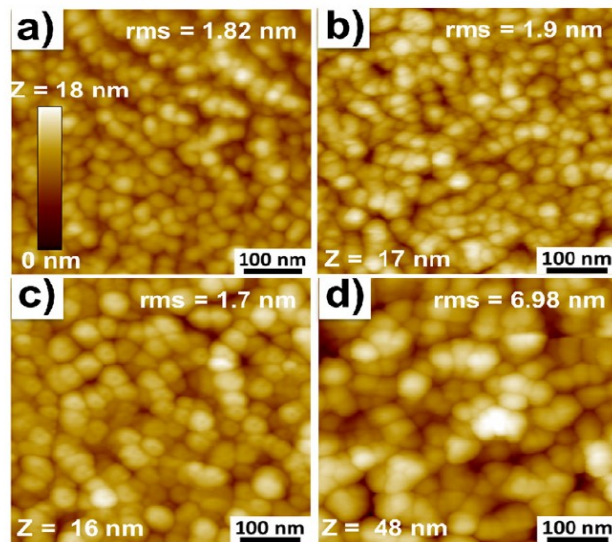


Fig.3.5 Atomic force microscopy (AFM) images of GeTe films annealed at a) 240 °C b) 260 °C c) 280 °C d) 350 °C [70]

In [70] Sun et.al. also have studied grain size variation with temperature and it is also mentioned that not much difference in morphology is observed between room temperature and 220 °C. However, from 240 °C annealing, crystallites clearly emerge. Further increase leads to a uniformly enhanced coarsening of crystallites. The grain sizes at different annealing temperatures are shown in fig.3.5.

In [78] Jiang. et. al. has studied the characterization of GeTe₄ thin films as a candidate for phase change memory applications. The XRD for GeTe₄ is shown in fig.3.6.

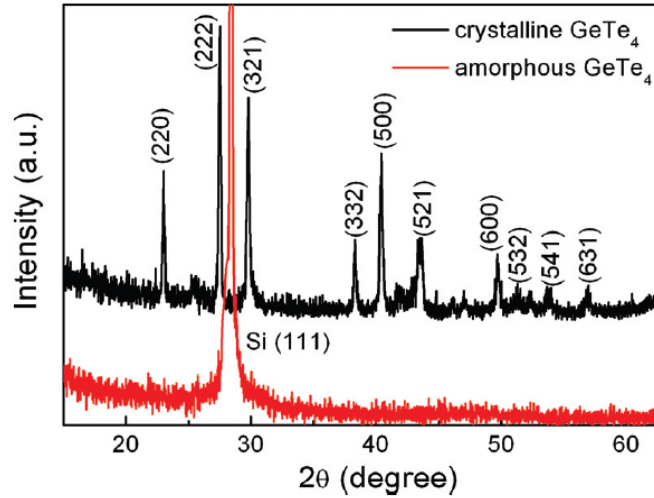


Fig.3.6 XRD pattern of GeTe₄ film [78]

In [78] it was mentioned that the GeTe film was annealed at 553 °K in nitrogen flow to achieve crystalline films. The as-deposited film is amorphous and after annealing we can see the crystalline films. The main diffraction peaks of (222), (321), (220), (500), (332) and (521) for GeTe₄ can be indexed.

In [80] a study on the structural and electrical properties of the GeTe film under different annealing conditions is carried out. In [80] the films were deposited on Si wafer at room temperature and at 200 °C using RF sputtering. The base pressure was 4 mPa and the working pressure was adjusted to 400 mPa by introducing the argon gas. The deposition rate was 0.2 nm/s. Depending on the deposition conditions, the amorphous GeTe was converted to cubic crystalline (C-GeTe) (sample deposited at room temperature) and rhombohedral structure (R-GeTe) (sample deposited at 200 °C). All the films were annealed at 400 °C in either

air or N₂ for 10 min, 100 min, and 1000 min. For the C-GeTe after subsequent annealing in air, phase transitions were induced. This resulted in the formation of Ge oxide as the major phase and metallic Te as the minor phase. For the R-GeTe regardless of the annealing time and atmosphere the rhombohedral structure was maintained. Oxygen can easily penetrate the chalcogenide alloys during the switching cycles.

For C-GeTe, high sheet resistance of several tens of megaohms per square was measured. After thermal annealing for 10 min, the sheet resistance decreased rapidly to 41 Ω/m^2 and 71 Ω/m^2 in N₂ and air atmospheres respectively. The correlation between the sheet resistance and the annealing temperature was unclear. The sheet resistance for the samples C-GeTe samples in air for 100 min increased to $3.8 \times 10^6 \Omega/\text{m}^2$. The sheet resistance after 1000 min was likely to be higher than several tens of megaohms per square. But in the N₂ atmosphere the sheet resistance showed a slight increase. Whereas for R-GeTe the sheet resistance initially was 32 Ω/m^2 . After 10 min annealing in air the resistance was reduced to 16 Ω/m^2 and no variations were seen for further annealing. But in the case of N₂ atmosphere the sheet resistance did not change up to 100 min. After 1000 min of annealing the sheet resistance increased slightly to 44 Ω/m^2 .

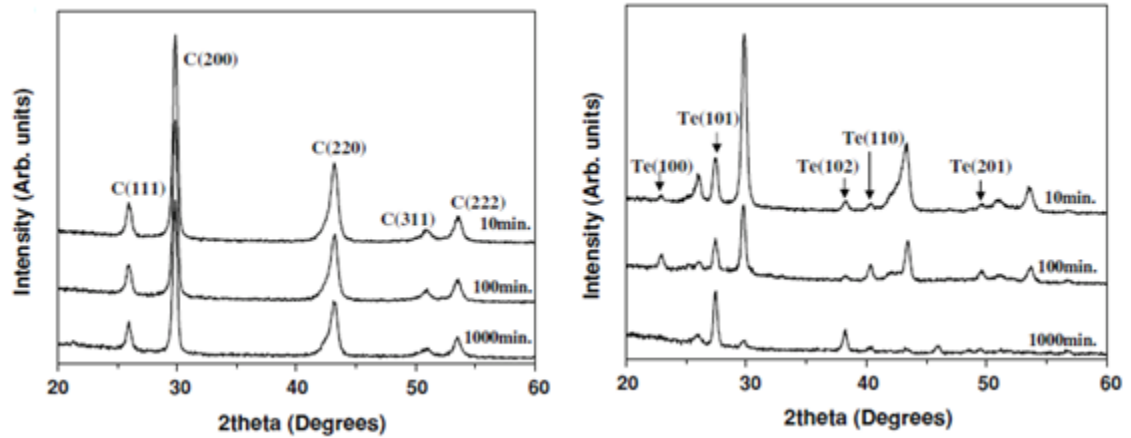


Fig.3.7 XRD spectra for a) C-GeTe annealed in N₂ b) C-GeTe annealed in air [80]

From the fig.3.7 a), we can see that the C-GeTe after annealing in N₂ for 10 mins the sample crystallized into cubic structure and no change in further annealing. From fig.3.7 b) after a 10 min annealing treatment in air, a metallic Te phase appeared along with a cubic GeTe phase. The metallic phase remained after further annealing, but the cubic GeTe phase completely disappeared after 1000 min.

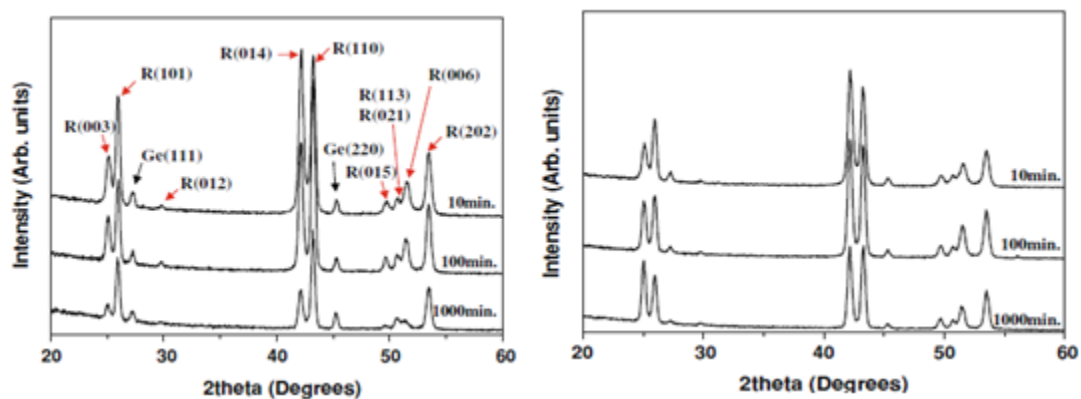


Fig.3.8 XRD spectra for a) R-GeTe annealed in N₂ b) R-GeTe annealed in air [80]

In the case of R-GeTe the as-deposited phases were metallic Ge and rhombohedral GeTe. These phases showed no variation regardless of the annealing time and atmosphere as seen in fig.3.8 a) and b).

The samples that were annealed for 1000 mins in air for both C-GeTe and R-GeTe, the thickness of the GeTe film was about 120 nm and 270 nm for the C-GeTe and R-GeTe compared to initial thickness of 160 nm and 270 nm for C-GeTe and R-GeTe respectively. The difference in 40 nm thickness in the C-GeTe may be related to the disappearance of the cubic GeTe phase from the XRD pattern. The cubic GeTe phase may have decomposed and been converted to Ge or Te oxide due to reaction with oxygen.

The temperature vs resistivity plot shown in fig.3.9 shows the material has five orders of off/on ratio, when comparing the as-deposited amorphous state and the crystalline state. The major advantage of GeTe is that its crystalline resistivity is amongst the lowest known for a phase change material. Thus, its application as an RF switch [88] is very attractive. Fig.3.10 shows the DC test structure used to measure the resistance of the GeTe thin films.

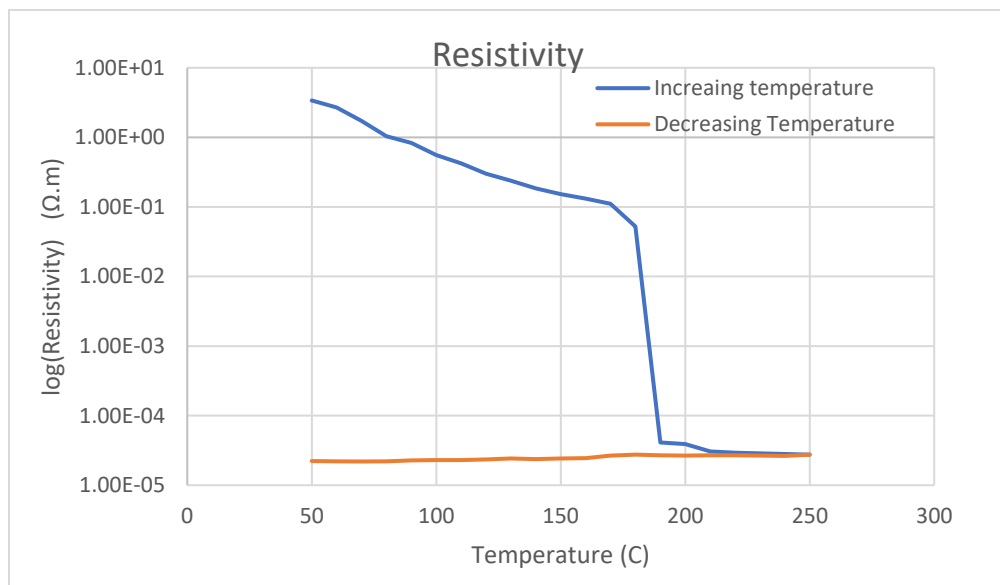


Fig.3.9 Temperature vs. resistivity plot

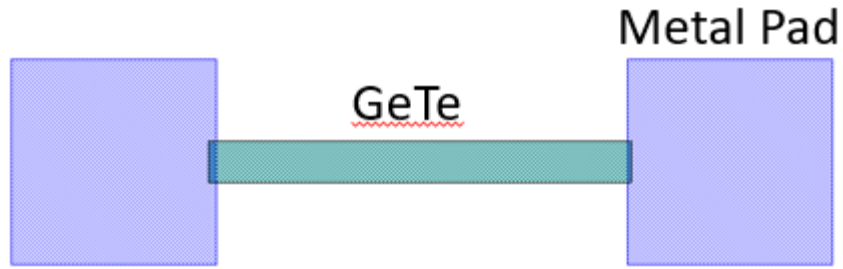


Fig.3.10 DC test structure

The equations below show how the resistivity and the conductivity were calculated after the resistance being measured

$$\text{Resistivity } \rho = A * \frac{R}{l} \text{ (}\Omega \cdot \text{m)} \quad 3-1$$

$$A = W \times \text{thickness} \quad 3-2$$

$$\sigma = \frac{1}{\rho} \text{(S/m)} \quad 3-3$$

Where W is the width of the GeTe stub

R is the measured electrical resistance

L is the length of the GeTe stub

A is the cross-sectional area of GeTe

3.5 Amorphization

Crystallized GeTe thin films are to be re-amorphized, this can be done through melt-quench process. To achieve this the film must be heated beyond the melting temperature (725 °C). As mentioned before there are three ways to heat the material beyond its melting temperature.

- (a) Thermal heating: This is not a good method as it causes film degradation and evaporation.
- (b) Laser heating: Illuminating the thin film with high intensity nano second laser pulses.
- (c) Joule heating (I^2R): A short dc pulse is applied to the in-circuit heater.

Thermal heating degrades the sample it is slow process and it causes loss of the sample due to evaporation. Joule heating is not feasible for plane samples. So, Laser heating was tried on the crystallized samples. This was done by illuminating 20 ns laser pulses from KrF 248 nm PLD laser of 156 J/cm^2 . However, using the 248 nm laser the sample was completely lost instead of amorphizing the film as the number of pulses were increased. The laser, ablated the material on the test sample.

Instead of pulsed laser, CO_2 CW ($10.6 \text{ }\mu\text{m}$ wavelength) laser was used on the as deposited GeTe samples on sapphire wafer. Fig.3.10 shows GeTe sample exposed to different CO_2 laser power, where CO_2 laser is used to draw line patterns as shown in the fig.3.10. 5% to 100% laser power of a total 10 W power has been used, no change in resistance and surface morphology was observed for the samples hit with 5%-15% laser power, this can be seen in fig.3.10(a), however from 20% to 100% laser power, the laser damages the surface. This could be mainly because of the sapphire wafer, which has 0% transmission at the $10.6 \text{ }\mu\text{m}$ wavelengths of CO_2 laser. The sapphire wafer absorbs all the power (radiation from the laser) through the GeTe thin film this causes zero absorption in the GeTe thin film and the ablation of the GeTe film is caused from the sapphire wafer side.

Fig.3.11 shows the infrared transmission properties of sapphire. The amorphization of GeTe films is left for future work.

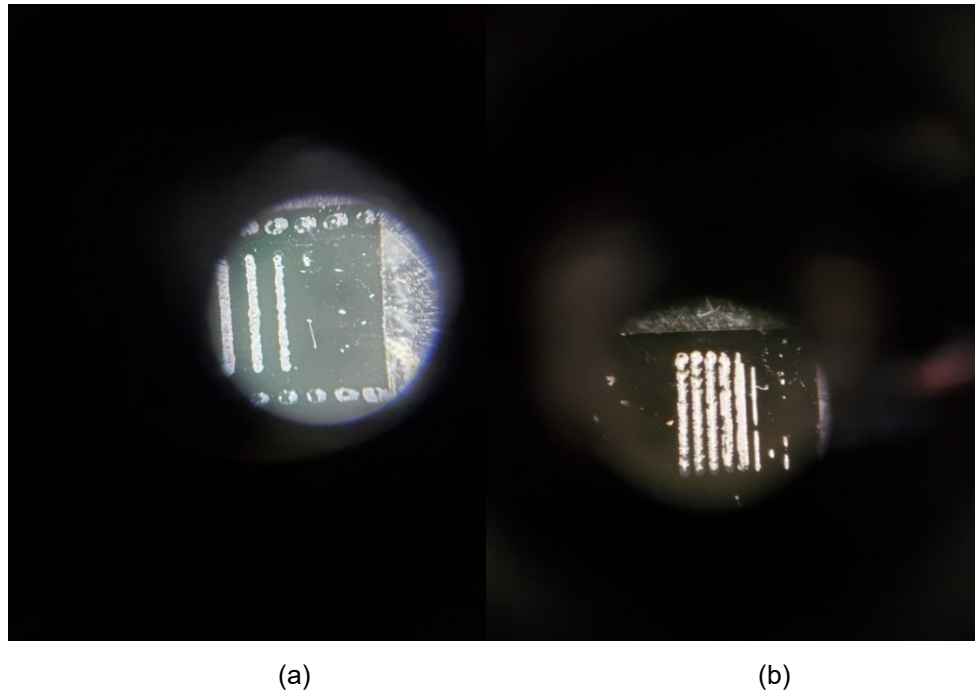


Fig.3.11 GeTe 250 nm as deposited samples exposed to CO₂ laser at different laser energies

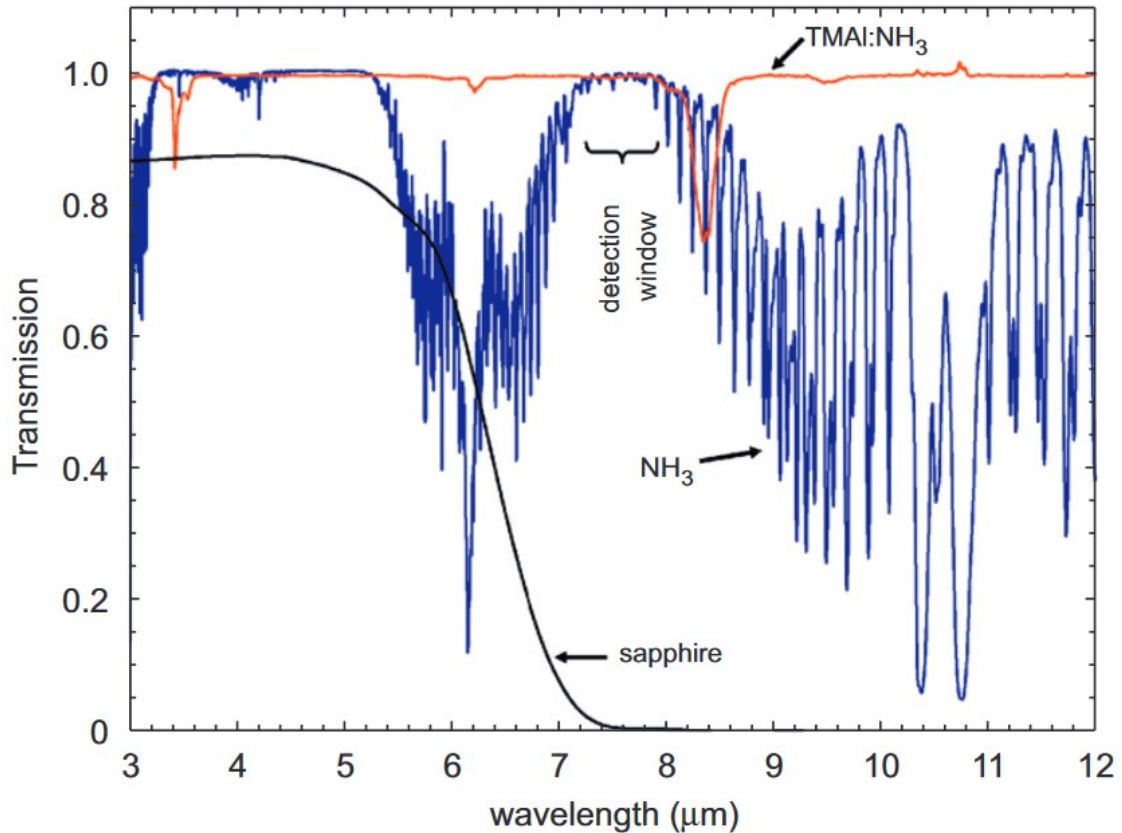


Fig.3.12 Infrared transmission properties of (a) Sapphires, (b) Ammonia, and (c) TMAI:NH₃ adduct, near room temperature [89]

3.6 RF Switch

As RF mobile technology evolves from 4G to 5G technologies, wireless communication systems require complicated radio frequency (RF) front end modules to enable reconfigurable and multiband operations. Low insertion loss, good linearity, excellent isolation, and high reliability are all requirements for these complicated RF modules [90]. Solid state RF switching devices are widely employed in today's cellular telecommunication systems, owing to their great dependability and ultra-fast switching speed. However, these devices with high nonlinearity, high power consumption, and low power handling capabilities open

the way for radio frequency microelectromechanical systems (RF MEMS) switches to be used commercially [91]. CMOS switches suffer from power handling capacity and modeling issues [14]. Recently, several groups have demonstrated PCM based rf switches. Our group has demonstrated Vanadium Dioxide VO_2 based rf switches in the past [16,19]. These switches are easy to fabricate and uses CPW configuration which makes them CMOS compatible. VO_2 -based devices, on the other hand, have a lower power handling capability than RF MEMS devices. Furthermore, VO_2 devices have a high-power consumption because continuous direct current (DC) power is required during the ON state, whereas PCM-based devices have a latching ON state that does not require constant DC power. Apart from optical storage, the PCM's huge resistivity difference between amorphous and crystalline states, as well as its ability to switch reversibly and frequently, make it a promising option for rf switching. GeTe has high thermal stability and its on state resistance is very low making it suitable for switching applications [92].

RF Switches using PCM have been demonstrated in [59,79,87,93-100]. In [79] SPST switch with micro heaters is demonstrated and the parasitic capacitance from this micro heater limits the performance. A modification digital version of switch is presented [100] with improved performance is presented however the design complexity has increased. In this chapter a GeTe based switch is demonstrated with very low insertion loss of 0.23 dB and high isolation of 19.7 dB measured at 15 GHz. A study on the length of GeTe slot is conducted. The devices are very easy to fabricate.

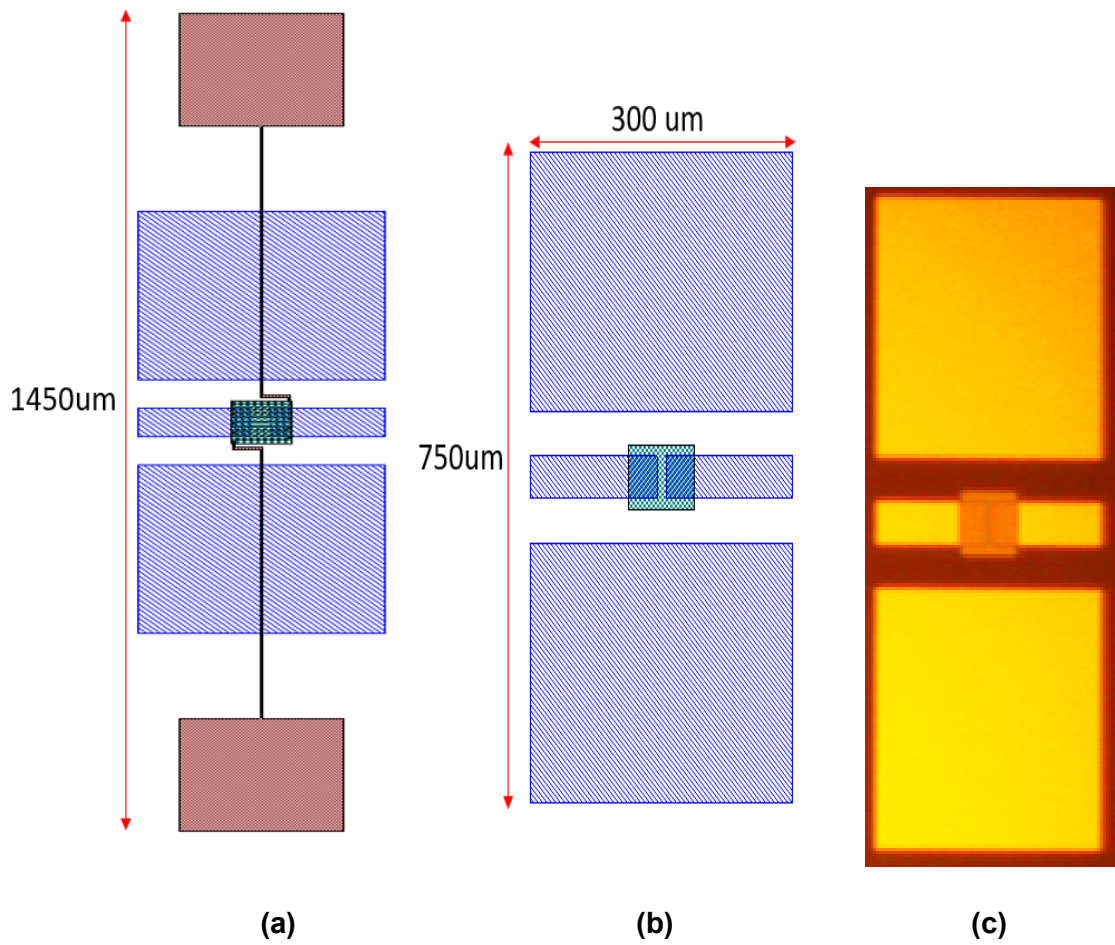
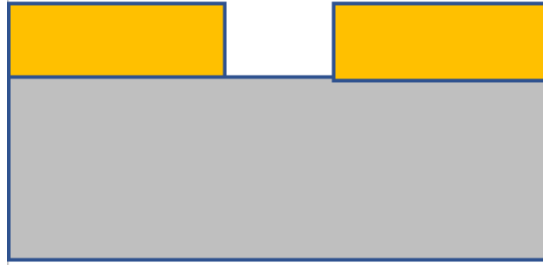


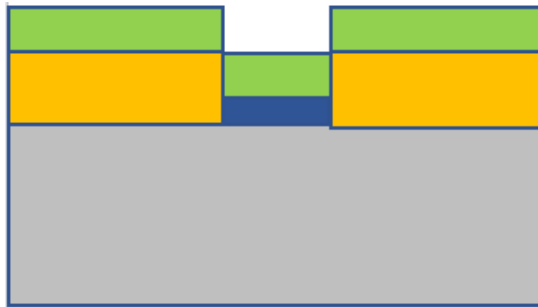
Fig.3.13 RF switch (a) with heater coil (b) without heater coil (c) 5μm gap switch without heater coil on wafer



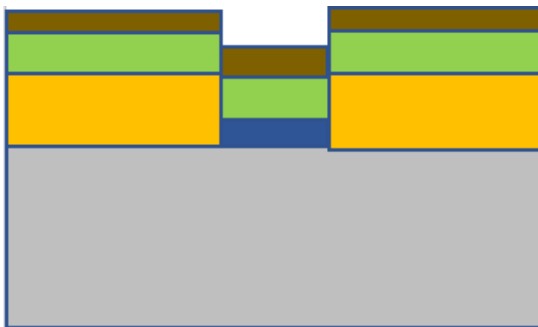
(a) Top metal deposition and liftoff



(b) GeTe deposited and etched



(c) Passivation deposited and etched



(d) Heater coil (patterned)

Fig.3.14 Fabrication procedure for rf switch

3.7 Measurement Setup

A Keysight N5235B PNA-L (Programmable Network Analyzer) network analyzer with a frequency sweep from 10 MHz to 50 GHz is used to test the devices in our lab. The calibration of the PNA/VNA is required prior to the measurement. The PNA's/VNA's calibration takes into consideration factors including cable length, probe loss, measurement arrangement, and temperature.

Short, open, load, and through (SOLT) approaches can be used to perform the calibration operations. 150 μm pitch ground-signal-ground (GSG) microwave probes and cables connect the Device Under Test (DUT) to the PNA. The measured swept frequency S-parameters can be saved and documented.

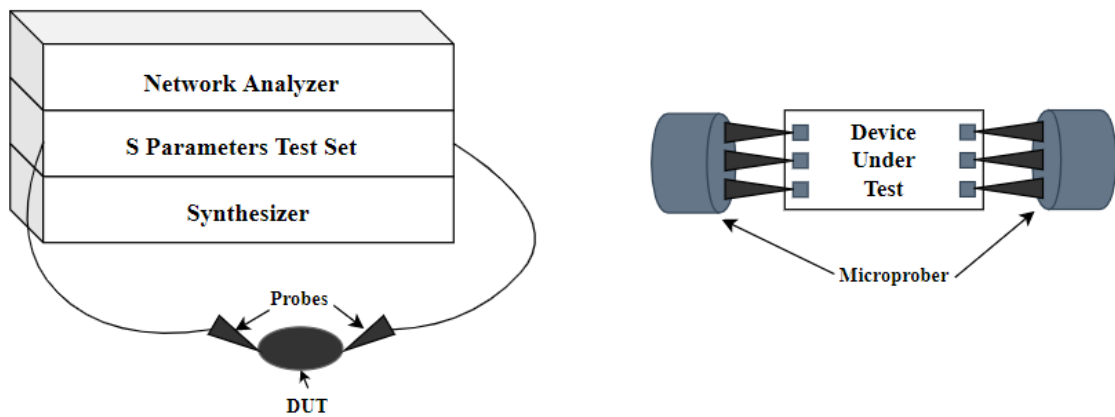
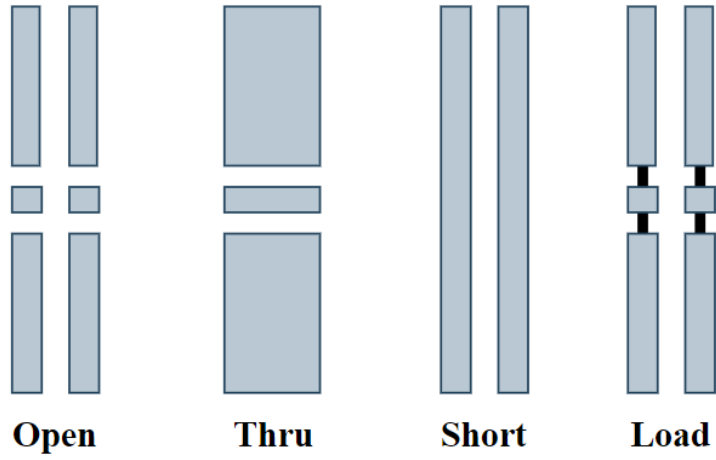


Fig.3.15 Measurement setup using GSG probes [101]



(a)



(b)

Fig.3.16 (a) GSG probe (b) calibration standards [101]

3.8 Measurement Procedure

Initially, the measurements are taken on as-deposited sample. This data is the OFF-state data of the device. As-deposited samples are in amorphous state. After taking the measurements, the sample is heated on the hot plate at 240 °C for about 5 mins and then cooled down. Heating at atmospheric pressure doesn't oxidize the sample as the passivation layer protects the GeTe thin film. However, if passivation layer is not present, then vacuum chamber should be used to avoid GeTe oxidization. After the sample cool down, measurements are again retaken on the same device to get the ON state data. The re-amorphization is still not achieved at the time of this report was published. The above procedure is used to get the ON and OFF state data of the device.

As shown in fig.3.13. the switch with three different gap sizes were fabricated and measured. GeTe is deposited in the gap between two electrodes. When GeTe is in OFF state i.e., high resistance state, all the signal is reflected. When GeTe is ON i.e., low resistance state, all the signal is transmitted making it a switch. Gap width of 5 μm , 10 μm , and 15 μm are used to demonstrate the switch behavior. Fig.3.17 and fig.3.18. shows the S parameter results of the devices. From the results we can see that as the gap size increase the insertion loss increases, with improved isolation. The 5 μm gap switch gives the best performance with 0.23 dB insertion loss at 15 GHz and 19.7 dB isolation at 15 GHz, when compared to 0.41 dB insertion loss with 22.76 dB isolation for 10 μm gap switch and 0.61 dB insertion loss with 23.6 dB isolation for 15 μm gap switch.

As the gap is increased, the isolation is increased but however the insertion loss is increased. For a switch, low insertion loss with large isolation is ideal.

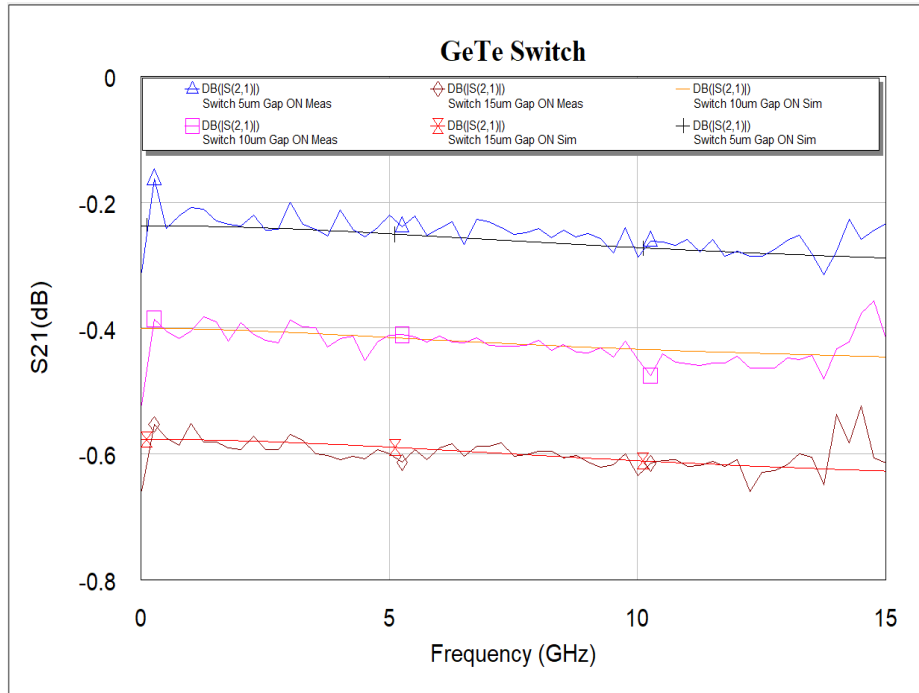


Fig.3.17 S_{21} magnitude ON state

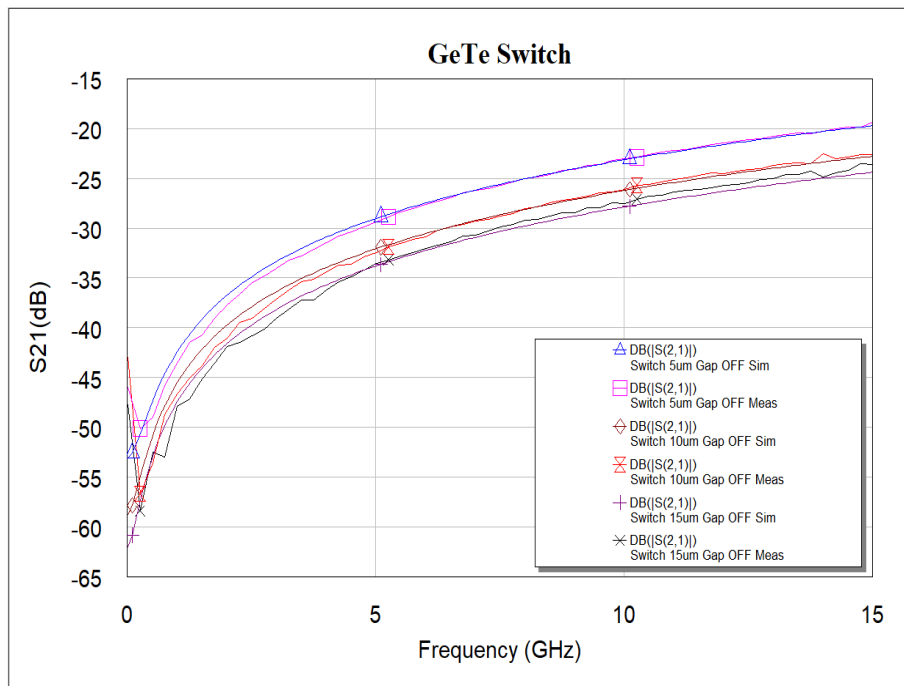


Fig.3.18 S_{21} magnitude OFF state

3.9 Circuit Model

The switch device shown in 3.13(b) without heater coil can be modeled using lumped components as shown in fig.3.19.

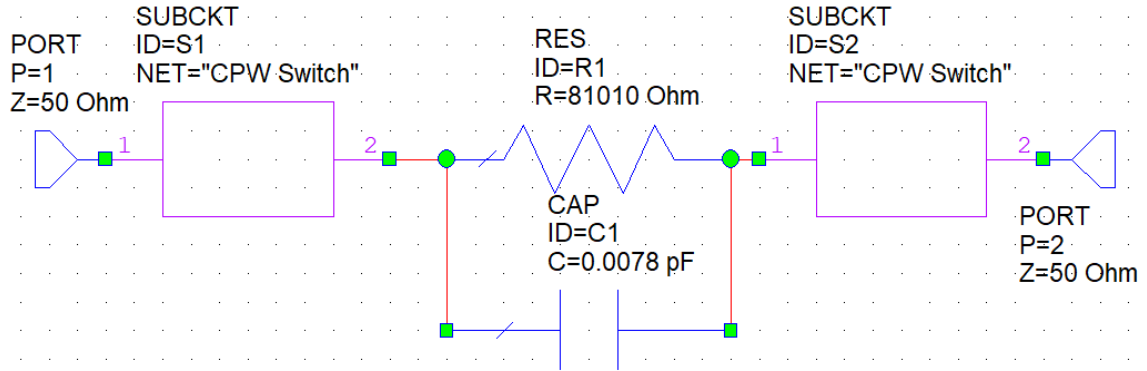


Fig.3.19 Circuit model shown for 10 μm gap switch in the amorphous state

Table.3.2 Extracted component values for switches with 5,10 and 15 μm gaps

Switch	Amorphous		Crystalline	
	R(Ohms)	C(pF)	R(Ohms)	C(pF)
5um gap	42310	0.0107	1.51	0.001
10um gap	81010	0.0078	3.43	0.001
15um gap	109000	0.0067	15	0.0067

From the table.3.2 we can see that the more than five orders of magnitude change in the resistance is obtained from the amorphous state to the crystalline state. The low ON state resistance and large OFF state resistance of GeTe makes it ideal for switching applications.

CHAPTER 4

ANALOG PHASE SHIFTERS

4.1 Introduction

Phase shifters are passive microwave devices with two ports that change the phase angle of an incoming RF signal at the out port (phase of S_{21}) in relation to the phase of the RF signal at the input port. A phase shifter (PS), in theory, modifies the insertion phase (phase of S_{21}) of a microwave device while maintaining the insertion gain (amplitude of S_{21}). Low insertion loss (IL), a wide phase tuning range, good linearity, small size, fast response speed, and high phase accuracy are all requirements for the PS, which must also minimize group delay fluctuation, DC power consumption, and nonlinear distortions.

The advancement in 5G has created enormous demand for the phase shifters circuits, which play an essential role in the beamforming of phase-array antennas. The phased array antennas are widely used for telecommunication and radar applications. About 2 – 10 thousand phase shifters are needed in different types of phased array antenna systems [37]. Several groups have demonstrated phase shifters for low frequencies in past. Recently few groups [102-103] have demonstrated a phase shifter at 60 GHz. The design is complex and big. Reproducibility, compatibility, and high-volume production are major requirements of commercial industry.

There are various types of RF phase shifters, such as switched-line [104], loaded-line [105], reflection [106], switched-filter [107], traveling wave [108] etc.

The phase shifter can be implemented as analog or digital phase shifters. Analog phase shifters provide a continuous phase shift that changes continuously with the input RF signal, mostly controlled by a voltage. Varactor is an example analog phase control device that changes capacitance with the applied voltage. Analog phase shifters have their own merits such as low loss and lower cost of components. The main limitations of analog phase shifters are imbalanced insertion loss, fabrication errors and narrow-band performance [109]. On the other hand, digital phase shifters provide phase shifts in multiple set of phase states that are controlled by two-state phase bits, where the states possess different insertion phases at microwave frequencies. The advantage of a digital phase shifter is that they are usually smaller in size, immune to noise, provide flat phase over wide bandwidth and easier to implement.

Ferroelectric thin film BST varactor shown in fig.2.7 is the basic building block for analog phase shifters. When there is no bias applied, the BST has high permittivity and the large capacitor to the ground shunts all the signal to the ground isolating the output port (P2). When the DC bias is applied to the signal line, the dielectric permittivity of the BST is decreased which decreases the capacitance to ground allowing signal to pass through, this also changes the CPW transmission line phase. When multiple units of single varactors are cascaded, the total phase shift adds up to reach 360° or more. As mentioned earlier varactor needs to be optimized to design a phase shifter at higher frequencies. Table.4.1 summarizes phase shifters using different technologies.

Table.4.1 Summary of phase shifters using different technologies

Reference	Device Technology	Operating Frequency (GHz)	Insertion Loss (dB)	Phase Shift (Deg)	Limitations
[110]	GeTe	26-34	4.9 @ 30 GHz	170 @ 30 GHz	Fabrication Process
[111]	CMOS	20-30	11 @28 GHz	360 @28 GHz	High insertion loss, low linearity and low power handling capability
[112]	RF – MEMS	26-30	5.35 @28 GHz	120@28 GHz	Fabrication process
[113]	RF – MEMS	1-20	3 @ 20 GHz	150 @ 20 GHz	Power consumption
[114]	Hafnium Zirconium Oxide (HZO)	10-80	5.84 @60 GHz	111 @60 GHz	Fabrication process
[115]	Barium Calcium Zirconate Titanate (BCTZ)	8 – 12	11 @ 12 GHz	285 @ 12 GHz	Fabrication process and high bias voltage
[116]	RF – MEMS	1-13	6.02 @ 13 GHz	125 @ 13 GHz	High bias voltage

4.2 2 μm x 2 μm Varactor

The objective is to design, fabricate and demonstrate a phase shifter up to 50 GHz with 360° phase shift for wide band with low insertion loss. At higher frequencies, the phase shifter has wider phase control range, but it also suffers higher insertion loss. With the proposed optimized design low insertion loss can be achieved with low control voltages, low leakage currents and high figure of merit (FOM). The CPW transmission line configuration can be easily integrated with other circuits on chip.

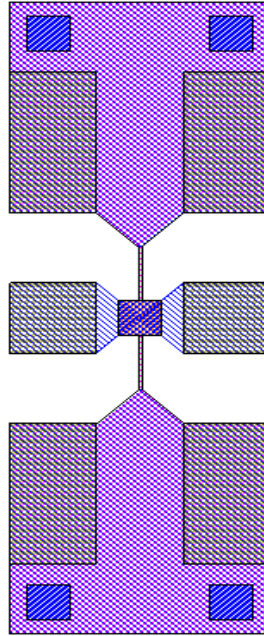


Fig.4.1 2 μm x 2 μm Varactor

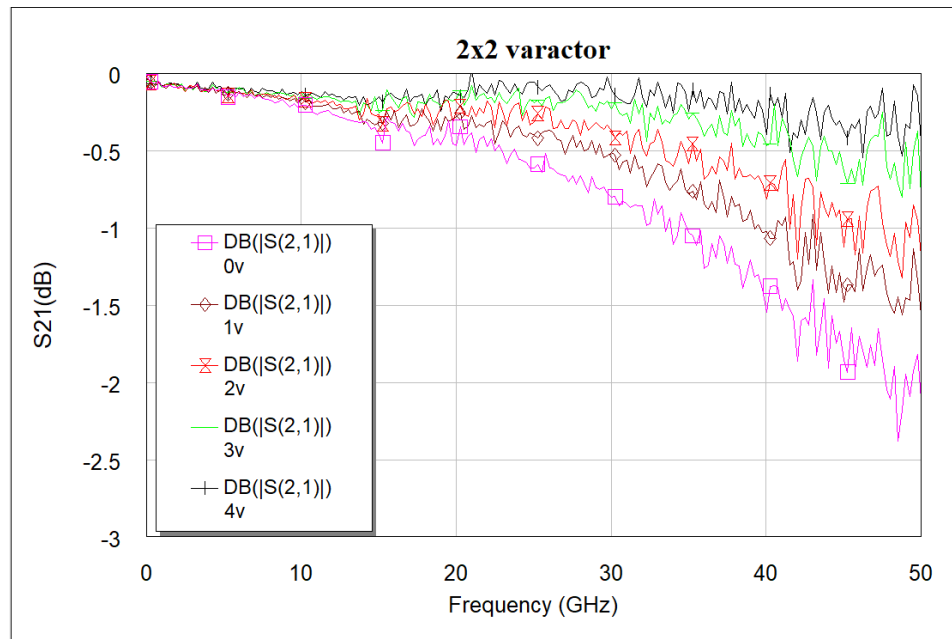


Fig.4.2 Measured S_{21} magnitude of a 2 μm x 2 μm varactor

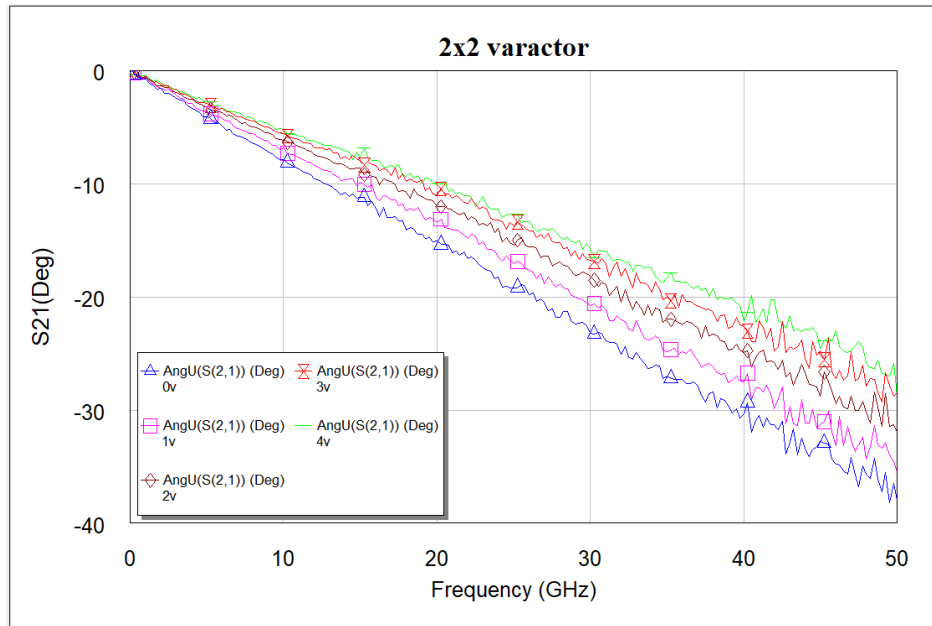


Fig.4.3 Measured S_{21} phase of a $2 \mu\text{m} \times 2 \mu\text{m}$ varactor

The $2 \mu\text{m} \times 2 \mu\text{m}$ varactor has very low insertion loss about 0.3 dB at 50 GHz and only up to 4 V is required to achieve maximum tuning, but however the phase shift is very less. To achieve a 360° phase shift from 24 GHz to 50 GHz many single units need to be cascaded. From our previous work [27], we have learned that cascading more than 15 units doesn't give much phase shift but however losses are high. Further modifications to the varactor are necessary.

Table.4.2 Extracted parameters for a $2 \mu\text{m} \times 2 \mu\text{m}$ varactor

Voltage	C (pF)	Rp (Ohms)	Ls (nH)	Rs(Ohms)
0v	0.07	3000	0.01	0.5
1v	0.06	3000	0.01	0.5
2v	0.5	3000	0.01	0.5
3v	0.3	3000	0.01	0.5
4v	0.017	3000	0.01	0.5

4.3 Dual Top 2 μm x 2 μm varactor

The new modified design helps to achieve larger phase shift with low insertion loss. Fig.4.4 shows the new modified design. The modified device can be seen in fig.4.4, Instead of one varactor overlap area, two varactor overlap areas of $2 \times 2 \mu\text{m}^2$ is used. This has better advantage over conventional design. With small area, more capacitance and phase shift are achieved. The new device has very low insertion loss of 0.9 dB with the dc bias of 10 V. The single varactor overlap area provides less phase shift, when compared to the dual top device which can be seen in fig.4.5 and fig.4.6 however, $2 \times 2 \mu\text{m}^2$ requires more units to be cascaded to achieve 360° phase shift, which is not an optimal solution in terms of size and losses.

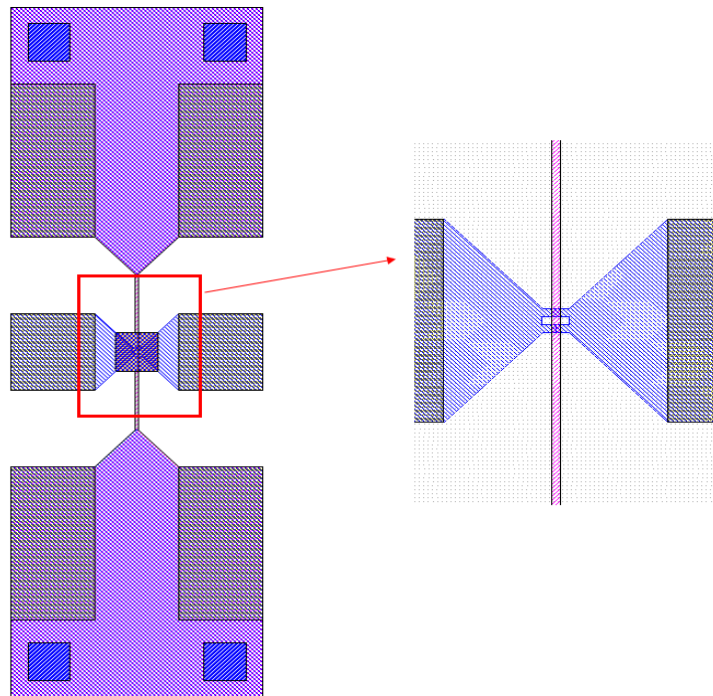


Fig.4.4 Dual top 2 μm x 2 μm varactor

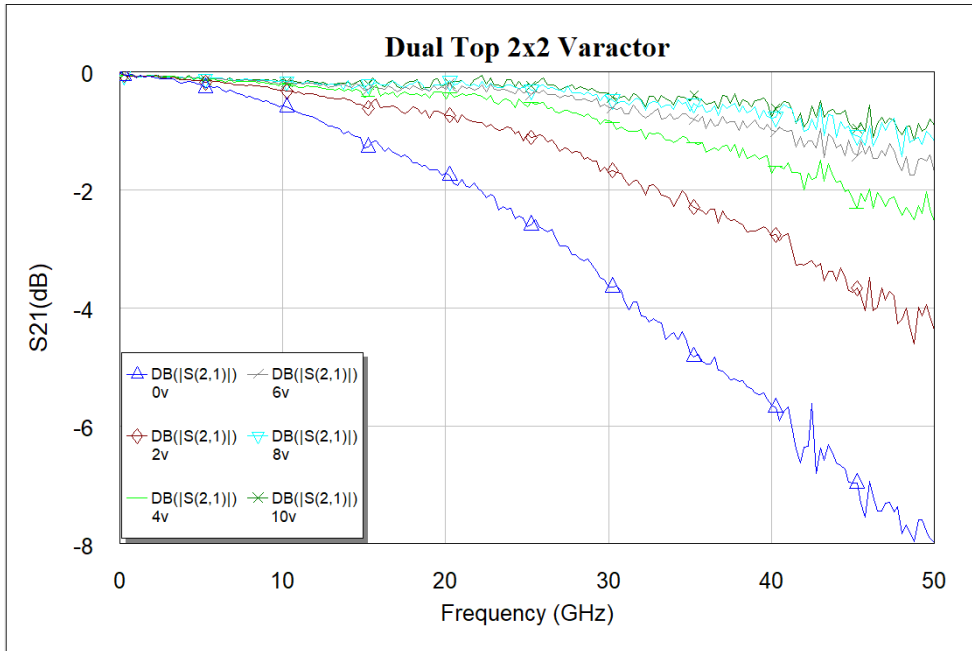


Fig.4.5 Measured S_{21} magnitude of a dual top $2 \mu\text{m} \times 2 \mu\text{m}$ varactor

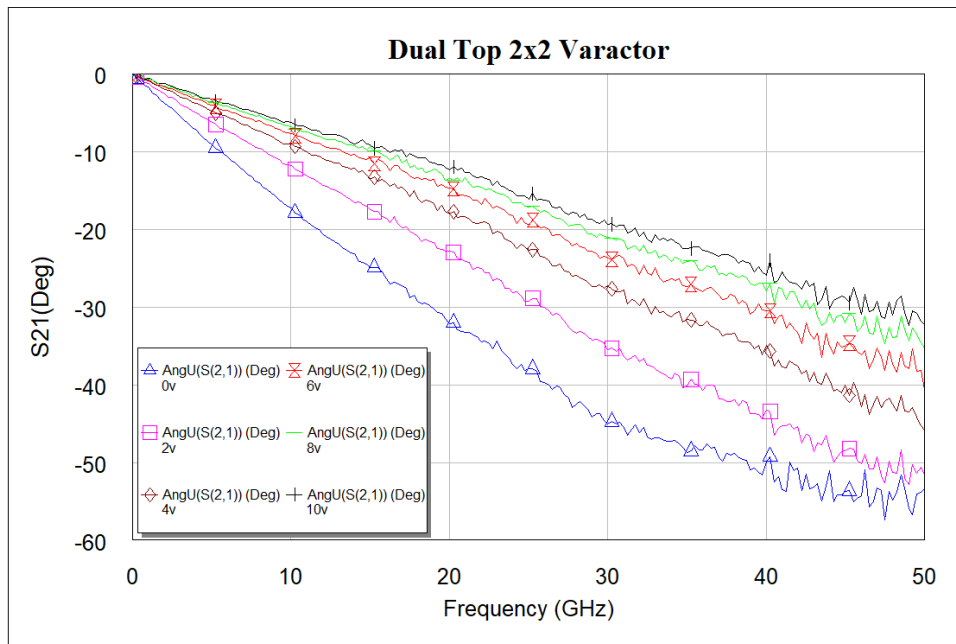


Fig.4.6 Measured S_{21} phase of a dual top $2 \mu\text{m} \times 2 \mu\text{m}$ varactor

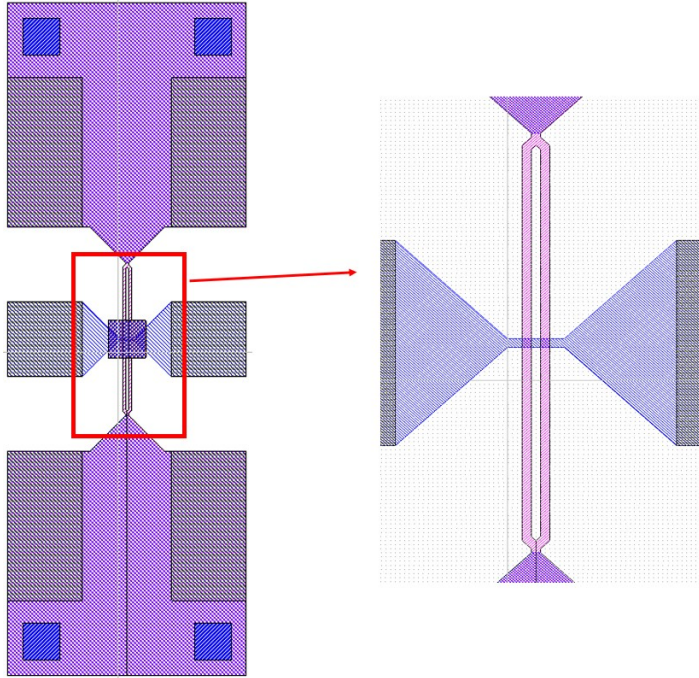
Table.4.3 Extracted parameters for a dual top 2 μm x 2 μm varactor

Voltage	C (μF)	Rp (Ohms)	Ls (nH)	Rs(Ohms)
0v	0.2	3000	0.01	0.5
2v	0.13	3000	0.02	0.5
4v	0.09	3000	0.02	0.5
6v	0.06	3000	0.01	0.5
8v	0.051	3000	0.01	0.5
10v	0.046	3000	0.01	0.5

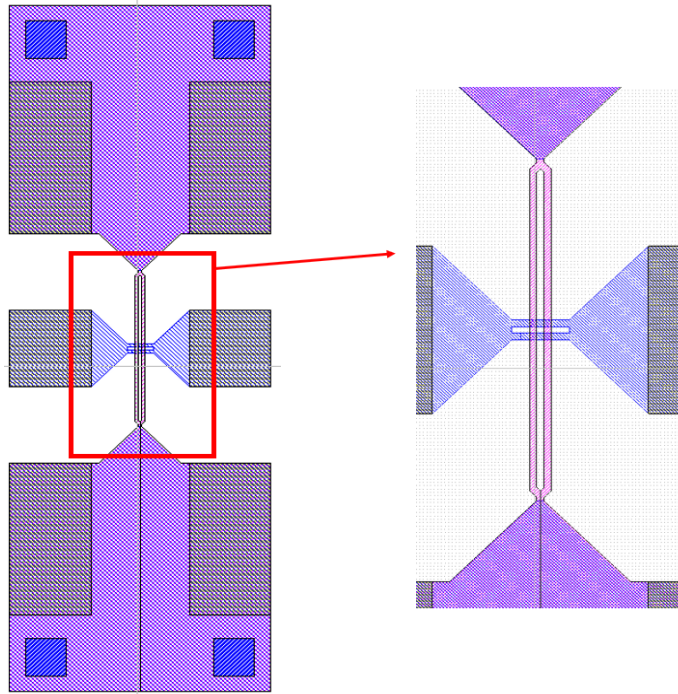
Table.4.3 shows the extracted values of the dual top 2 μm x 2 μm varactor. Several other varactor topologies as shown in fig.4.7 have also been investigated however the insertion loss is more, compared to dual top device, Table.4.4 summarizes the insertion loss at 10 V bias for each device.

Table.4.4 Insertion loss of modified varactors @ 10 V DC Bias

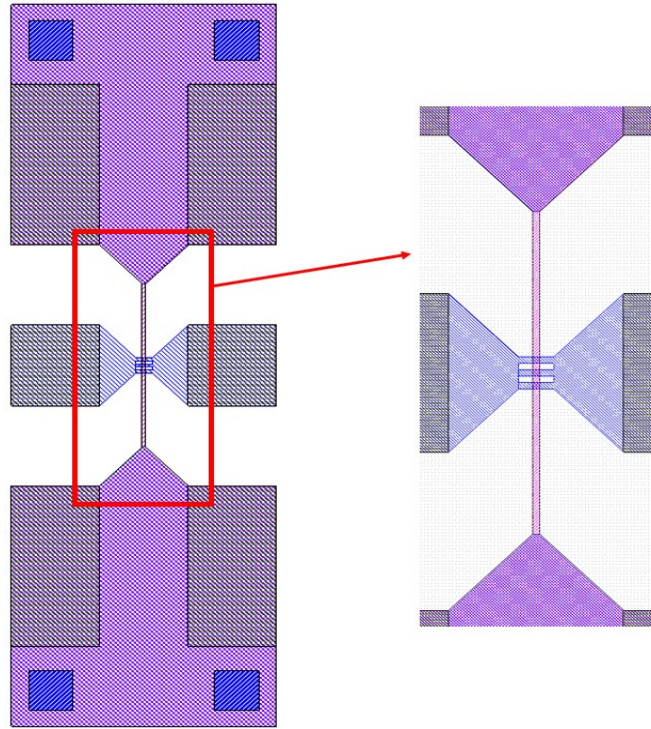
Modified Varactor Device	Insertion Loss @ 10V (dB)
Dual Top	-0.9
Dual Bottom	-1.6
Dual Top and Bottom	-2.7
Triple Top	-1.9
Triple Bottom	-2.08



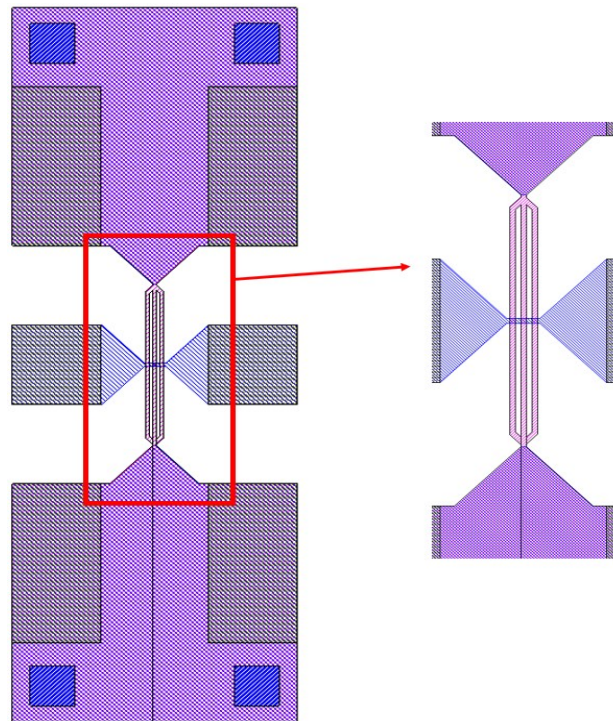
(a)



(b)



(c)



(d)

Fig.4.7 Varactor Devices (a) Dual Bottom (b) Dual Top and Bottom (c) Triple Top (d) Triple Bottom

4.4 Phase Shifter using Dual Top Varactor

A phase shifter device is designed using dual top varactor as shown in fig.4.8. 10 units of $3 \times 3 \mu\text{m}^2$ dual top varactors are cascaded. The frequency response is shown in fig.4.9. The noise in the results shown in fig.4.8 at 0 V bias and 2 V bias for frequencies above 30 GHz is due to the attenuation caused by the measurement setup.

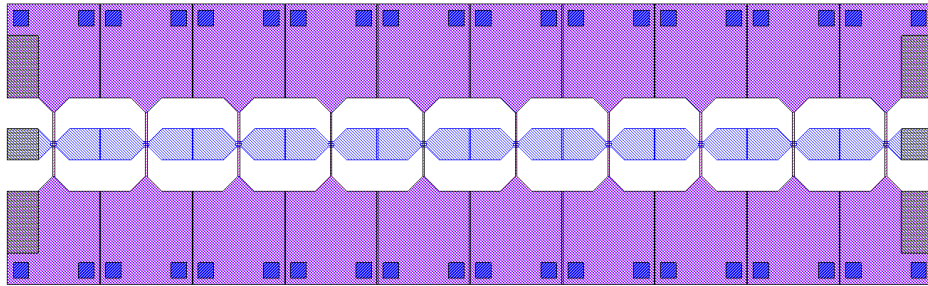


Fig.4.8 $3 \mu\text{m} \times 3 \mu\text{m}$ dual top varactor cascade 10 phase shifter

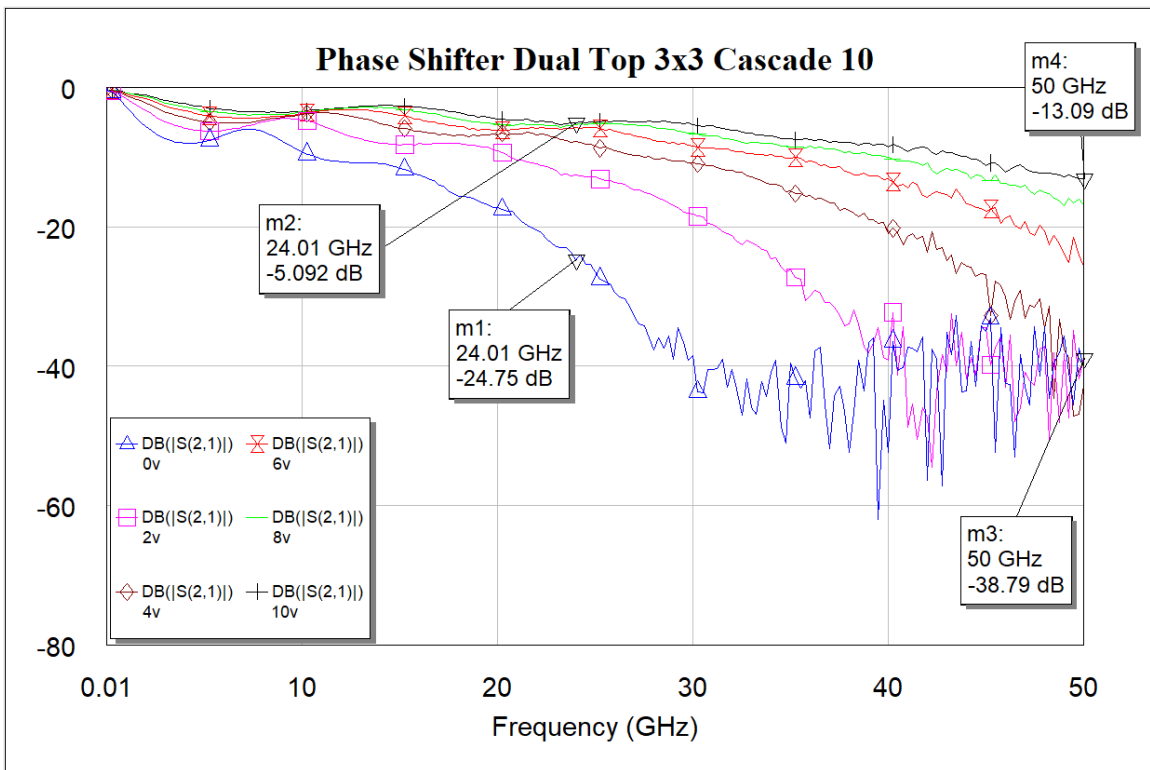


Fig.4.9 Measured S_{21} magnitude of dual top $3 \mu\text{m} \times 3 \mu\text{m}$ cascade 10 phase shifter

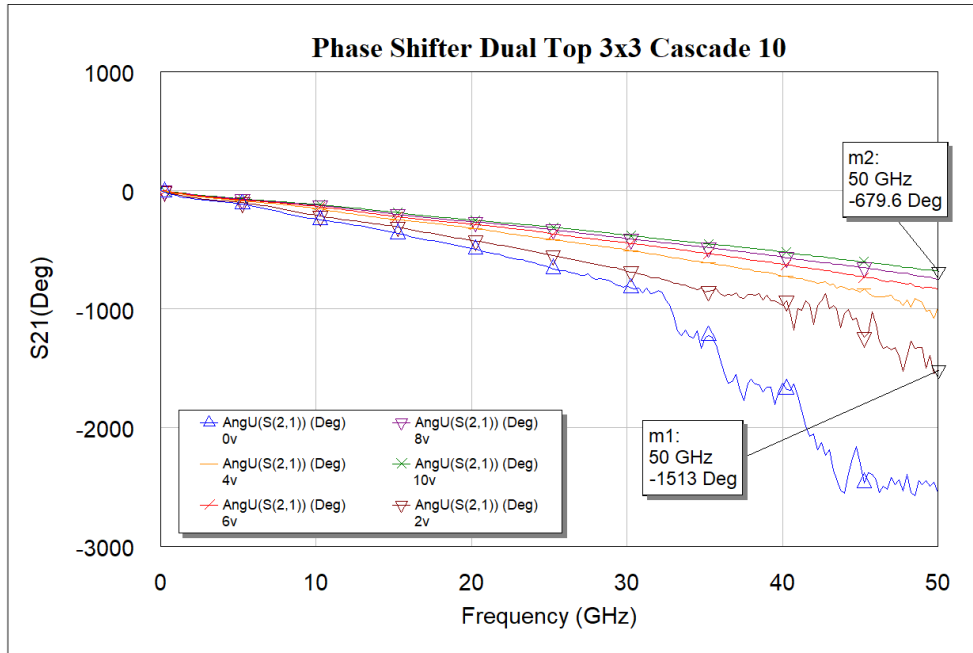


Fig.4.10 Measured S_{21} phase of dual top 3 μm x 3 μm cascade 10 phase shifter

The device at 0 V DC bias or zero-bias state of the phase shifter is in high insertion loss state. This is because of the high varactor shunt capacitance at zero-bias. At a dc bias of 10 V, the varactor shunt capacitance is reduced to a minimum resulting in more signal transmission for port1 to port2 and is considered as low insertion loss state. The insertion loss mainly depends on the number of stages cascaded of the phase shifter and the frequency. As the number of stages of the phase shifter is increased, insertion loss is increased and same applies with frequency, as the frequency increased, the insertion loss is increased. The phase shift is the difference between the phase of S_{21} at 0 V and the phase of S_{21} at 10 V. Maximum transmission losses, phase control range and FOM can be compute using Equation 4-1,4-2 and 4-3.

$$\text{Maximum Transmission Loss } (f_0) = ||S_{21}(0V, f_0)|_{dB} \quad 4-1$$

$$\text{Phase Control Range } (f_0) = |\angle S_{21}(0V, f_0) - \angle S_{21}(10V, f_0)| \quad 4-2$$

$$FOM = \frac{\text{Phase Control Range } (f_0)}{\text{Maximum Transmission Loss } (f_0)} \left(\frac{\text{degree}}{dB} \right) \quad 4-3$$

The overlap area of the varactor is increased, the phase shift is increased with lower insertion loss when compared to conventional varactors. With the conventional varactors more units are to be cascaded to achieve larger phase shift. As the number of cascade units are increased, the phase shift increases but the insertion loss increases as well. From fig.4.9 and fig.4.10., due to the distortion caused by the measurement setup the phase shift and FOM @ 50 GHz is calculated between 2 V bias and 10 V. A phase shift of 317 ° (0 V – 10 V) is achieved at 24 GHz and 833.4 ° at 50 GHz (2 V-10 V), however the phase shift is greater than that @ 50 GHz. Table.4.5 summarizes the results of the dual top 3 μm x 3 μm varactor cascade 10 @ 24 GHz. And Table.4.6 summarized the results of the dual top 3 μm x 3 μm varactor cascade 10 @ 50 GHz.

Table.4.5 Summary of results of dual top 3 μm x 3 μm cascade 10 phase shifter @ 24 GHz

Bias	Mag @ 24 GHz (dB)	Phase @ 24 GHz (Deg)
0 V	-24.75	-612.5
10 V	-5.092	-295.6

Table.4.6 Summary of results of dual top 3 μm x 3 μm cascade 10 phase shifter @ 50 GHz

Bias	Mag @ 24 GHz (dB)	Phase @ 24 GHz (Deg)
0 V	-38.79	-1513
10 V	-13.09	-679.6

4.5 Phase Shifter with PCM

Adding phase change material along with BST has improved the performance of the phase shifters. GeTe is used in conjunction with BST to improve the phase shift. At room temperature (20 °C) GeTe is in high resistance state. At 240°C, it has the low resistance state which acts as a metal. Using this property, we can have an extra overlap area which forms a varactor at high temperature. This helps in getting additional phase shift whenever needed, as we have seen that the larger the capacitance, the larger the phase shift as well as the insertion loss. Better performance with reduced size and losses can be achieved with adding a GeTe stub as shown in the Fig.4.11 (b) to the varactor design. Fig.4.11 shows modified 3x3 μm varactor with GeTe.

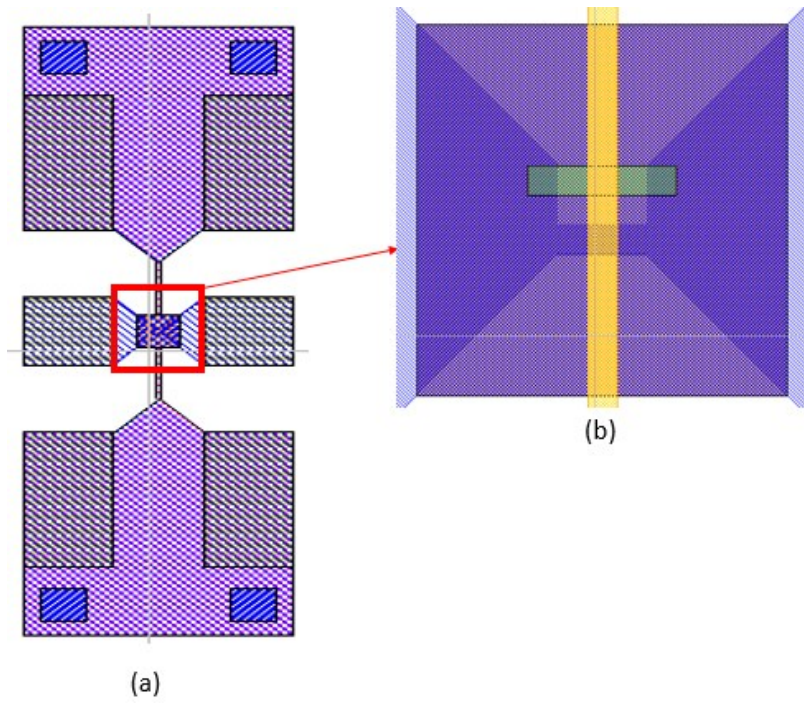


Fig.4.11 (a) Modified 3x3 μm^2 varactor with GeTe (b) magnified drop out

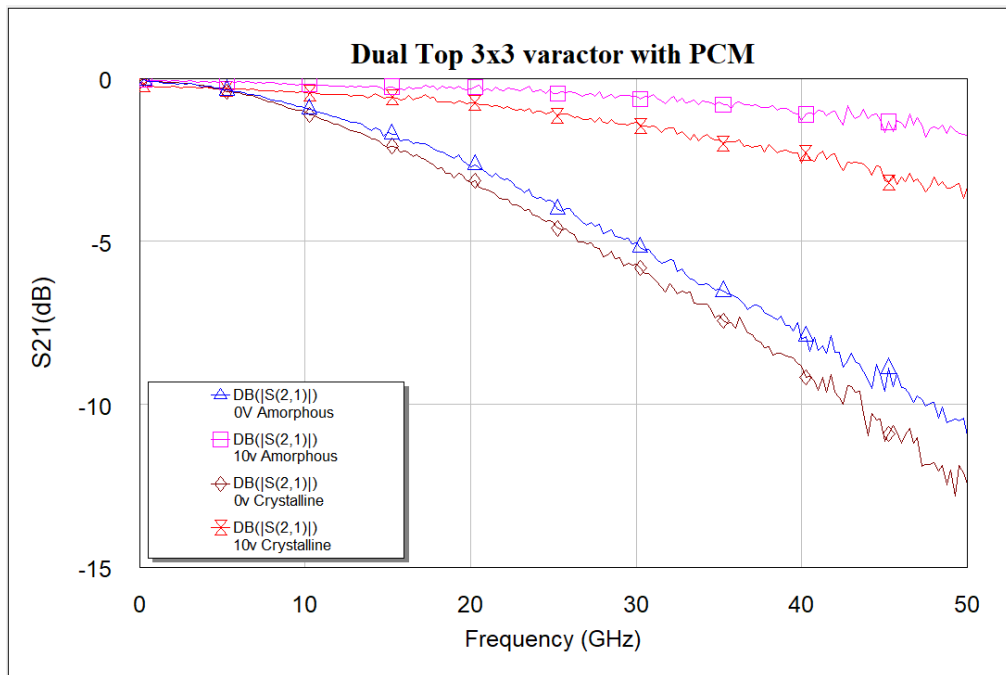


Fig.4.12 Measured S_{21} magnitude of dual top 3 μm x 3 μm varactor with PCM

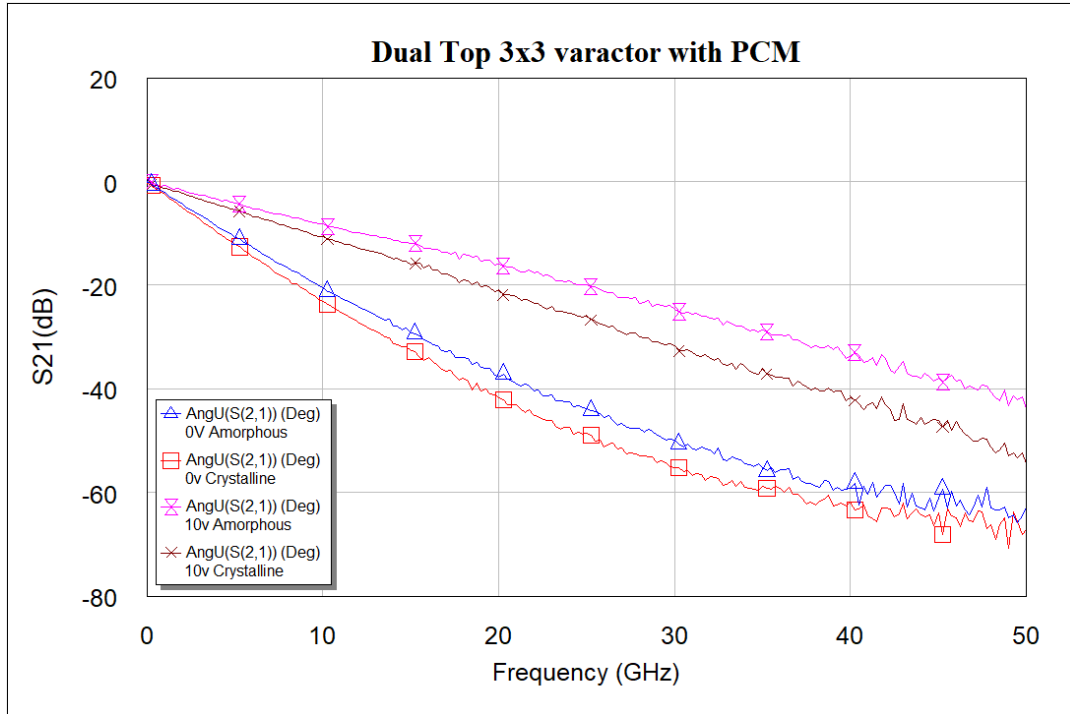


Fig.4.13 Measured S_{21} phase of dual top $3 \mu\text{m} \times 3 \mu\text{m}$ varactor with PCM

Electrical model shown in fig.2.12 is used to extract the parameters of the above varactor.

Table.4.7 Extracted parameters of dual top $3 \mu\text{m} \times 3 \mu\text{m}$ varactor with PCM

Voltage	C (pF)	Rp (Ohms)	Ls (nH)	Rs(Ohms)
0v Amorphous	0.27	3000	0.012	0.5
10v Amorphous	0.05	3000	0.012	0.5
0v Crystalline	0.315	3000	0.012	0.5
10v Crystalline	0.1	1000	0.012	0.5

From the above table.4.7 we can see that 6.3:1 tuning is achieved by adding PCM material. With normal varactors only about 4:1 tuning is achieved. Which is about 57% increase in tuning. A phase shifter is designed using this varactor with 10 units cascaded as shown in fig 4.14.

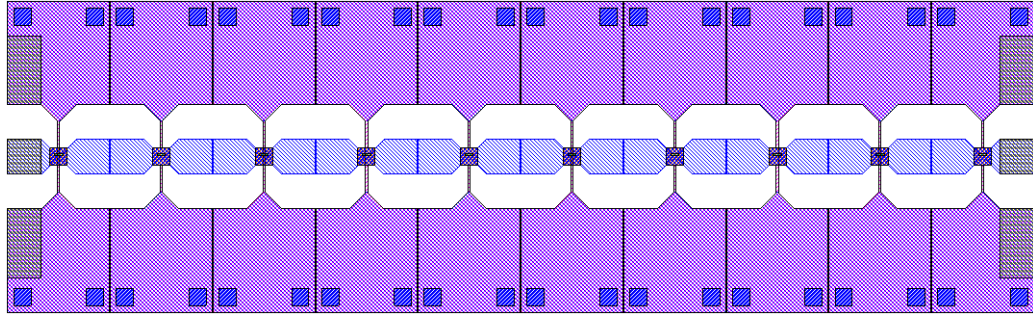


Fig.4.14 Dual top 3 μm x 3 μm varactor with PCM cascade 10 phase shifter

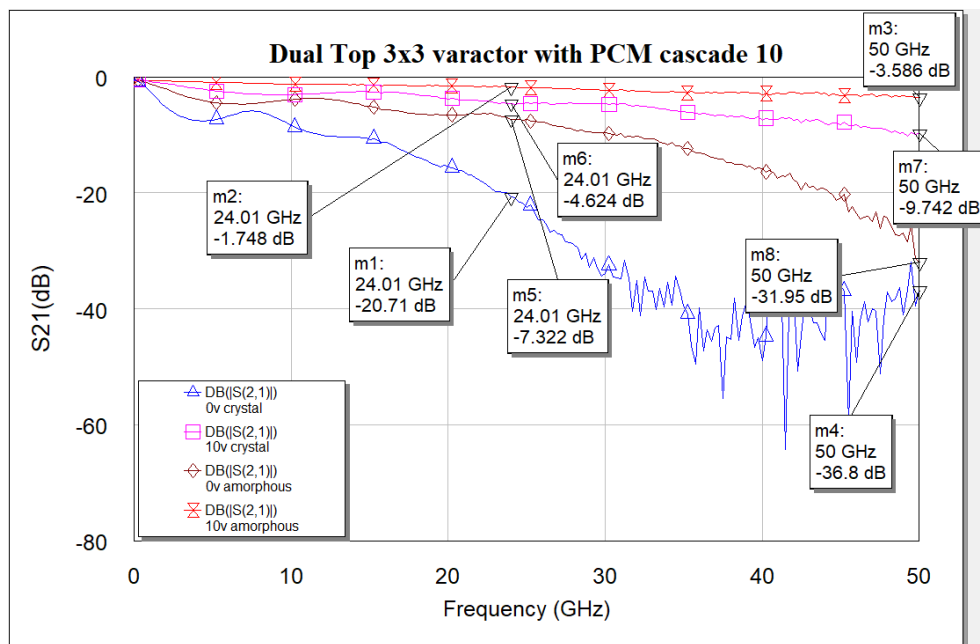


Fig.4.15 Measured S_{21} magnitude of dual top 3 μm x 3 μm varactor with PCM cascade 10 phase shifter

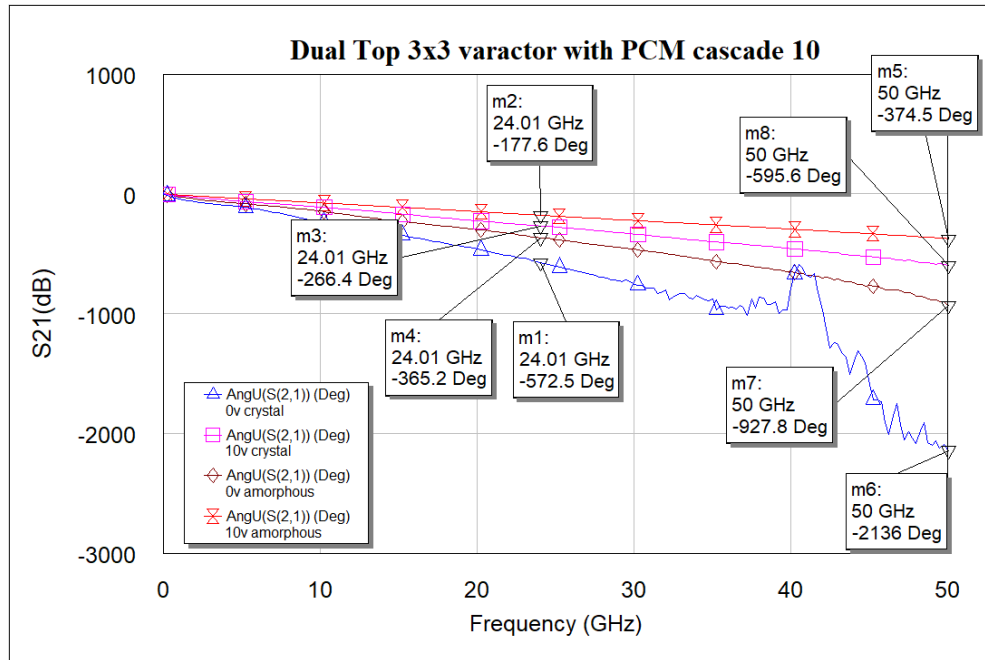


Fig.4.16 Measured S_{21} phase of dual top $3 \mu\text{m} \times 3 \mu\text{m}$ varactor with PCM cascade 10 phase shifter

We can see in Fig 4.14 and Fig 4.15 that when GeTe is in low resistance state it acts as metal and forms two $3 \times 3 \mu\text{m}^2$ capacitors for each device. But when the GeTe is not in its conducting state, there is only one single capacitor to ground, which reduces the phase shift and insertion loss as well.

Table.4.8 Summary of results of dual top $3 \mu\text{m} \times 3 \mu\text{m}$ varactor with PCM cascade 10 phase shifter

Bias	Mag	Mag	Phase	Phase	Mag	Mag	Phase	Phase
	@24GHz	@24GHz	@24GHz	@24GHz	@50GHz	@50GHz	@50GHz	@50GHz
	(dB)	(dB)	(Deg)	(Deg)	(Deg)	(Deg)	(Deg)	(Deg)
	PCM-							
	OFF	ON	OFF	ON	OFF	ON	OFF	ON
0v	-7.322	-20.71	-365.2	-572.5	-31.95	-36.8	-927.8	-2136
10v	-1.748	-4.624	-177.6	-266.4	-3.586	-9.742	-374.5	-595.6

Clearly, from the above table.4.8., a 395° phase shift is achieved @24 GHz, and 1761.5° phase shift is achieved @ 50GHz. Thus, adding a PCM stub provides additional tuning.

Table.4.9 Comparison of FOM of the phase shifters with and without PCM

Bias	Figure of Merit of PS without PCM	Figure of Merit of PS with PCM
@ 24 GHz	12.8	19.07
@ 50 GHz	> 21.5	< 46.64

We can see that the phase shift @24 GHz for the phase shifter with no PCM is 316° whereas, adding PCM the phase shift between 10 V DC-bias with PCM in amorphous state and 0 V DC-bias with PCM in crystalline state is 395° , which gives the desired phase shift @24 GHz. This is because @10 V bias, and PCM in the off state there is only one capacitor shunted to ground and as this capacitance is lower than having two capacitors to ground, more signal will be passing through the phase shifter resulting in lower insertion loss and larger phase shift.

The FOM @ 50 GHz as shown in the table.4.9, the phase shifter without PCM the FOM is calculated using 2 V to 10 V so the overall FOM would be greater than the given value. Whereas the FOM for phase shifter with PCM, the value of insertion loss at 0 V with PCM (ON state) could be more than the given value. So, the FOM could be less than 46.64 degree /dB. However, adding the PCM to the phase shifter is an advantage, additional tuning can be achieved.

A phase shifter with 360° phase shift throughout the high frequency spectrum of 5G i.e., 24 GHz to 50GHz has been demonstrated in this chapter.

CHAPTER 5
TUNABLE BAND STOP FILTER DESIGN USING DEFECTED GROUND
STRUCTURE

5.1. Introduction

Filters are the most important circuit block of the modern communication systems. Multiple filters are often used in a system to cover a large frequency bandwidth. Having a tunable filter would reduce the number of filters that need to be integrated into the system. Currently, in industry, acoustic filters are used but however their operation is limited to 6 GHz. Tunable filters were demonstrated previously [117-118] have used discrete components. In this chapter a novel tunable band stop filter design technique is demonstrated.

Electromagnetic Band Gap (EBG) structures like photonic band gap (PBG) structures are periodic structures which have defects in the ground plane. PBGs initially were researched mostly in the optical frequencies and the concept can apply to wide range of frequencies. They are used in many applications such as lasers, antennas many other devices. PBG's can provide band gap characteristics with periodic defects in the ground plane [119-123]. PBG's are difficult to use for microwave and millimeter wave components. This is mainly due to difficulties in modeling. And moreover, the radiation from the periodic defects was another concern.

A defected ground structure (DGS) is like that of photonic band gap structure which have defects in the metallic ground plane. These etched defects in

the ground plane disturb the shielding current distribution, which alters and rise the inductance and capacitance of the line [124]. The shielded current distribution depends on the shape and dimensions of the defect and the band gap property relies on many design parameters such as lattice shape, lattice spacing, and number of lattices [125]. Ahn et.al. [125] have proposed DGS by introducing a thin slot in between the two square shaped PBG cells. Previously our group has done several projects on DGS [126-128]

Defected ground structures can be used over a wide range of frequencies which gives the engineer an extra degree of freedom to design. First DGS was proposed in 1999, later many researchers have proposed many designs that has boosted the applicability of DGS. The main advantage of DGS over PBG is the circuit area, for DGS the circuit area is relatively very small when compared to PBG as few DGS elements can achieve similar parameters as periodic PBG and can show slow-wave effect.

Another advantage of DGS is by cascading the unit cell we can achieve deeper and steeper stop band depending on the number of cells. The cascading can be in both horizontal and vertical direction but with the conventional planar transmission line, vertical cascading is not possible. Cascading must be done along the transmission line direction.

The etched section of DGS increases the series inductance which in turn increases the reactance of the microstrip with increase in frequency. This gives a start for the rejection of certain frequency range. The attenuation pole location is

provided by the series inductance in parallel with the capacitance. This acts like a parallel LC resonator. The unwanted surface waves and leakage and spurious signals can be suppressed with stopband characteristics of DGS. The reactance of capacitance is decreased with the increase in frequency. The resonant frequency is given by

$$f = \frac{1}{2\pi\sqrt{lc}}$$

5-1

Where l is the inductance and c is the capacitance of the device. DGS can provide sharp selectivity at cutoff frequency and excellent performance in terms of spurious signals in stop band and ripples in pass band [124]. Using DGS we can suppress harmonics too. Many researchers have combined DGS with new materials to achieve special characteristics like tunability and more.

The LC equivalent components of DGS causes slow wave effect which is one of the most important advantages of DGS. The transmission line with DGS when compared to conventional lines has higher impedance and slow wave factor [124]. With these properties the circuit sizes can be reduced significantly. DGS has many applications like in microwave oscillators, microwave couplers to increase the coupling, microwave filters, microwave amplifiers etc. DGS is also used in microstrip antenna design for different applications such as antenna size reduction, cross polarization reduction and harmonic suppressions.

DGS is also used in beam steering of antenna performance. The impedance of a conventional microstrip line was limited to around $100 \Omega \sim 130 \Omega$ which was

a serious problem. This is overcome by using DGS in the metallic ground plane, which leads to increase in the impedance of the microstrip line more than 200Ω [124]. In [124], 1:6 unequal Wilkinson power divider was proposed which was designed using DGS. In this power divider, the microstrip line of characteristic impedance 208Ω could be achieved by using a rectangular block defect. One can also use this advantage of high characteristic impedance in digital systems. A detailed explanation about DGS is provided in [127]. In this work, CPW configuration is used.

5.2 Dumbbell DGS

The dumbbell DGS has narrow and wide etched areas as shown in fig.5.1. These defects increase the effective inductance and capacitance of the transmission line. The rectangular patch “ $a \times b$ ” have the dimension of 260×150 mil and the gap width “ g ” was initially assumed to be 20 mil.

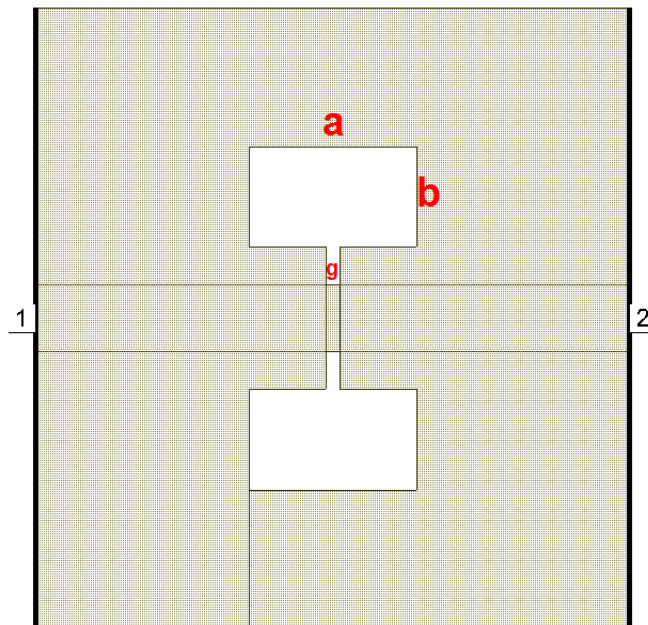


Fig.5.1 Dumbbell DGS on microstrip line

5.2.1 Influence of the Square Lattice “a x b”

The frequency responses for different rectangular etched areas are shown in the fig.5.2. To investigate the influence of the rectangular lattice dimension, the rectangular etch has been varied, it is simulated for 2 different dimensions of 260 mil x 150 mil and 300 mil x 170 mil keeping the etched gap width “g” under the conductor line constant. The rectangular etch increases the series inductance to the microstrip line which introduces cutoff characteristics at some frequencies. The increase in series inductance gives rise to lower cutoff frequencies. The attenuation pole can be explained by the parallel capacitance with the series inductance. Therefore, the attenuation pole location becomes lower with increase of series inductance.

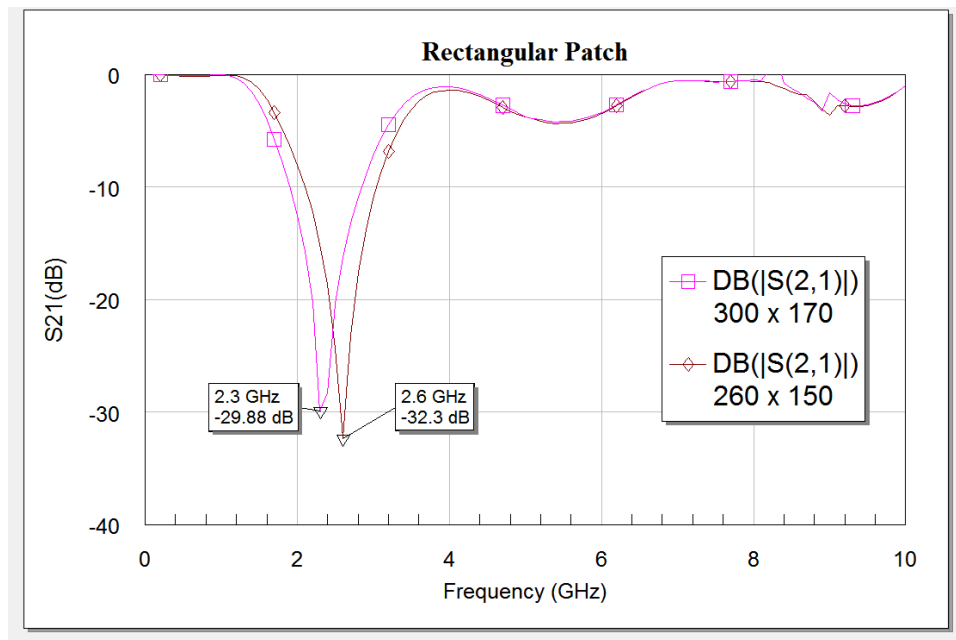


Fig.5.2 Influence of rectangular lattice dimensions

From the fig.5.2. we can see attenuation poles in the simulation result. These occurred because of the parallel capacitance and the series inductance. In this case the capacitance was constant as the etched gap 'g' was kept constant. As the series inductance increase the resonance frequency decreases [125].

5.2.2 Influence of the Gap Distance “g”

Now the rectangular etched area is kept constant at 260 mil x 150 mil. The gap distance “g” is varied. As the rectangular etched areas are constant the effective series inductance is also constant. Since the series inductance is constant, there would be no change in the cutoff frequency though the gap distance is varied. This shows the gap etched underneath the conductor line does not affect the series inductance. The change in the gap distance only affects the effective capacitance. If the gap distance is increased, then the capacitance is reduced then the attenuation pole moves to higher frequency. The fig.5.3. shows the effects of variation in the gap distance.

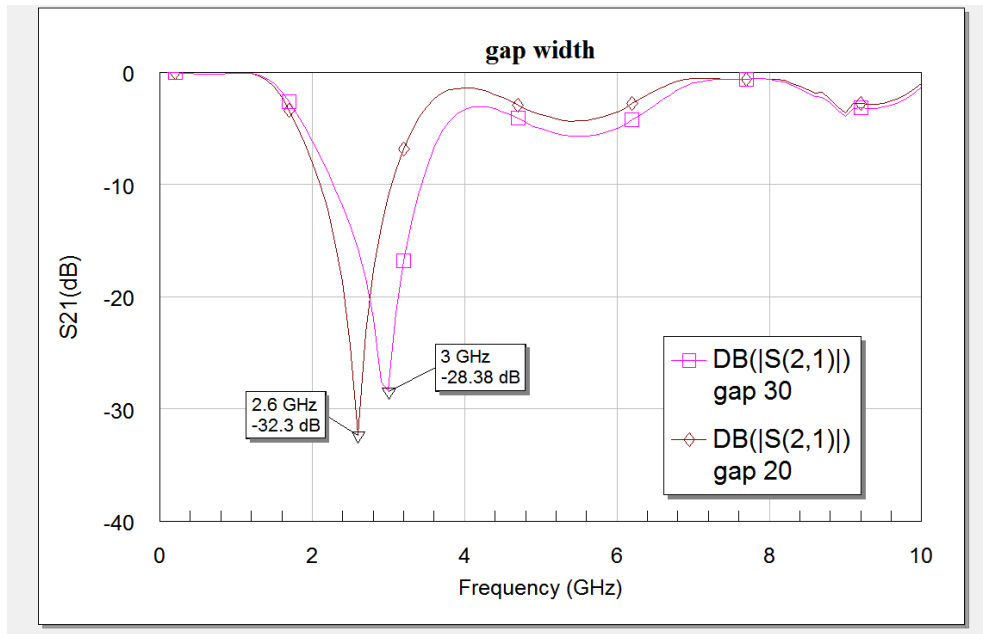


Fig.5.3 Influence of gap distance

5.3 U-Slot DGS

The U-Slot has two slots of width “g” along the transmission line in the ground plane as shown in fig.5.4. These two slots relate to another slot of width “c”. The length of the two slots is denoted by “L”. And the two slots are separated by a distance “d”. Now let’s look at each parameter influence on frequency response.

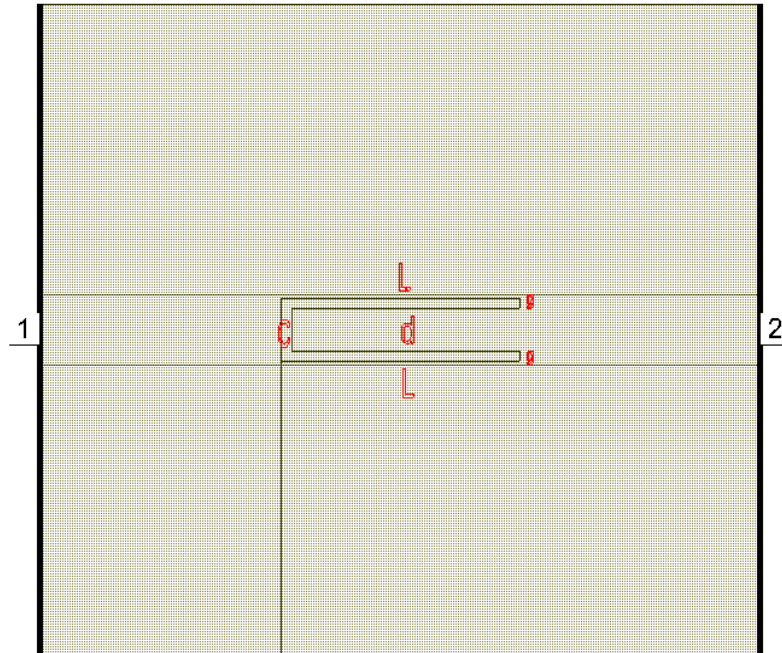


Fig.5.4 U-slot DGS on microstrip line

5.3.1 Influence of Length “L”

Assuming the values $d=60$ mil and $c=g= 15$ mil, the length “L” is varied. The figure 5.5 shows the characteristics of the u-slot with different lengths. As we can see when the length ‘L’ increases, the stopband bandwidth, and the resonance frequency decrease. As the length of the slot increases the inductance and the capacitance both increases. The Q is not affected by the change in the slot length.

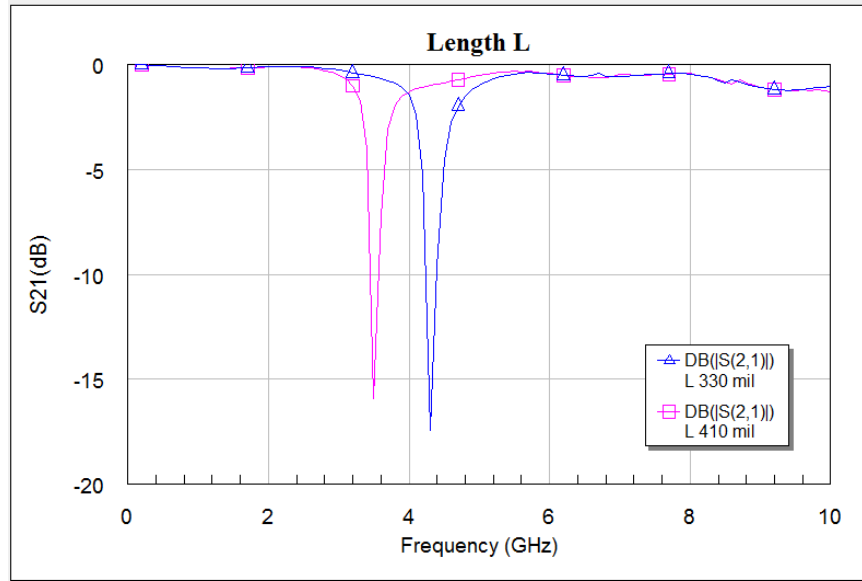


Fig.5.5 Influence of length L on frequency response of u-slot

5.3.2 Influence of Distance “d”

The values of $L = 350$ mil and $g=c = 15$ mils are kept constant and the distance between two slots is varied. When distance between two slots d is reduced Q-factor is increased. The decrease in d gives rise to increase in capacitance. Fig.5.6. shows the variations of the distance between two slots. And if the distance is increased the Q-factor is reduced and gives lower capacitance.

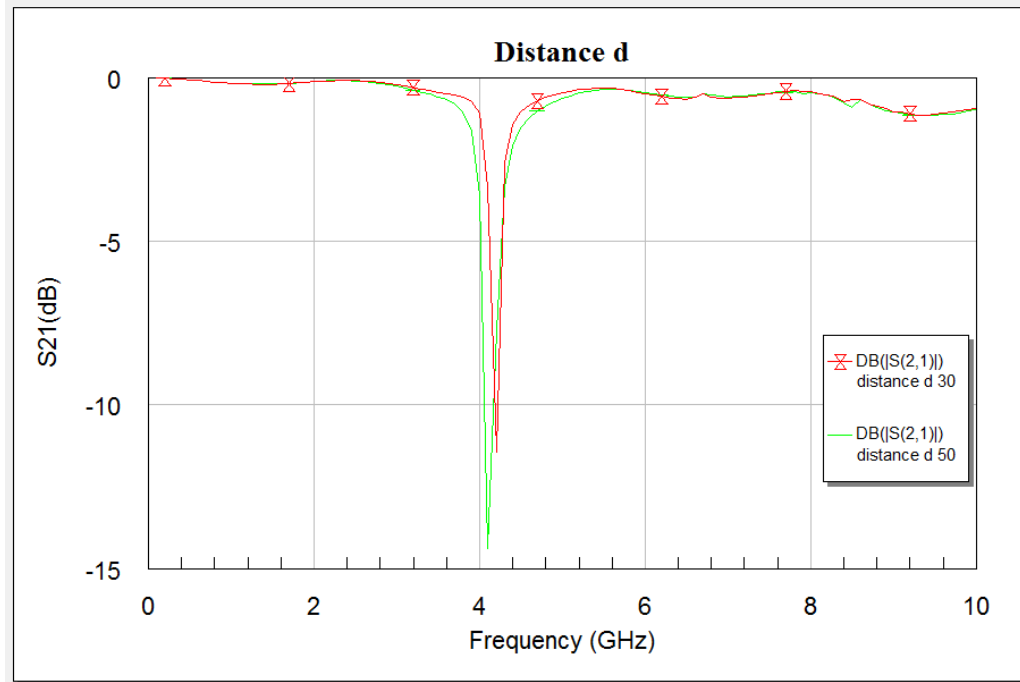


Fig.5.6 Influence of distance d on frequency response of u-slot

5.3.3 Influence of Width of the Slot “g”

To investigate the effect of the slot width “g” on the frequency response the length of the slot $L=350$ mil, $d=40$ mil, and $c=15$ mil, are kept constant. The width of the g is varied and the figure 5.7 shows the frequency response for the influence of the width of the slot “g”.

When the slot width grows, the equivalent capacitance decreases and the equivalent inductance increases, the resonance frequency slowly decreases due to the increase in inductance. The Q-factor increases as the slot width decreases. As the slot width decreases, the increase in capacitance causes the increase in Q-factor [129].

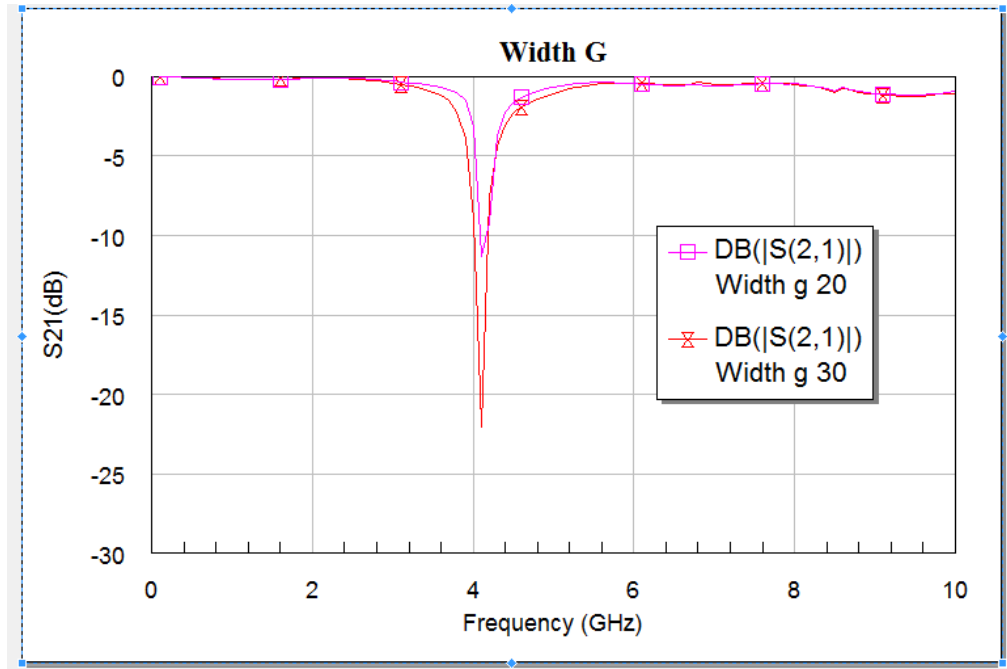


Fig.5.7 Influence of width of g on frequency response of u-Slot

These results are obtained using microstrip transmission line structure designed on a PCB board with ϵ_r of 10. However, CPW structure is easier to fabricate on wafer and integrate with other electronics. Thus, we will use CPW transmission line for our design. Moreover, using BST thin films we can achieve tunable band stop filters. However, the analysis discussed earlier is still valid for CPW based DGS structures.

5.4 Dumbbell DGS using CPW

The design of Dumbbell DGS on CPW is like that of the microstrip transmission line, the only difference is that the ground plane and the signal line are on one plane as shown in fig.5.8. The dimensions “a x b” used here are “400

$\mu\text{m} \times 230\mu\text{m}$ and the gap width “g” is “ $10 \mu\text{m}$ ”. Using high dielectric material like BST we can get large capacitance and inductance values of the defects in the ground plane making its size small. The frequency response of dumbbell DGS is shown in fig.5.9.

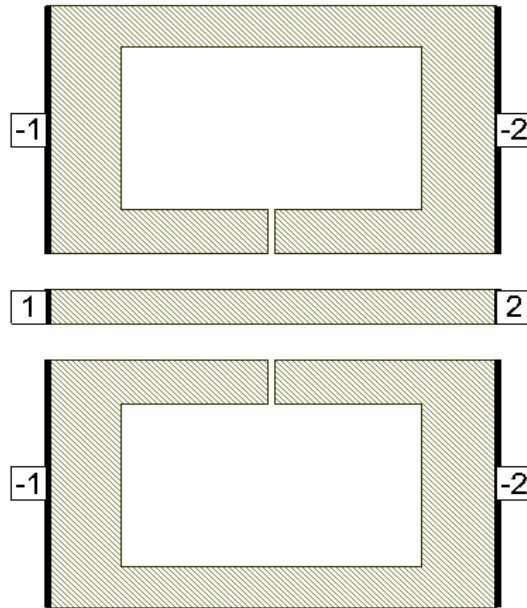


Fig.5.8 Dumbbell DGS on CPW line

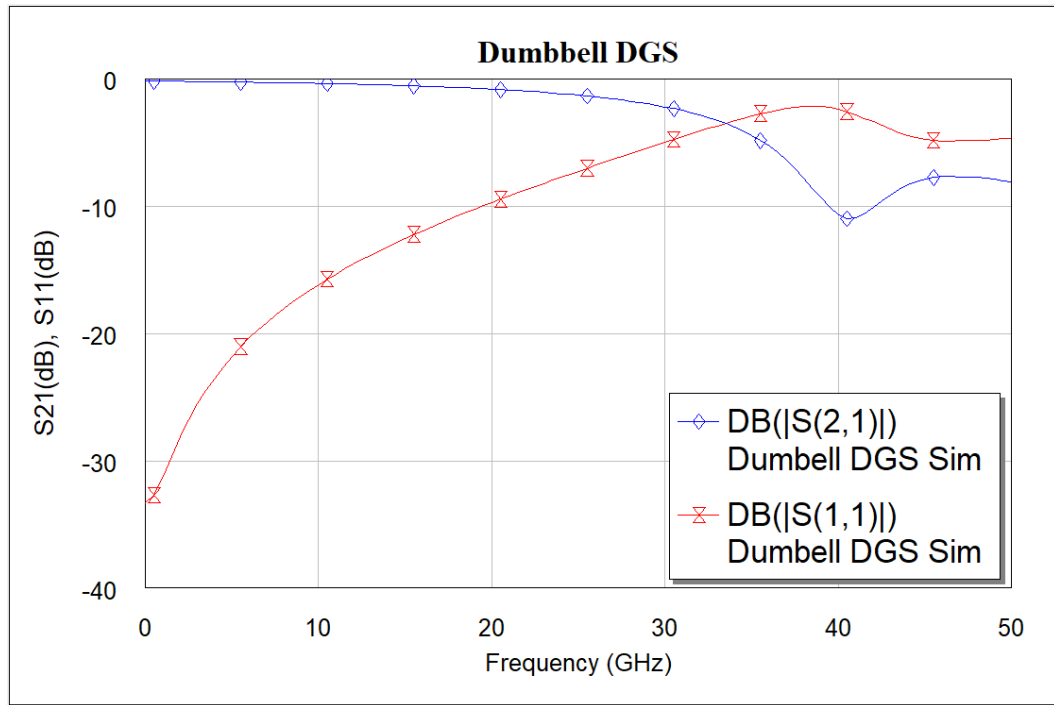


Fig.5.9 Simulated frequency response of dumbbell DGS

BST $\epsilon_r = 700$ is used for all the simulations used in this chapter. Smaller values of ϵ_r gives lower capacitance and inductance which shifts the notch outside of our frequency of interest. To shift the resonance to lower frequency we must increase the inductance and capacitance i.e., we must increase the defect dimensions as discussed earlier. This will in turn increase the size of the filter. Fig.5.9 shows the simulated frequency response for the CPW based dumbbell DGS. Fig.5.10 shows the measured results for Dumbbell DGS and fig5.11 shows comparison of measurements to that of simulations. From the measured results the dumbbell DGS resonates around 50 GHz. The RF performance of the new proposed filter DGS can be modeled using lumped elements. In general, the DGS section can be modeled by parallel LC resonator circuit for many applications. But by considering the losses into account it can be efficiently modeled by parallel RLC

resonant circuit. The resistance is due to losses in the conductor, leakage resistance of the dielectric, and radiation losses. The circuit model is shown in fig.5.12. The circuit parameters were extracted using AWR tool which provides a variable tuner to fine tune the parameters. The R, L, C values extracted from the circuit model are $R=310 \Omega$, $C= 0.113 \text{ pF}$, $L = 0.136 \text{ nH}$.

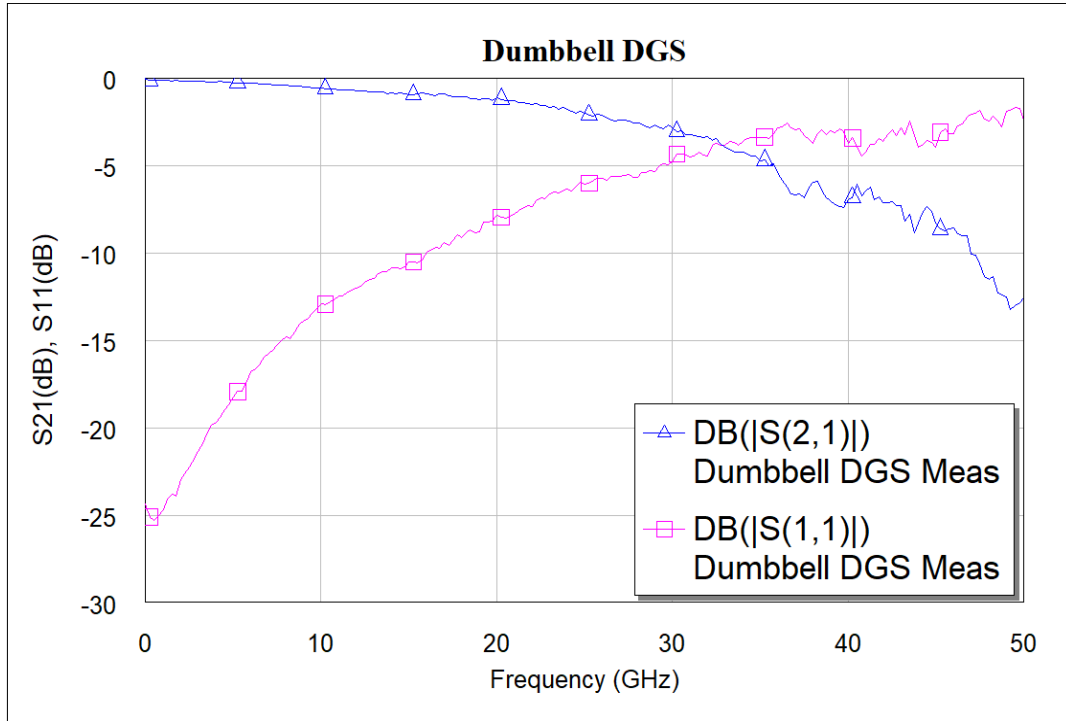


Fig.5.10 Measured frequency response of dumbbell DGS

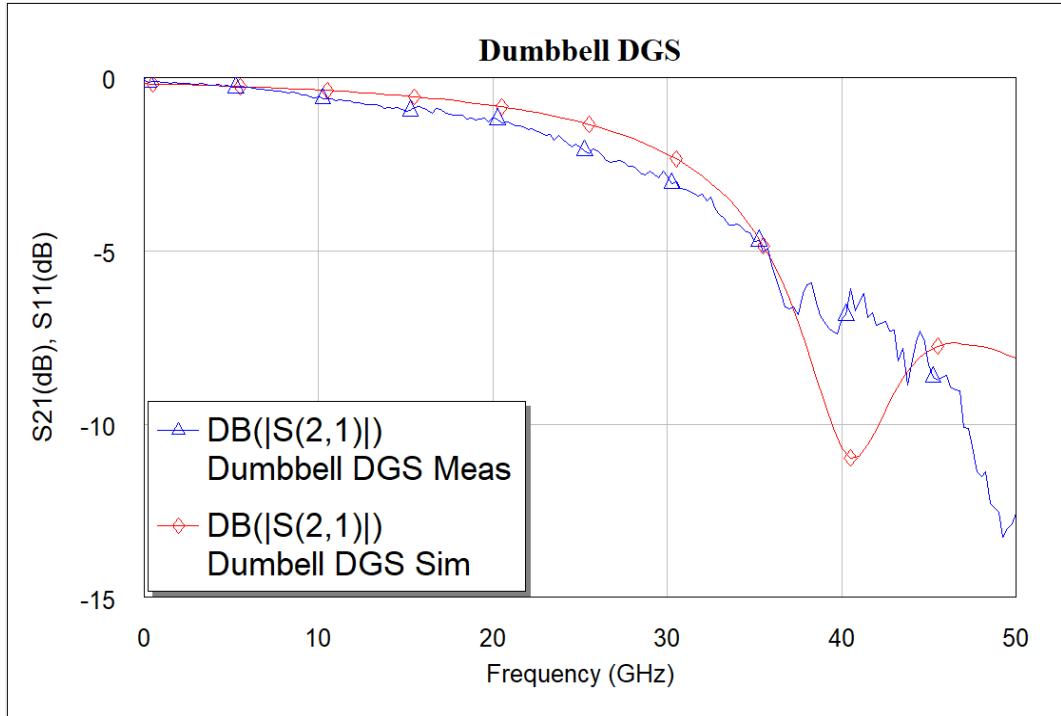


Fig.5.11 Simulated vs. measured S_{21} frequency response of dumbbell DGS

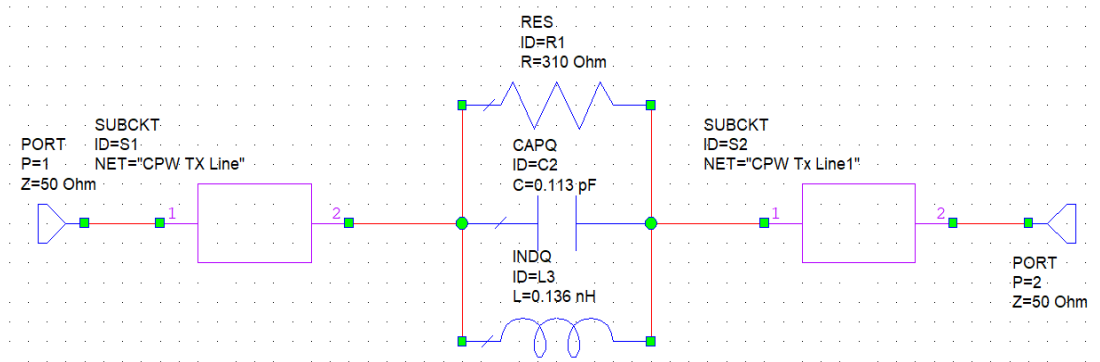


Fig.5.12 Circuit model for dumbbell DGS

5.5 U-slot DGS using CPW

U-slot DGS on CPW line is shown in fig.5.13. unlike in microstrip line the u-slot defect is not made right under the signal line but is still in the ground plane. The dimensions of the u-slot used here are width g is $10\ \mu\text{m}$, width c is $10\ \mu\text{m}$, Length L is $402.5\ \mu\text{m}$ and the distance d is $45\ \mu\text{m}$ ($22.5\ \mu\text{m} + 22.5\ \mu\text{m}$). The frequency response is shown in fig.5.14.

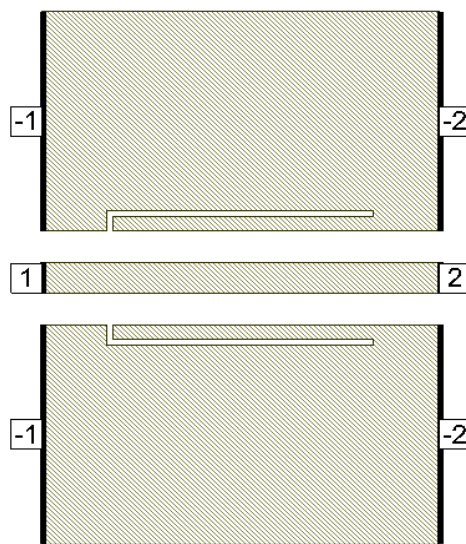


Fig.5.13 U-slot DGS on CPW

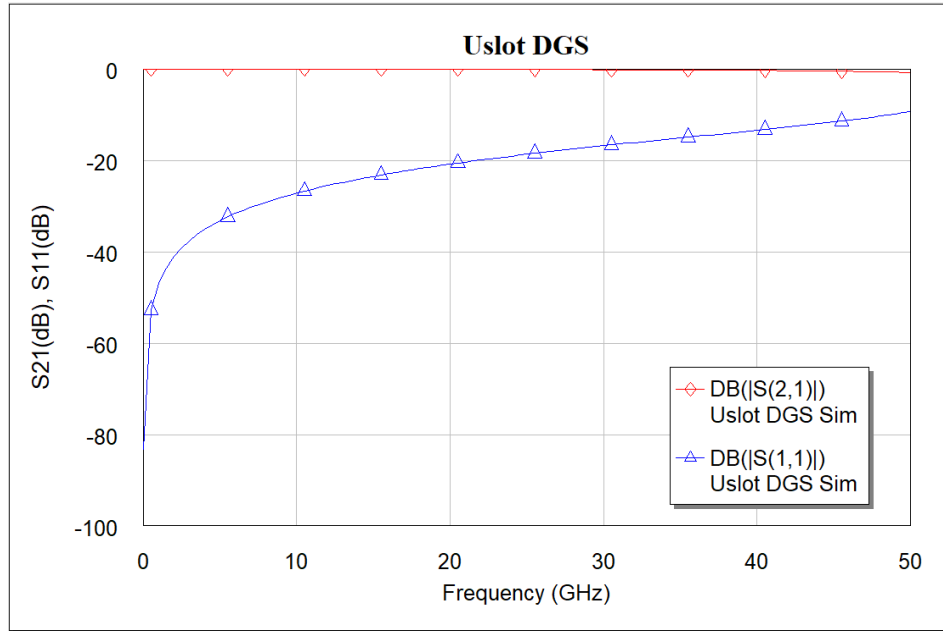


Fig.5.14 Simulated frequency response of u-slot DGS

Clearly u-slot defect doesn't generate enough capacitance and inductance for the filter to resonate in the frequency of interest. Fig.5.15 shows the measured data and fig.5.16 shows simulated vs. measured data.

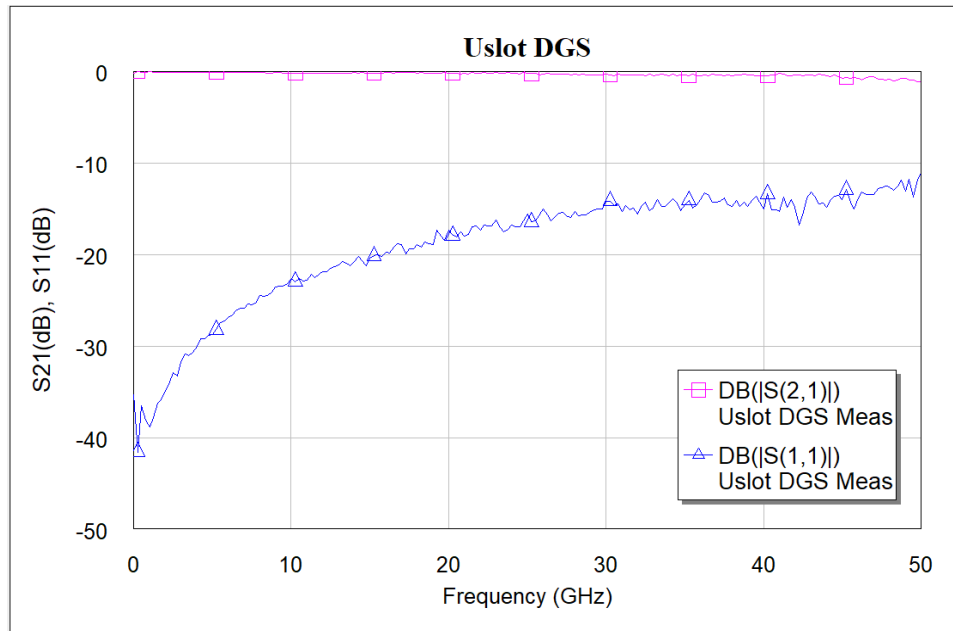


Fig.5.15 Measured frequency response of u-slot DGS

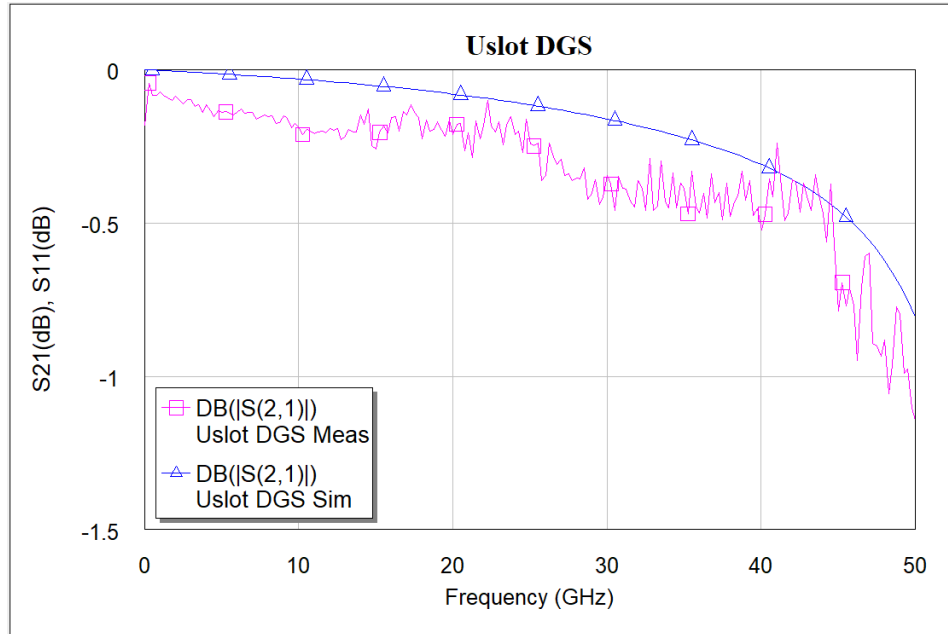


Fig.5.16 Simulated vs. measured S_{21} frequency response of u-slot DGS

From the fig.5.11 and fig.5.16 we can clearly see that the resonance frequency of these standalone DGS is outside of our frequency of interest. Lower resonance frequency is achieved by increasing capacitor and inductor which in turn increases the size of the device. However, by integration of these two devices increases the overall capacitance and inductance of the device and lower resonance frequency is achieved. Circuit model for u-slot DGS is shown in fig.5.17. The extracted values are $R= 310 \Omega$, $C= 0.01 \text{ pF}$, and $L= 0.121 \text{ nH}$.

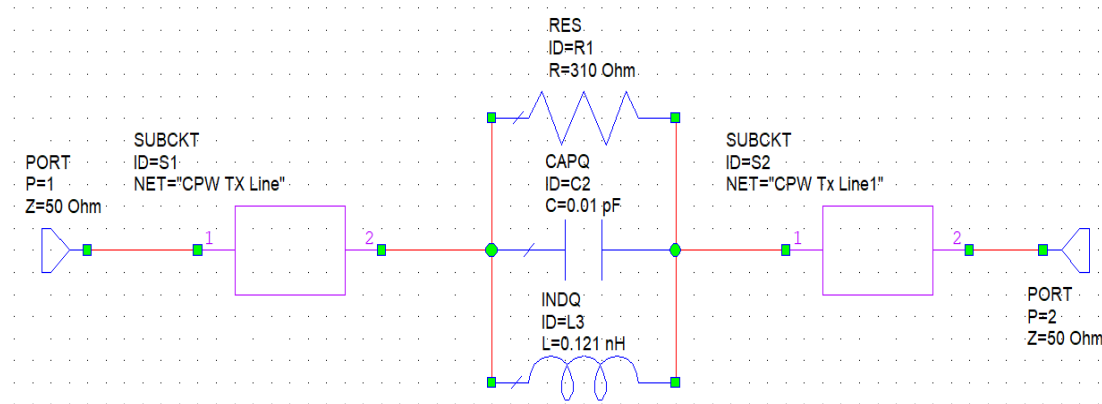


Fig.5.17 Circuit model for u-slot DGS

5.6 Dumbbell U-slot DGS

In this design the dumbbell and u-slot DGS are integrated. U-slot has more capacitance as the thin slot forms a capacitor and the dumbbell shape has more inductance with less capacitance. By integrating both we can achieve more capacitance and inductance with same size defects. This improves the filter performance and lower resonance frequency is achieved. Fig.5.18 shows the dumbbell u-slot DGS using CPW line, the dimensions are same as dumbbell DGS and u-slot DGS as in fig.5.8 and fig.5.13. The simulated frequency response is shown in fig.5.19., and measurements are shown in fig.5.20. while fig.5.21 shows and comparison of simulation vs measurements. Circuit model is shown in fig.5.22.

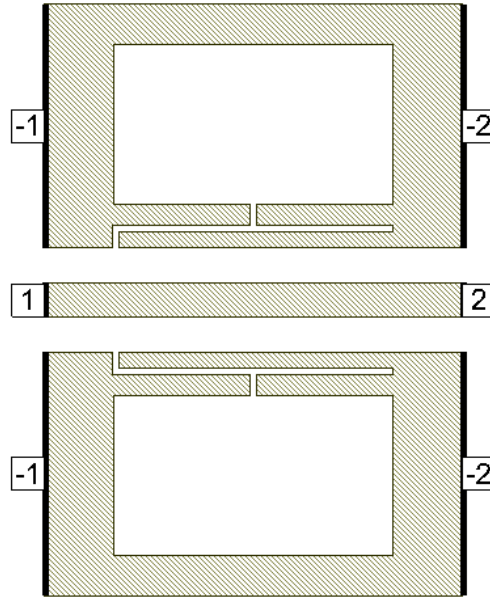


Fig.5.18 Dumbbell u-slot DGS

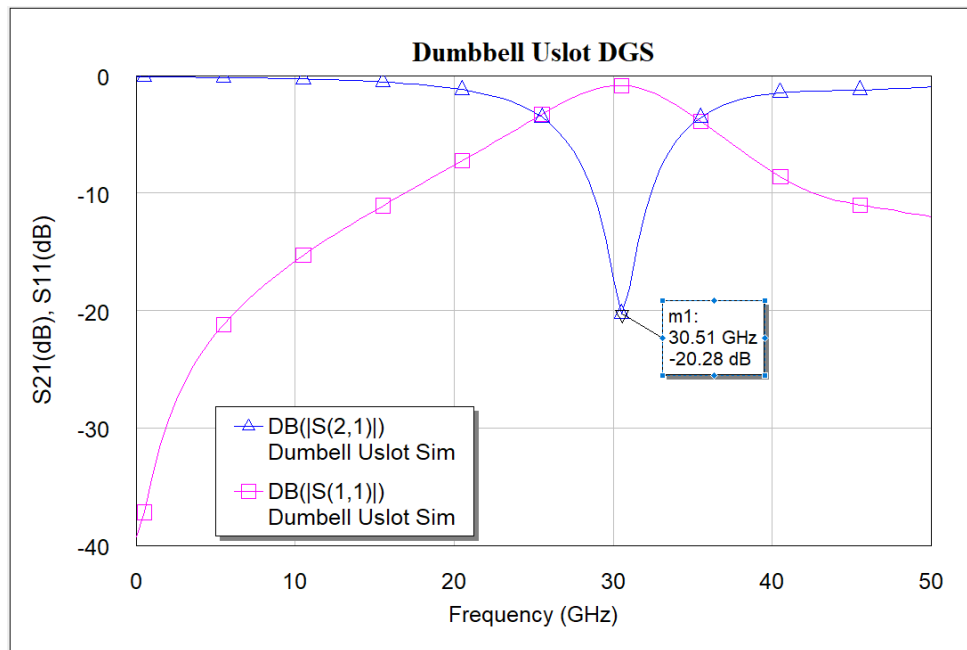


Fig.5.19 Simulated frequency response of dumbbell u-slot DGS

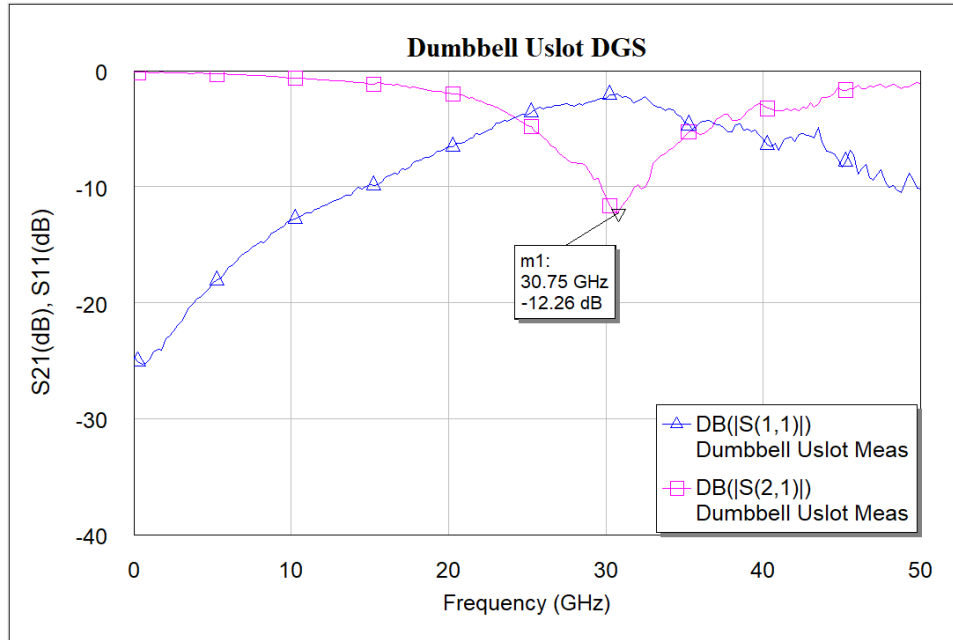


Fig.5.20 Measured frequency response of dumbbell u-slot DGS

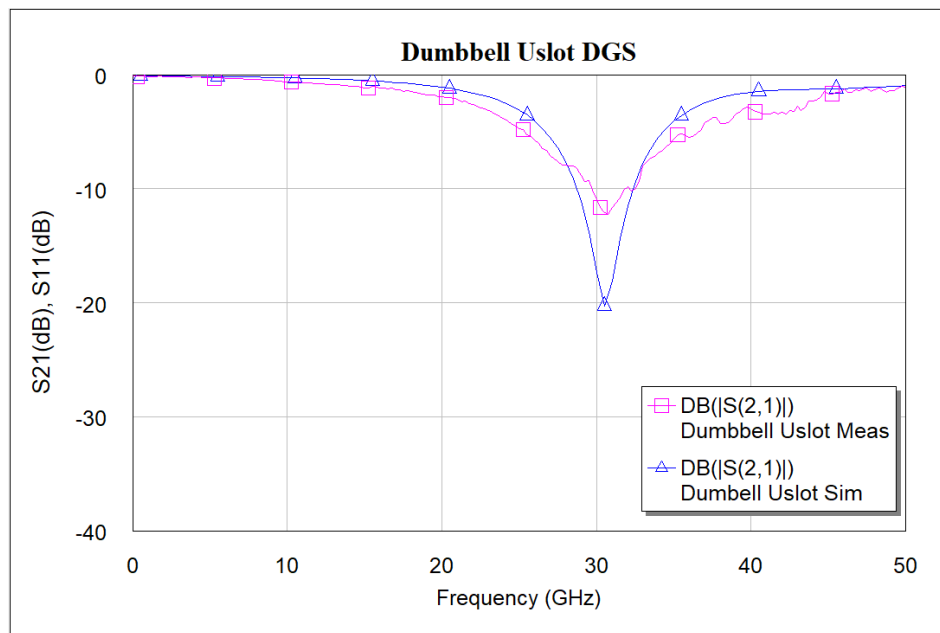


Fig.5.21 Simulated vs. measured S₂₁ frequency response of dumbbell u-slot DGS

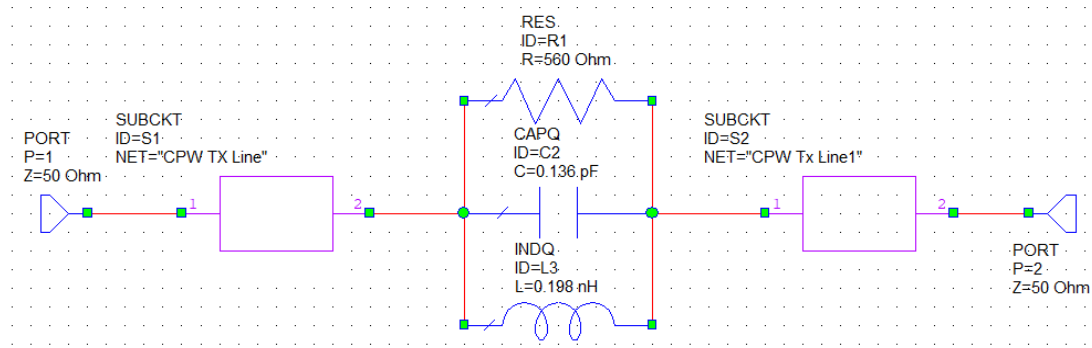


Fig.5.22 Circuit model for dumbbell u-slot DGS

The extracted values are $R = 560 \Omega$, $C = 0.136 \text{ pF}$, $L = 0.198 \text{ nH}$. Clearly from fig.5.21., we can see that the rejection is low. Deeper rejection and narrow stopband are the ideal requirements of a band stop filter. In the next section a narrow band filter with deeper rejection is demonstrated.

5.7 Dumbbell U-slot DGS Cascade

Deeper rejection is achieved by cascading multiple units of a standalone filter. In this section a cascade of two dumbbell u-slot DGS filters is demonstrated. Fig.5.23 shows the filter layout. Same dimensions as shown in fig.5.18 are used, both the unit cells must be of same dimensions. Any change in the dimensions cause changes in the capacitance and inductance values which in turn yield two resonance frequencies. Variations in the film thickness can also yield two resonances in the frequency response. When the capacitance and inductance of both single units are same a single resonance with deeper rejection and narrow bandwidth is observed from simulations as shown in fig.5.24. and measured results are shown in fig.5.25. while fig.5.26 shows comparison of simulation vs measurements.

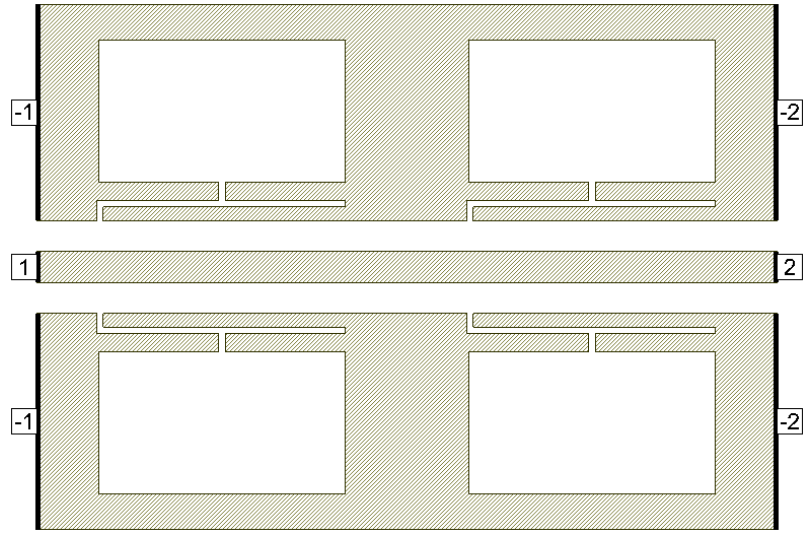


Fig.5.23 Dumbbell u-slot DGS cascade

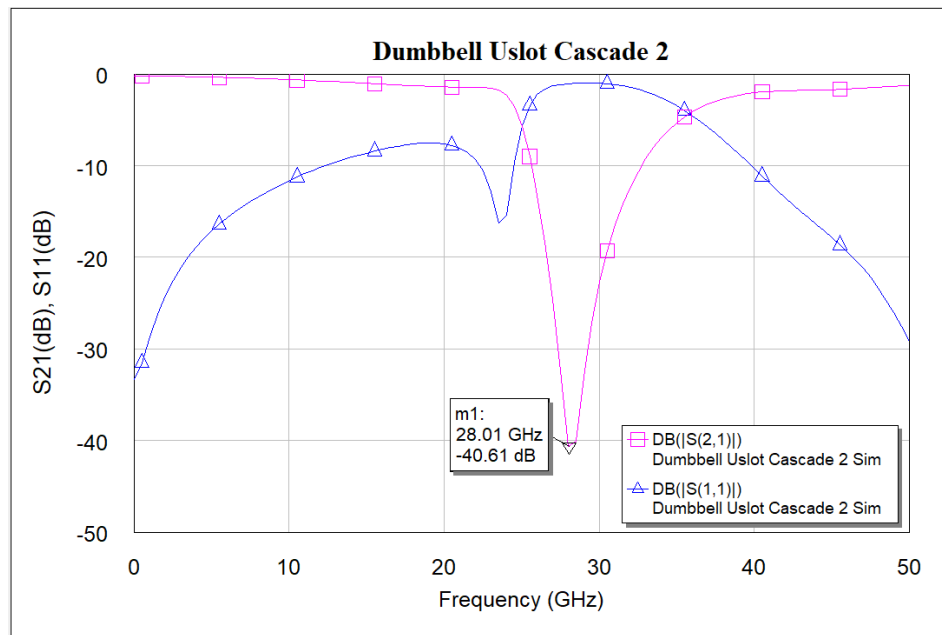


Fig.5.24 Simulated frequency response of dumbbell u-slot cascade DGS

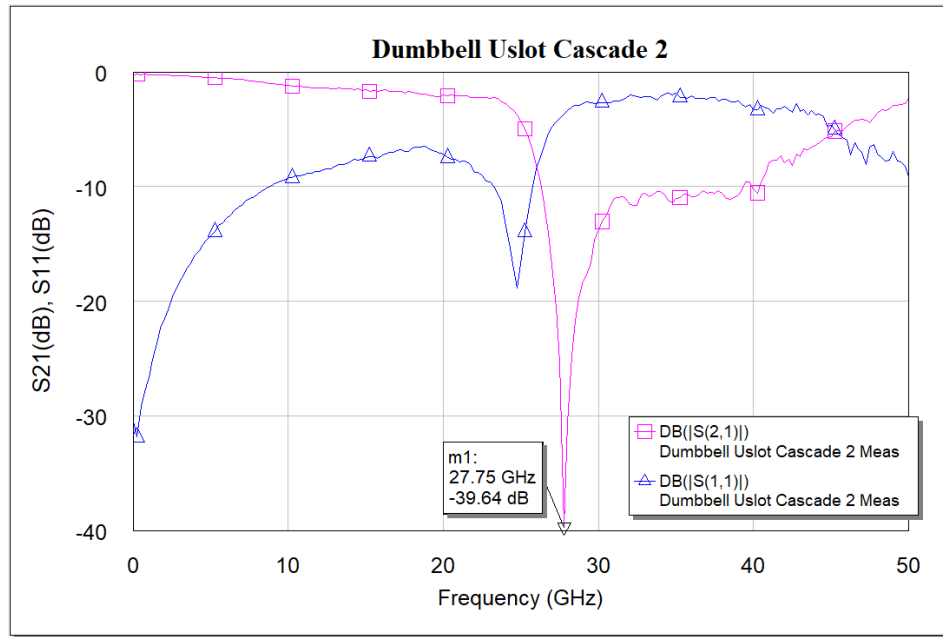


Fig.5.25 Measured frequency response of dumbbell u-slot cascade DGS

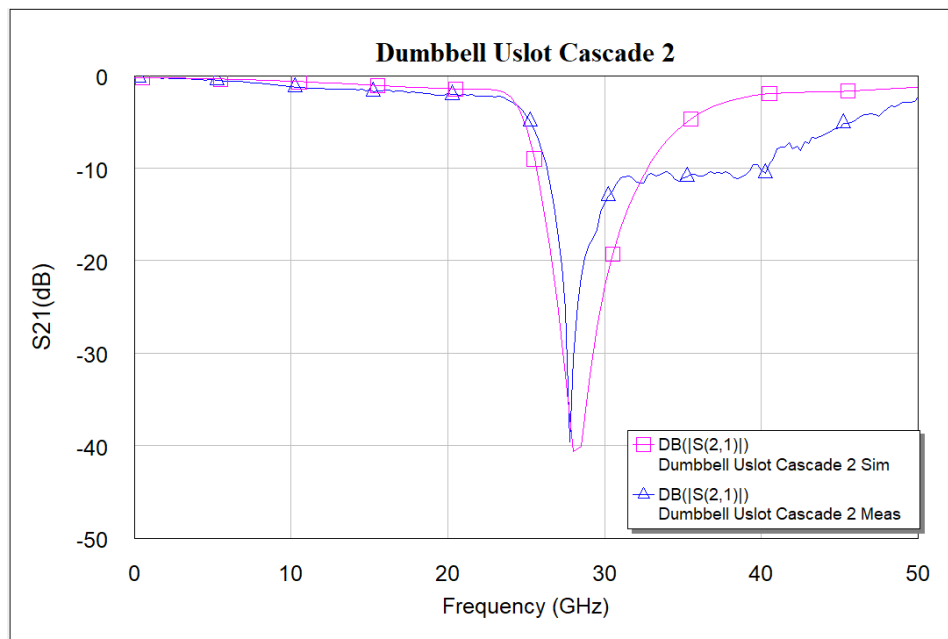


Fig.5.26 Simulated vs. measured S_{21} frequency response of dumbbell u-slot cascade DGS

The slight shift in the resonance frequency as well as the narrow bandwidth from the measurements is due to the combination of de-embedding errors and

CPW signal line coupling to the ground. For longer devices the de-embedding errors play vital role. Moreover, the signal line to ground coupling of the CPW line also adds parasitic capacitance for bigger devices. The circuit model shown in fig.5.27 matches very well with the measured data. The values extracted from the circuit diagram are $R1 = 8650 \Omega$, $C1 = 0.233 \text{ pF}$, $L1 = 0.1382 \text{ nH}$ and $R2 = 8650 \Omega$, $C2 = 0.233 \text{ pF}$, $L2 = 0.1382 \text{ nH}$. The comparison of frequency response of circuit model vs measured data is shown in fig.5.28.

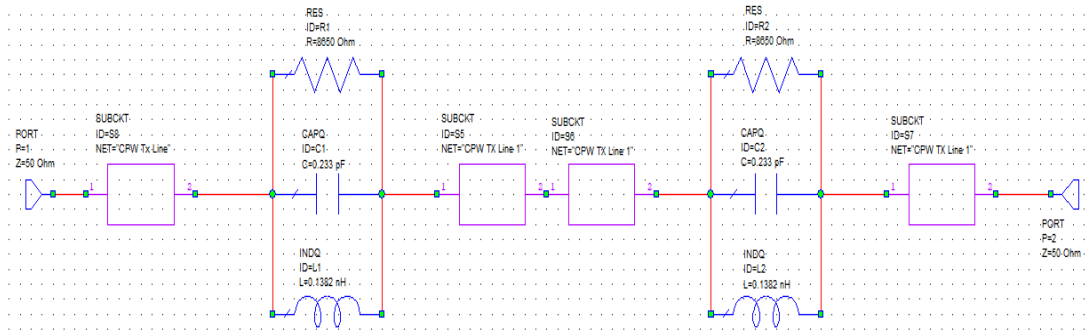


Fig.5.27 Circuit model for dumbbell u-slot cascade DGS

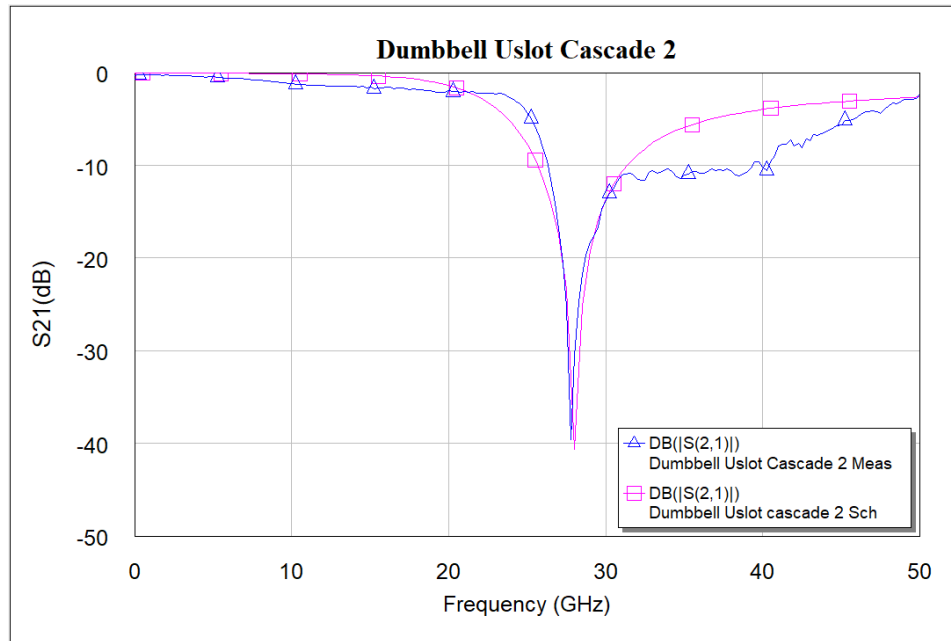


Fig.5.28 Schematic model vs. measured S_{21} frequency response of dumbbell u-slot cascade DGS

5.8 Dumbbell U-slot DGS Using BST and PCM

Achieving tuning with planar structures requires high voltages. DC biases from 0 V – 21 V were applied but no tuning was observed. This is mainly because the smaller slot dimension in the device is 10 μm and the overall area of this slot compared to device size is very small. Typically, 40 kV/cm is required to tune the devices. Highest tuning is achieved at 400 kV/cm. For this device, larger voltages about 40 V or higher are required to see the tuning. However, having BST thin film layer give large capacitances and inductances which makes the size of device small. Tuning can be achieved by adding a phase change material layer in the device as shown in the fig.5.29.

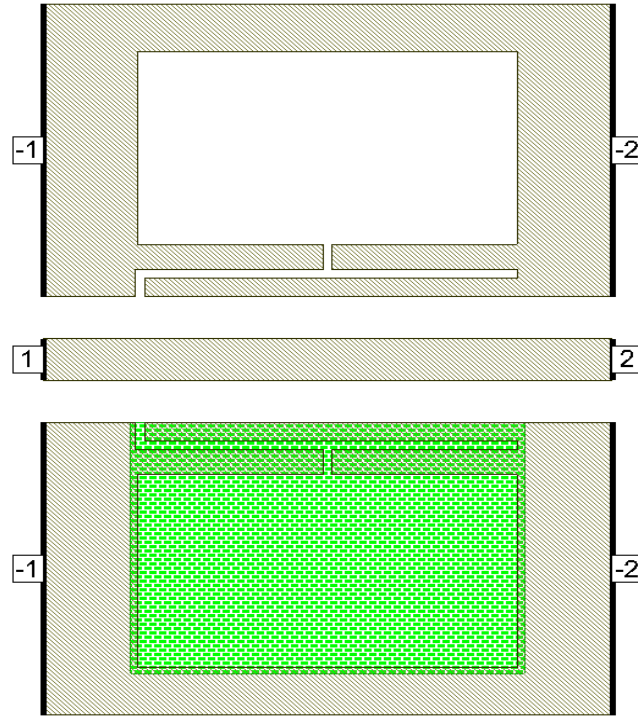
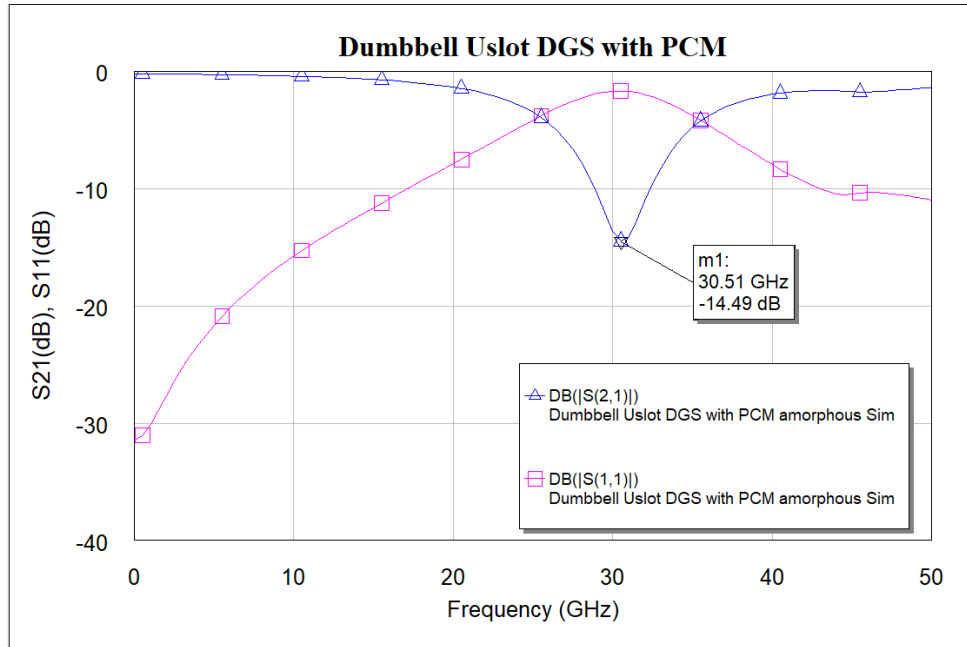
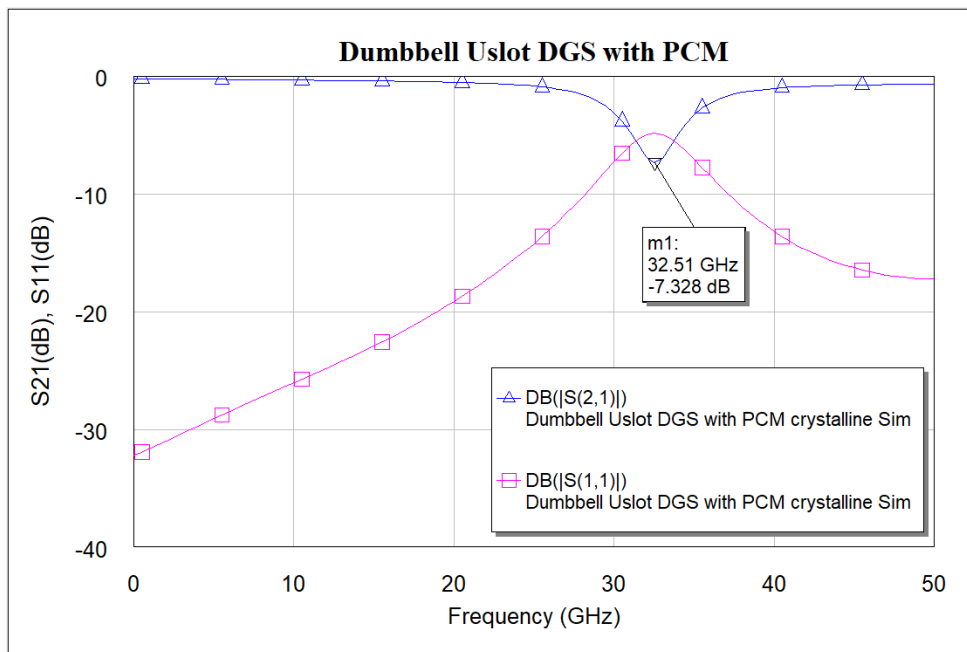


Fig.5.29 Dumbbell u-slot DGS with PCM

Adding the phase change material will give us additional tuning. When the PCM material is in amorphous state, the device has inductance and capacitance from the defects in both the ground planes, but when the PCM material is in crystalline state only inductance and capacitance from defects in one ground plane is seen as the defects in the other ground plane would be covered with metal. This reduction in the inductance and capacitance will push the resonance to higher frequency. This can be used for tuning the filter. Fig.5.30 shows the frequency response of dumbbell u-slot DGS in both amorphous and crystalline state.



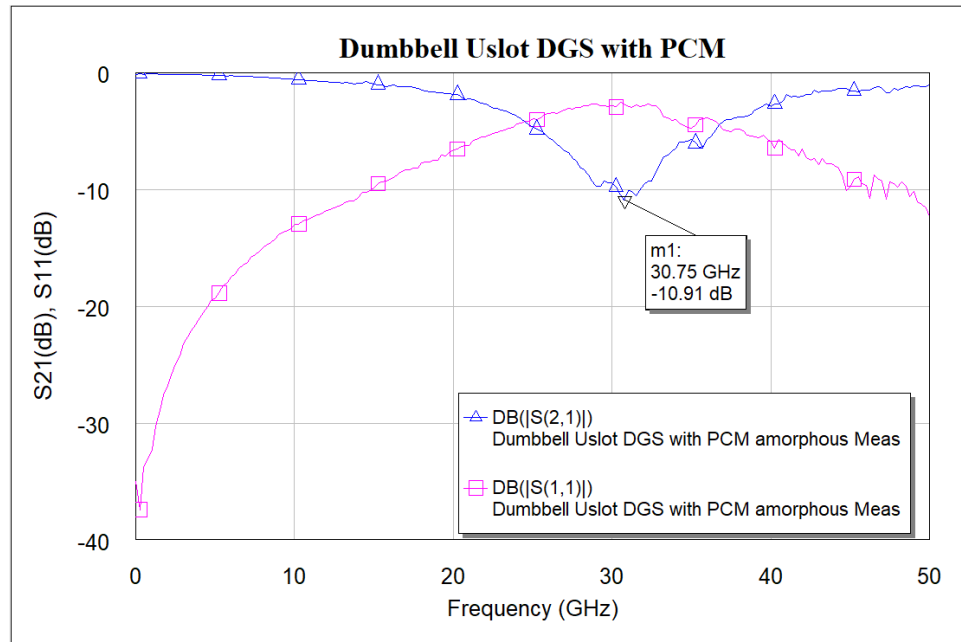
(a)



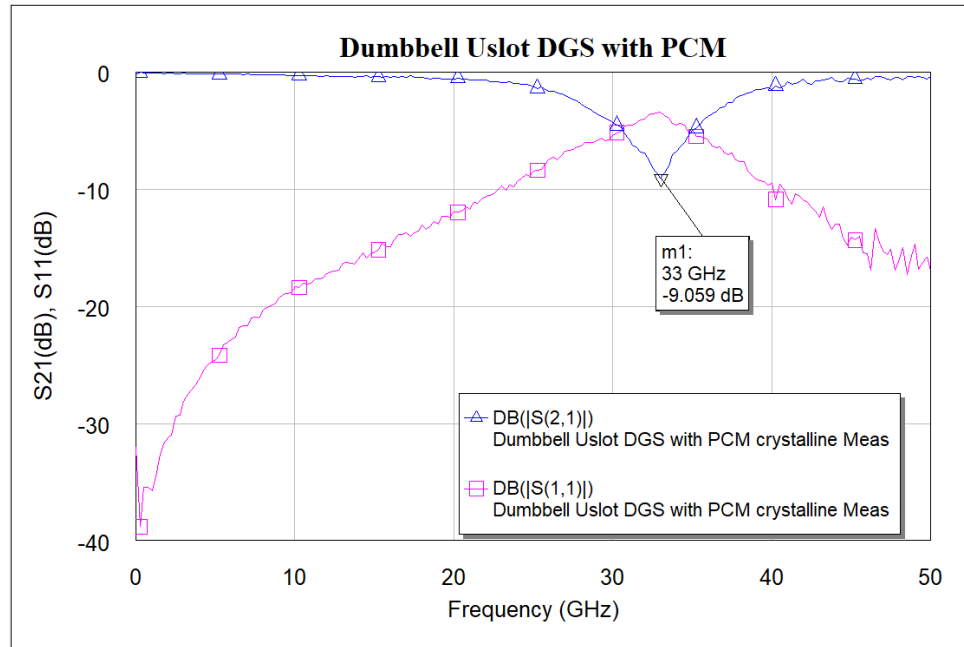
(b)

Fig.5.30 Simulated frequency response of dumbbell u-slot DGS with PCM (a) amorphous PCM (b) crystalline PCM

The frequency response in amorphous state is like that of the dumbbell u-slot DGS as the PCM is in amorphous state the device has inductance and capacitance from the defects in both the ground planes. But whereas from the frequency response in crystalline state, the resonance frequency has shifted to higher frequency as expected. Fig.5.31. shows the measured results.



(a)

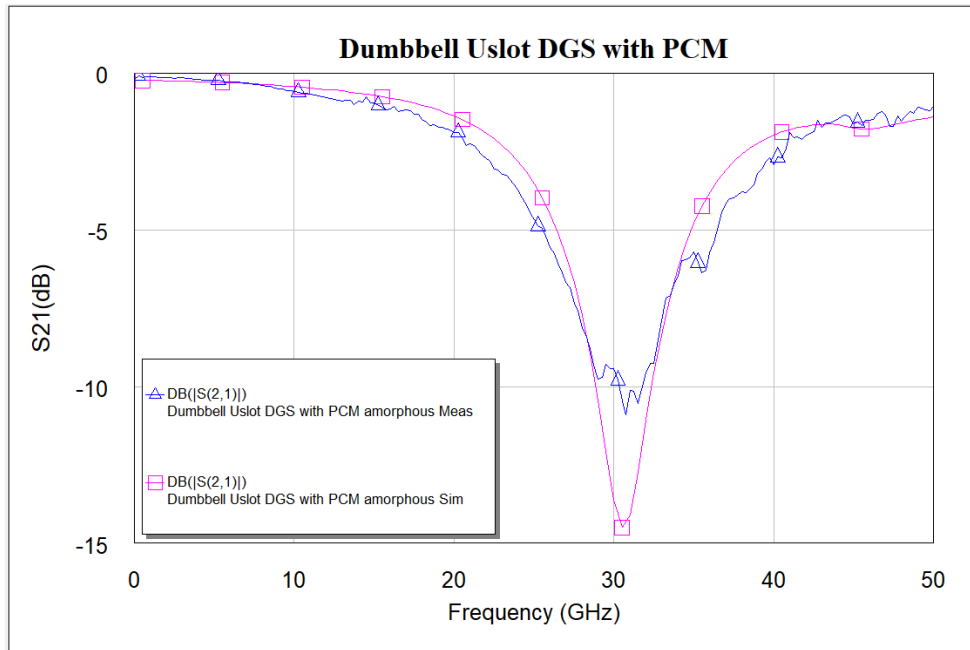


(b)

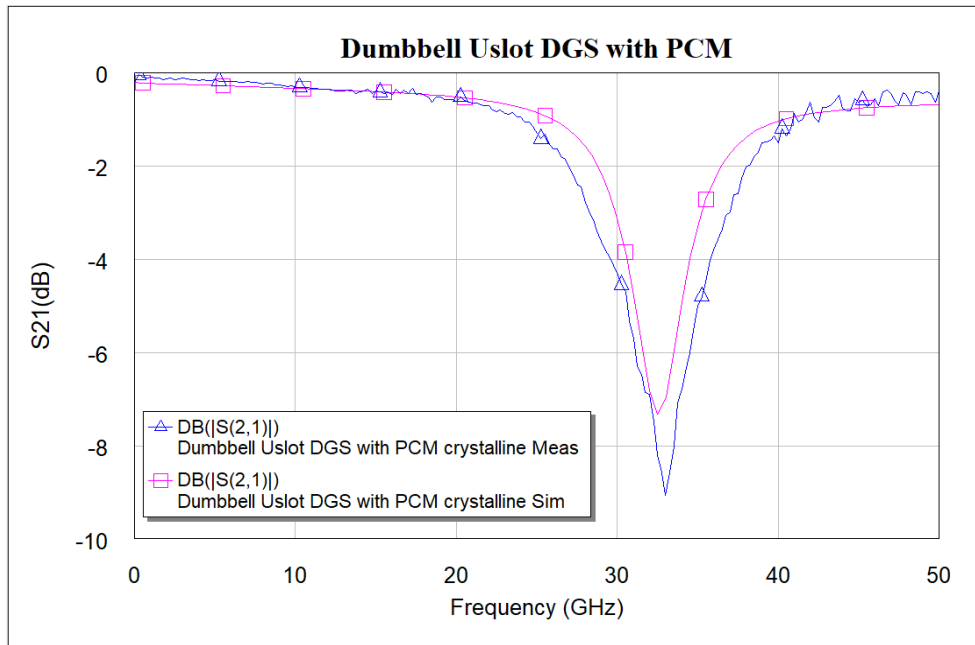
**Fig.5.31 Measured frequency response of dumbbell u-slot DGS with PCM
(a) amorphous PCM (b) crystalline PCM**

From the fig.5.31., (a) and (b) we can clearly see a shift in resonance frequency from 30.75 GHz to 33 GHz. A frequency shift of about 2.25 GHz is achieved i.e., 7.32% of tuning is achieved by using the PCM. Fig.5.32 shows the comparison of simulated and measured results. And the circuit model used is shown in fig.5.33. which is like that shown in previous sections. The parameters extracted are $R = 430 \Omega$, $C = 0.159 \text{ pF}$, $L = 0.171 \text{ nH}$ for amorphous state and $R = 430 \Omega$, $C = 0.315 \text{ pF}$, $L = 0.075 \text{ nH}$ in crystalline state. The increase in capacitance in crystalline state make sense as a big piece of metal PCM in crystalline state forms a large parasitic capacitance to substrate. The as deposited film is in amorphous state, which is high resistance state. To make it crystalline, the sample is heated on the hot plate at 240 °C for about 5 minutes. The

germanium telluride thin film transforms from amorphous to crystalline state. After the sample is cooled down, the measurements are again performed on the same device to see change in the frequency response.



(a)



(b)

Fig.5.32 Simulated vs. measured S_{21} frequency response of dumbbell u-slot DGS with PCM (a) amorphous PCM (b) crystalline PCM

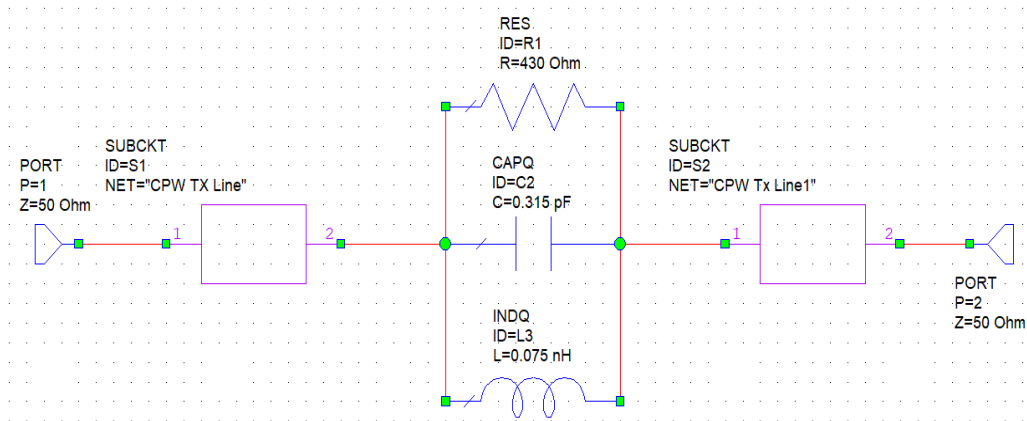


Fig.5.33 Circuit model for dumbbell u-slot DGS with PCM

The significance of use of PCM can be seen when two single DGS filters are cascaded as shown in the previous section.

5.9 Dumbbell U-slot DGS Using BST and PCM Cascade

Like section 5.7, two single DGS cells with PCM are cascaded as shown in fig.5.34.

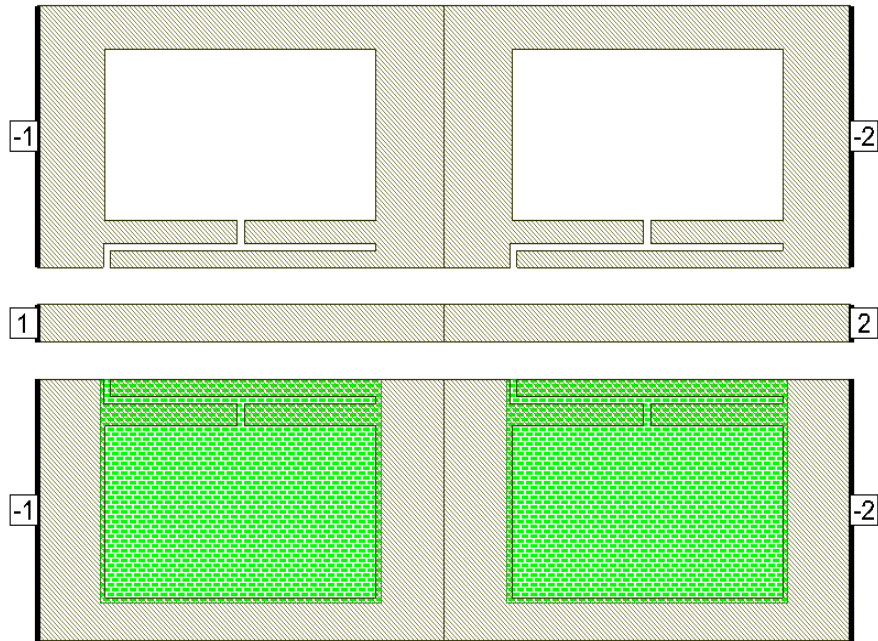
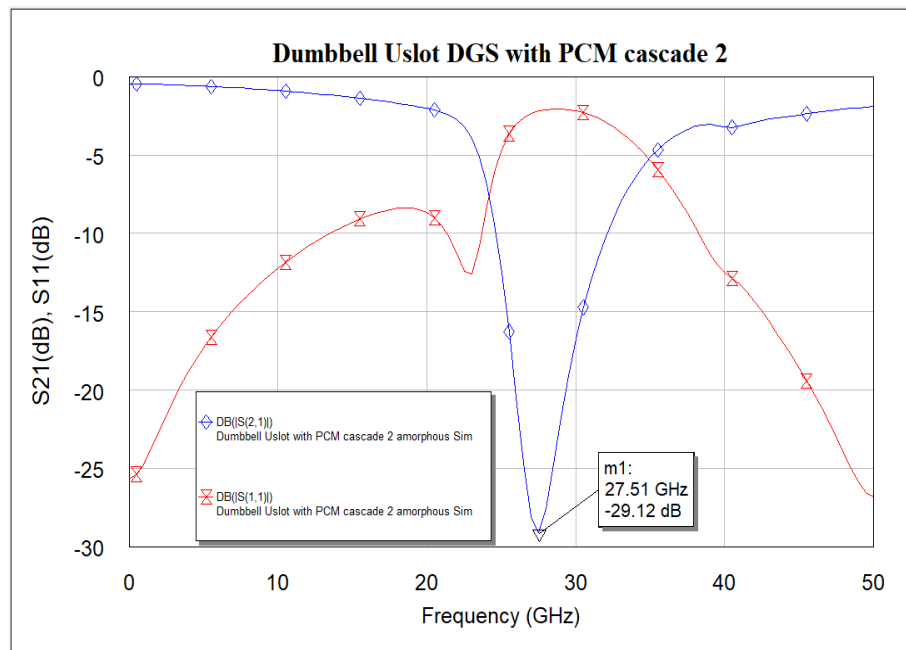
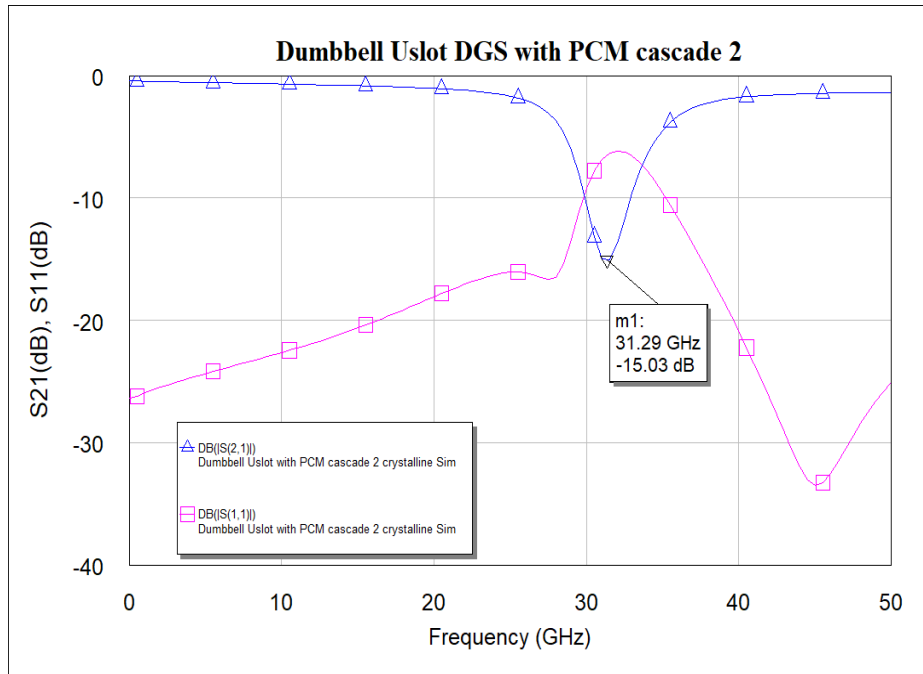


Fig.5.34 Dumbbell u-slot DGS with PCM Cascade

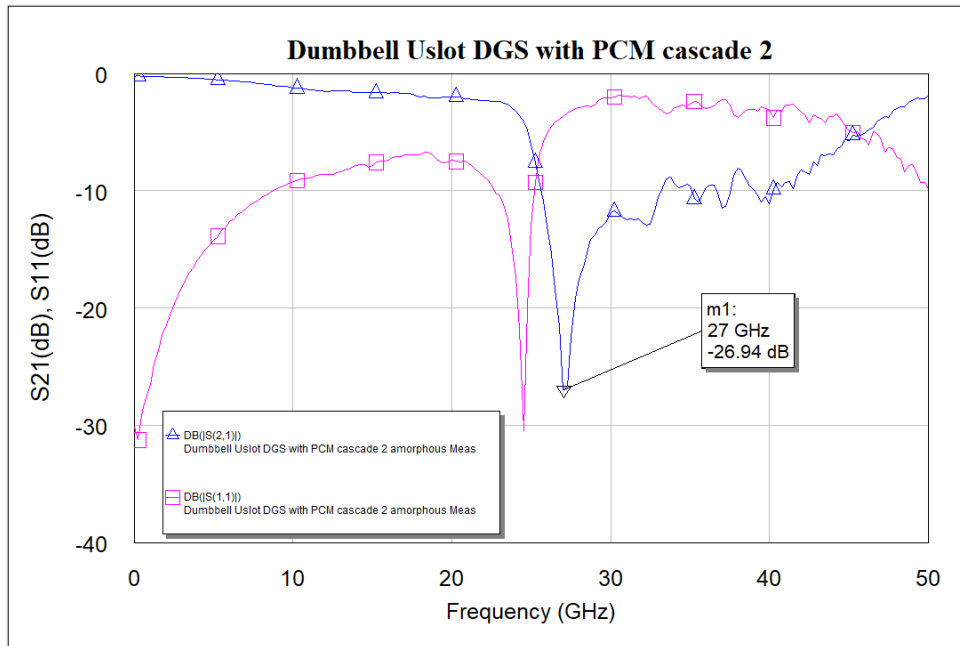


(a)

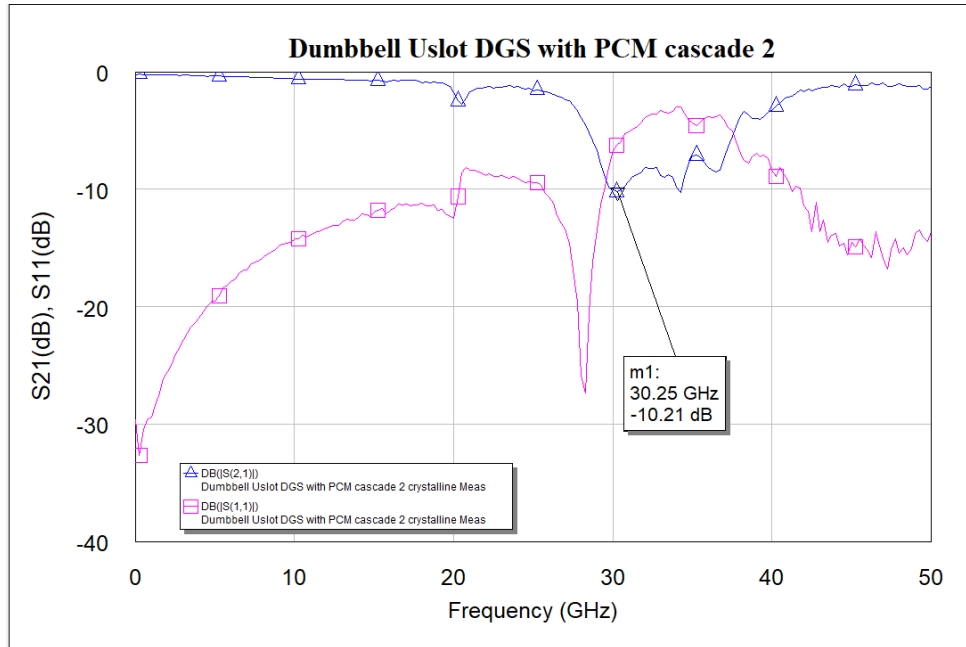


(b)

Fig.5.35 Simulated frequency response of dumbbell u-slot DGS with PCM cascade (a) amorphous PCM (b) crystalline PCM

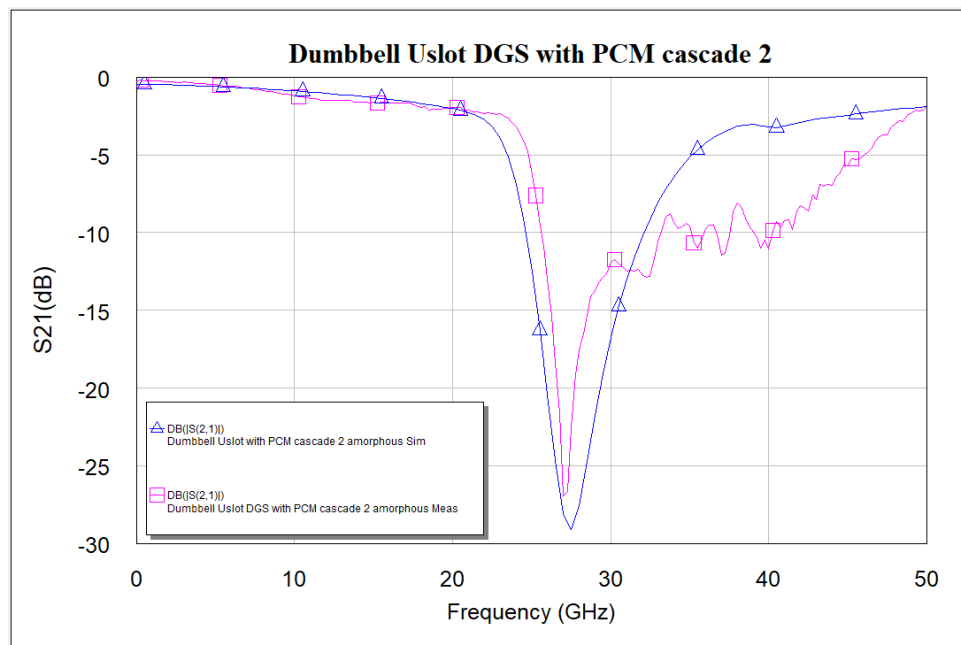


(a)

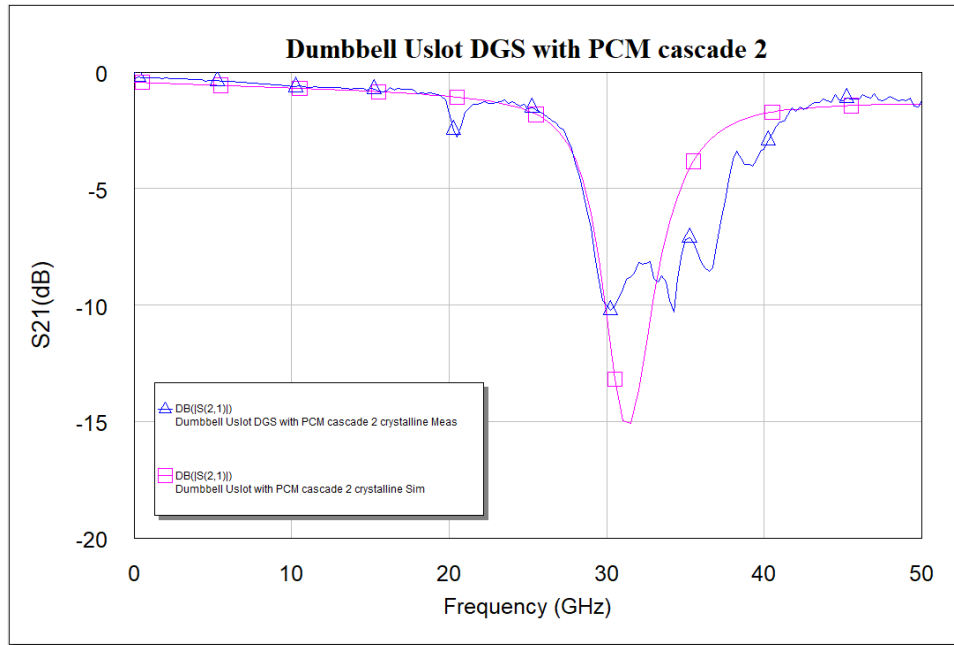


(b)

Fig.5.36 Measured frequency response of dumbbell u-slot DGS with PCM cascade (a) amorphous PCM (b) crystalline PCM



(a)



(b)

Fig.5.37 Simulated vs. measured S_{21} frequency response of dumbbell u-slot DGS with PCM cascade (a) amorphous PCM (b) crystalline PCM

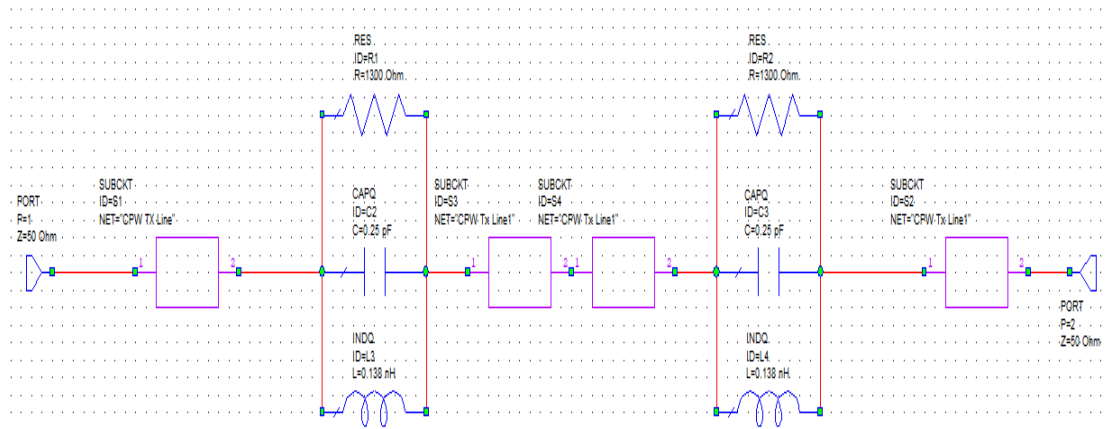


Fig.5.38 Circuit model for dumbbell u-slot DGS with PCM Cascade

From the simulated frequency response shown in fig.5.35 and fig.5.36, little more than 3 GHz tuning is achieved. From the measured data shown in fig.5.36 (a) and (b) a shift in resonance frequency from 27 GHz to 30.25 GHz. A frequency

shift of about 3.25 GHz is achieved i.e., 12.04% of tuning is achieved by using the PCM. From fig.5.37 we can see that the simulation results align very well with the measured results. The circuit model shown in fig.5.38 is used to extract the lumped component values. The values are $R1 = 1300 \Omega$, $C1 = 0.25 \text{ pF}$, $L1 = 0.138 \text{ nH}$ and $R2 = 1300 \Omega$, $C2 = 0.25 \text{ pF}$, $L2 = 0.138 \text{ nH}$.

In this chapter, tunable defected ground structures have been demonstrated successfully. Adding phase change material layer to the devices have increased the tuning. About 7.32% tuning is achieved for dumbbell u-slot devices with PCM and the tuning range have been increased to 12.04% by cascading the DGS.

SUMMARY AND CONCLUSIONS

In this work, advantages of integrating phase change materials such as Germanium Telluride with BST thin films have been demonstrated successfully. GeTe based RF switch with low insertion loss of 0.23 dB and high isolation -of 19.75 dB at 15 GHz was demonstrated.

Modified Metal-Insulator-Metal (MIM) varactor designs are implemented by integrating BST and GeTe materials for higher tuning, low losses, and low control voltages with reduced size for high frequency applications. Increased tunability of 6.3:1 which is about 57% more compared to 4:1 tuning achieved from a traditional varactor.

Phase shifters using modified varactors for low losses and high Figure of Merit (FOM) at high frequency applications are demonstrated. A phase shifter device that can provide 360° phase shift over a broad mm-Wave frequency range (24 GHz – 50 GHz) have been experimentally demonstrated. With good FOM of 46.64 degrees/dB at 50 GHz and 19.07 degrees/dB at 24 GHz using MIM varactors with BST and GeTe thin films and 319° phase shift at 24 GHz with FOM 12.8 degrees/dB and more than 360° phase shift at 50 GHz with $FOM_{(2V-10V)} > 21.5$ degrees/dB using MIM varactor with only BST thin films.

Tunable band stop DGS filters are demonstrated with CPW transmission line configuration on the top of BST thin film. Cascaded two-unit cells enhanced the band-rejection behavior with a notch depth of -39.64 dB @ 27.75 GHz. By integrating the DGS with GeTe a tunable stop band characteristics is

demonstrated. A shift in resonance from 30.75 GHz to 33 GHz is seen, a frequency shift of 2.25GHz, i.e., 7.32 % tuning is achieved. A frequency shift of about 3.25 GHz is seen i.e., 12.04% of tuning is achieved by cascading of two-unit cells.

In conclusion, Integration of Barium Strontium Titanate (BST) thin films with Germanium Telluride (GeTe) thin films have been successfully demonstrated. Integrating both the thin films increases tunability of the devices and creates a new scope in design of reconfigurable rf/microwave circuits.

FUTURE WORK

Phase change materials such as germanium telluride once crystallized stays crystallized. Re-amorphization of GeTe is difficult, especially when integrated in a system with other electronics. This needs to investigate further, utilizing different optical sources as well as electrical bias. Integrating Vanadium Dioxide (VO_2) thin films with BST would overcome the complications of the re-amorphization of GeTe. VO_2 as deposited thin films are amorphous i.e., in high resistance state. The resistance decreases with increase in temperature like GeTe. However, the phase transition temperature for VO_2 thin films is about 68°C , much lower than GeTe and unlike GeTe, VO_2 changes to an insulator with decreasing in temperature as shown in fig.6.1.

Overcoming the high temperature deposition of VO_2 would be a major challenge. As both VO_2 and BST thin films need high temperature depositions and wouldn't sustain high temperatures after deposited. New fabrication techniques to thermally insulating BST and VO_2 materials needs to be explored. Using other high k dielectric materials that require low thermal budget instead of BST could be a possible solution.

REFERENCES

- [1] D. Schnauffer, T. Nguyen, B. Thomas, A. Mariani, P. Cooper, B. Peterson, P.Warder., "5G RF for Dummies", 2nd Qorvo Special Edition., John Wiley & Sons, Inc. 2020.
- [2] S.Juneja., R.Pratap., R.Sharma., "Semiconductor Technologies for 5G Implementation at Millimeter Wave Frequencies – Design Challenges and Current State of Work," Engineering Science and Technology., Vol.24., pp.no. 205-217., June 2020.
- [3] G.M.Rebeiz., G.L.Tan., and J.S.Hayden., " RF MemS Phase Shifters: Design and Applications," IEEE Microwave Magazine., pp.no. 72-81., June 2002.
- [4] A.S. Nagra., J.Xu., E.Erker., and R.A.York., " Monolithic GaAs Phase Shifter with Low Insertion Loss and Continuous 0-360° Phase Shift at 20 GHz," IEEE Microwave and Guided Wave Letters., Vol.9., No.1., pp.no. 31-33., January 1999.
- [5] S.Asalam., M.Khanna., V.Veenugopal., and B.K.Kuanr., " Microwave Monolithic Filter and Phase Shifter Using Magnetic Nanostructures," AIP Advances 8., 056624., pp.no. 1-6., December 2017.
- [6] Z.Wang., Y.Y.Song., Y.Sun., J.Bevivino., M.Wu., V.Veerakumar., T.J.Fal., and R.E.Camley., " Millimeter Wave Phase Shifter Based on Ferromagnetic Resonance in a Hexagonal Barium Ferrite Thin Film," Appl. Phys.Lett. 97., 072509., pp.no. 1-3., August 2010.

- [7] J.Douglas., L.E.Davis., G.F.Dionne., E.F.Schloemann., and S.N.Stitzer., “ Ferrite Devices and Materials,” IEEE Trans. on Micro. Th. And Tech., Vol 50., No.3., pp.no. 721-737., March 2002.
- [8] E.G.Erker., A.S.Nagra., Y.Liu., P.Periaswamy., T.R.Taylor., J.Speck., and R.A.York., “Monolithic Ka-Band Phase Shifter Using Voltage Tunable BaSrTiO₃ Parallel Plate Capacitors,” IEEE Microwave and Guided Wave Letters., Vol.10., No.1., pp.no. 10-12., January 2000.
- [9] K.Vijay., K.A.Jose., V.V.Varadan., R.hughes., and J.F.Kelly.,” A Novel Microwave Planar Phase Shifter,” Microwave Journal., pp.no. 244-254., April 1995.
- [10] F. De Flaviis, N. G. Alexopoulos, and O. M. Stafsudd, “Planar Microwave Integrated Phase Shifter Design with High Purity Ferroelectric Material,” IEEE Trans. Microwave Theory Tech., Vol. 45, pp.no. 963–969, June 1997.
- [11] F. W. Van Keuls, R. R. Romanovsky, N. D. Varaljay, F. A. Miranda, C.L. Canedy, S. Aggarwal, T.Venkatesan, and R. Ramesh, “A Ku-Band Gold/ Ba_xSr_{1-x}TiO₃/LaAlO₃ Conductor/Thin-Film Ferroelectric Microstrip Line Phase Shifter for Room Temperature Communications Applications,” Microwave Opt. Technol. Lett., Vol. 20, No. 1, pp.no. 53–56, January. 1999.
- [12] F. W. Van Keuls, C. H. Mueller, F. A. Miranda, R. R. Romanovsky, C. L. Canedy, S. Aggarwal, T. Venkatesan, R. Ramesh, J. S. Horwitz, W. Chang, and W. Kim, “Room Temperature Thin Film Ba_xSr_{1-x}TiO₃ Ku-Band Coupled Microstrip Phase Shifters: Effects of Film Thickness, Doping, Annealing and Substrate Choice,” in IEEE MTT-S Dig., 1999.

- [13] B. Underdahl., "5G for Dummies, Sprint Business Special Ed.", John Wiley & Sons, Inc. 2018.
- [14] K.Muhonen., S.Parker., K.Annam., "Parasitic Model to Describe Breakdown in Stacked- FET SOI Switches," IEEE RFIC Sym., pp.no. 139-142., 2020.
- [15] M.Z.Koohi., A.Mortazawi., "Reconfigurable Radios Employing Ferroelectrics," IEEE Microwave Mag., pp.no. 120-135., May. 2020.
- [16] K. Pan, W. Wang, E. Shin, K. Freeman, and G. Subramanyam, "Vanadium oxide thin-film variable resistor-based RF switches," IEEE Transactions on Electron Devices, Vol. 62, No. 9, pp.no. 2959-2965, Sep. 2015.
- [17] E. Shin, K. C. Pan, W. Wang, G. Subramanyam, V. Vasilyev, K. Leedy, and T. Quach, "Tungsten-doped vanadium dioxide thin film based tunable antenna," Materials Research Bulletin, Vol. 101, pp.no. 287–290, Feb. 2018.
- [18] L. Li, W. Wang, E. Shin, T. Quach, and G. Subramanyam, "Design of tunable shunt and series interdigital capacitors based on vanadium dioxide thin film," Proceedings of the IEEE National Aerospace and Electronics Conference, NAECON 2017, pp.no. 279-283, 2017.
- [19] K. Pan, E. Shin, K. Freeman, W. Wang, D. Brown, and G. Subramanyam, "Vanadium dioxide thin film series single-pole single throw switch," Proceedings of the IEEE National Aerospace and Electronics Conference, NAECON 2014, pp.no. 1-4, 2014.
- [20] H. Yue, D. Brown, G. Subramanyam, K. Leedy, and C. Cerny, "Thin film Barium-Strontium-Titanate Parallel-Plate varactors integrated on low-resistivity silicon and sapphire substrate," 2013 Joint IEEE International Symposium on

Applications of Ferroelectric and Workshop on Piezoresponse Force Microscopy (ISAF/PFM), pp.no. 291–294, Feb. 2014.

[21] G. Subramanyam, E. Shin, D. Brown, and H. Yue, “Thermally controlled vanadium dioxide thin film microwave devices,” Proceedings of the IEEE Midwest Symposium on Circuits and Systems (MWSCAS), pp.no. 73-76, 2013.

[22] S. Wang, W. Wang, E. Shin, T. Quach and G. Subramanyam, “Tunable inductors using vanadium dioxide as the control material,” Microwave and optical technology letters, vol. 59, no. 5, pp.no. 1057-1061, May 2017.

[23] E. Shin, L. Li, W. Wang, K. Pan and G. Subramanyam, “Design and Fabrication of Tunable Inductors Based on Vanadium Dioxide Thin Film”, SPIE International Workshop on Thin film for Electronics, Eletro-Optics, Energy and Sensors,2019.

[24] F.Miranda., G.Subramanyam., F.W.V.Keuls., R.R.Romanofsky., J.D.Warner.,and Carl.H.Mueller., ”Design and development of Ferroelectric Tunable Microwave Components for Ku- and K- Band Satellite Communication Systems.” IEEE Transactions on Microwave Theo. and Tech., Vol.48., No..7, pp.no-1181-1189., July 2000.

[25] G. Subramanyam, R. Neidhard, K. Stamper and M. Calcaterra, “Improved RF Performance Characteristics of Cascaded Ferroelectric Varactor Shunt Switches,” 15th IEEE international symposium on the applications of ferroelectrics, pp.no. 352-355, 2006.

- [26] C. J. G. Meyers, C. R. Freeze, S. Stemmer and R. A. York, "Voltage-Tunable Parallel-Plate Capacitors Fabricated on Low-Loss MBE-Grown BST," IEEE/MTT-S International Microwave Symposium - IMS, pp.no. 739-742, 2018.
- [27] K.Annam., D.Spatz., E.Shin., G.Subramanyam., "Experimental verification of Microwave Phase Shifters Using Barium Strontium Titanate (BST) Varactors," IEEE National Aerospace and Electronics Conference (NAECON), pp.no. 63-66., 2019.
- [28] E.G.Erker., A.S.Nagra., Y.Liu., P.Periaswamy., T.R.Taylor., J.Speck and R.A.York., "Monolithic Ka-Band Phase Shifter using Voltage Tunable BaSrTiO₃ Parallel Plate Capacitors," IEEE Microwave and Guided Wave Lett. Vol.10, No.1, 2000.
- [29] D.Kuylenstierna., G.Subramanyam., A.Vorobiev and S.Gevorgian., "Tunable Electromagnetic Bandgap Performance of Coplanar Waveguides Periodically Loaded By Ferroelectric Varactors," Microwave and Optical Tech. Lett., Vol.39., No.2., pp.no. 81-86, 2003.
- [30] S.Gevorgian., "Ferroelectrics in Microwave Devices, Circuits and Systems Physics, Modelling, Fabrication and Measurements" Springer.
- [31] B.Noren, "Thin Film Barium Strontium Titanate (BST) For a New Class of Tunable RF Components," Microwave Journal., Vol.47., pp.no.210-220., May 2004.
- [32] D. Ghosh, "Tunable Microwave Devices using BST and Base Metal Electrodes," PhD Dissertation, North Carolina State University, 2005.

- [33] W.P. Mason, "Electrostrictive Effect in Barium Titanate Ceramics," *Physical Review*, Vol. 74, pp.no. 1134-1147, 1948.
- [34] C.V. Varanasi., K.D.Leedy., D.H Tomich., G.Subramanyam., "Large Area $Ba_{1-x}Sr_xTiO_3$ Thin Films For Microwave Applications Deposited by Pulsed Laser Ablation," *Thin Solid Films*, Vol.517, pp.no 2878-2881, 2009.
- [35] Q. X. Jia., X. D. Wu., S. R. Foltyn., P. Tiwari., " Structural and Electrical Properties of $Ba_{0.5}Sr_{0.5}TiO_3$ Thin Films with Conductive $SrRuO_3$ Bottom Electrodes," *Appl. Phys. Lett.*, Vol-66, pp.no. 2197-2199, April 1995.
- [36] A. Kumar., S. G. Manavalan., "Characterization of barium strontium titanate thin films for tunable microwave and DRAM applications," *Surf. Coat. Technol.*, Vol-198, pp.no. 406-413, August 2005.
- [37] B.Acikel, "High Performance Barium Strontium Titanate Varactor Technology for Low Cost Circuit Applications," PhD Dissertation, University of California Santa Barbara, 2002.
- [38] R. Zhang., C. Yang., G. Ding., J. Feng., "Preparation and Characterization of $Ba_{1-x}Sr_xTiO_3$ Thin Films Deposited on Pt/SiO₂/Si by Sol-Gel method," *MRS Bull.*, Vol-40, No-9, pp.no.1490-1496, 2005.
- [39] S.Ketkar., "Synthesis, Characterization and Applications of Barium Strontium Titanate Thin Film Structures," PhD Dissertation, University of South Florida, 2013.
- [40] N. K. Pervez., P. J. Hansen., R. A. York., "High Tunability Barium Strontium Titanate Thin Films for RF Circuit Applications," *Appl. Phys. Lett.*, Vol-85, pp.no. 4451-4451, 2004.

- [41] P. Padmini., T. R. Taylor., M. J. Lefevre., A. S. Nagra., J. S. Speck., R. A. York., "Realization of High Tunability Barium Strontium Titanate Thin Films by RF Magnetron Sputtering", Appl. Phys. Lett., Vol-75, pp.no. 3186-3188, November 1999.
- [42] F.Benes., M.Dragomir., B.Malič., M.Deluca. "Chemical Solution Deposition of $Ba_xSr_{1-x}TiO_3$ Thin Films for Energy Storage Applications" Proceedings 56, pp.no. 1- 9, 2020.
- [43] C. Borderon, D. Averty, R. Seveno, H. W. Gundel., "Preparation and Characterization of Barium Strontium Titanate Thin Films by Chemical Solution Deposition" Ferroelectrics," Vol.362, pp.no.1-7, 2008.
- [44] C.J.G.Meyers., C.R.Freeze., S.Stemmer., R.A.York., " (Ba,Sr)TiO₃ Tunable Capacitors with RF Commutation Quality Factors Exceeding 6000," Appl. Phys. Lett., 2016.
- [45] G.Subramanyam., M.W.Cole., N.X.Sun., T.S.Kalkur., N.M.Sbrockey., G.S.Tompa., X.Guo., C.Chen., S.P.Alpay.,G.A.Rossetti., K.Dayal., L.Q.Chen., D.G.Schlom., "Challenges and Opportunities for Multi-Functional Oxide Thin Films for Voltage Tunable Radio Frequency/Microwave Components," Appl. Phys. Reviews.,pp.no1-35., 2013.
- [46] S.Wang, "Experimental Investigation of New Inductor Topologies," PhD Dissertation, University of Dayton, 2016.
- [47] T.M Shaw., Z.Suo., M.Huang., E. Liniger R.B. Laibowitz J.D.Baniecki, "The Effect of Stress on the Dielectric Properties of Barium Strontium Titanate Thin Films," Appl. Phys. Lett., Vol.75., No.14., pp.no. 2129-2131. October 1999.

- [48] A.Tombak., J.P.Maria., F.T. Ayguavives., Z.Jin., G.T.Stauf., A.I.Kingon., A.Mortazawi., "Voltage-Controlled RF Filters Employing Thin-Film Barium-Strontium-Titanate Tunable Capacitors," in IEEE Trans. on Micro. Theo. and Techn., Vol. 51, No. 2, pp.no 462-467, Feb. 2003.
- [49] T.S.Kalkur., N.Sbrockey., G.S.Tompa., M.W.Cole., "Tunable RF Filters Fabricated Using MOCVD Deposited Graded Composition BST Films", Integr. Ferroelectr., Vol.126, No.1, pp.no. 28-33, 2011.
- [50] T.S. Kalkur., N. Sbrockey., G.S. Tompa., J. Spanier., M. Alpay., M.W. Cole., "Low Voltage Tunable Band Pass Filter using Barium Strontium Titanate Parallel Plate Capacitors", Integr. Ferroelectr., Vol. 112, No.1, pp.no. 1-7, 2009.
- [51] V.Gurumurthy, "Barium Strontium Titanate Films for Tunable Microwave and Acoustic Wave Applications," MS Thesis, University of South Florida, 2007.
- [52] S. Gevorgian., A. Vorobiev., "Impact of the Electrodes on the Tunability of Paraelectric BST Film Based FBARs," 40th European Microwave Conference, pp.no. 1210-1213, 2010.
- [53] J. Berge., A. Vorobiev., W. Steichen., S. Gevorgian., "Tunable Solidly Mounted Thin Film Bulk Acoustic Resonators Based on $Ba_xSr_{1-x}TiO_3$ Films," IEEE Microw. Wirel. Compon. Lett., Vol.17, No.9, pp.no. 655-657, Sept. 2007.
- [54] A. Victor., J. Nath., D. Ghosh., B. Boyette., J.-P. Maria., M. B. Steer., A. I. Kingon., G. T. Stauf., "Noise Characteristics of an Oscillator with a Barium Strontium Titanate (BST) Varactor." IEEE Proc. Microwaves. Antennas & Propagation, pp.no. 96-102, Feb. 2006.

- [55] A. Jamil., T. S. Kalkur., N. Cramer., "Tunable ferroelectric capacitor-based voltage-controlled oscillator", IEEE Trans. Ultrason. Ferroelect. Freq. Control, Vol. 54, No. 2, pp.no. 222-226, Feb 2007.
- [56] M. Sazegar, Y. Zheng, H. Maune, C. Damm, X. Zhou and R. Jakoby, "Compact Tunable Phase Shifters on Screen-Printed BST for Balanced Phased Arrays," in IEEE Transactions on Microwave Theory and Techniques, Vol. 59, No. 12, pp.no. 3331-3337, Dec. 2011.
- [57] B. Acikel., Y.Liu., A.S.Nagra., T.R., Taylor., P.J.Hansen., J.S.Speck., R.A.York., "Phase shifters using (Ba,Sr)TiO₃ thin films on sapphire and glass substrates," 2001 IEEE MTT-S International Microwave Symposium Digest, Vol.2, pp.no. 1191-1194, 2001.
- [58] G. Subramanyam, F. Ahamed and R. Biggers, "A Si MMIC compatible ferroelectric varactor shunt switch for microwave applications," in IEEE Microwave and Wireless Components Letters, Vol. 15, No. 11, pp.no. 739-741, Nov. 2005.
- [59] N.E.Hinnawy., P.Borodulin., B.P.Wagner., M.R.King., E.B.Jones., R.S.Howell., M.J.Lee., R.M.Young., "Low-Loss Latching Microwave Switch using Thermally Pulsed Non-Volatile Chalcogenide Phase Change Materials," Applied Physics Letters, pp.no - 1-5, July 2014.
- [60] T.Ohta., " Phase-Change Optical Memory Promotes The DVD Optical Disk," J. of Optoelectronics and Adv. Materials., Vol.3, No.3., pp.no. 609-626, Sep. 2001.
- [61] S.Raoux., D.Lelmini., M.Wuttig., I.Karpov., "Phase Change Materials," MRS Bull., Vol.37, pp.no 118-123, 2012.

- [62] M.H.R.Lankhorst., B.W.S.M.M.Ketelaars., R.A.M.Wolters., "Low-Cost and Nanoscale Non-Volatile Memory Concept for Future Silicon Chips," Nature materials, Vol.4, pp.no 347-352, 2005.
- [63] G. W. Burr, M. J. Breitwisch, M. Franceschini, D. Garetto, K. Gopalakrishnan, B. Jackson, B. Kurdi, C. Lam, L. A. Lastras, A. Padilla, B. Rajendran, S. Raoux, R. Shenoy, "Phase Change Memory Technology," J.of Vac. Sci. and Tech. B, Vol.28, No.2, 2010.
- [64] M.Nardone., M.Simon., I.V.Karpov., V.G.Karpov, "Electrical Conduction in Chalcogenide Glassed of Phase Change Memory," J. of App. Phys. Vol.112, No.7, 2012.
- [65] F. Xiong, A. D. Liao, D. Estrada, E. Pop, "Low-Power Switching of Phase-Change Materials with Carbon Nanotube Electrodes," Science, Vol. 332, No. 6029, pp.no. 568-570, Apr. 2011.
- [66] C. J. Xue, G. Sun, Y. Zhang, J. J. Yang, Y. Chen, H. Li, "Emerging Non-Volatile Memories: Opportunities and Challenges," Proceedings of the Ninth IEEE/ACM/IFIP International Conference on Hardware/Software Codesign and System Synthesis, pp.no. 325-334, 2011.
- [67] S.R.Ovshinsky., "Reversible Electrical Switching Phenomena in Disordered Structures," Phys. Rev. Lett. Vol.21, No.20, pp.no 1450-1453, 1968.
- [68] M.Wuttig., N.Yamada., "Phase-Change Materials for Rewriteable Data Storage," Nature Materials, Vol.6. pp.no 824-832., 2007.

- [69] A. Velea., C.N. Borca., G.Socol., A.C. Galca., D. Grolimund., M. Popescu., J.A. van Bokhoven., "In-situ Crystallization of GeTe\GaSb Phase Change Memory Stacked Films," Journal of App. Phys., pp.no. 1-9, Dec 2014.
- [70] X.Sun., E.Thelander., J.W.Gerlach. U.Decker., B. Rauschenbach., "Crystallization Kinetics of GeTe Phase-Change Thin Films Grown by Pulsed Laser Deposition," J. of Phys. D: Appl. Phys., Vol.48., pp.no 1-6, 2015.
- [71] H.Lu., E.Thelander., J.W.Gerlach., D.Hirsch., U.Decker., B.Rauschenbach., "Ge₂Sb₂Te₅ Phase-Change Films on Polyimide Substrates by Pulsed Laser Deposition," App. Phys. Lett., Vol.101, No.3., 2012.
- [72] S.Raoux., B.Munoz., H.Y.Cheng., J.L.J.Sweet., "Phase Transitions in Ge-Te Phase Change Materials Studied by Time-Resolved X-Ray Diffraction," Appl. Phys. Lett., Vol. 95, No. 14., 2009.
- [73] X. Sun., E. Thelander., P.Lorenz., J.W.Gerlach., U.Decker., B.Rauschenbach., "Nanosecond Laser-Induced Phase Transitions in Pulsed Laser Deposition-Deposited GeTe Films," J. of App. Phy., pp.no-1-5., Oct 2014.
- [74] G.C.Sosso., G.Miceli., S.Caravati., F.Giberti., J.Behler., M.Bernasconi, " Fast Crystallization of the Phase Change Compound GeTe by Large-Scale Molecular Dynamics Simulations," J. Phys. Chem. Lett., 2013.
- [75] G.Bruns., P.Merkelbach., C.Schlockermann., M.Salinga., M.Wuttig., T.D.Happ., J.B.Philipp., M.Kund., "Nanosecond Switching in GeTe Phase Change Memory Cells," Appl. Phys. Lett., Vol.95, No.4, 2009.

- [76] S.Raoux., H.Y.Cheng., M.A.Caldwell., H.S.P.Wong., "Crystallization Times of Ge-Te Phase Change Materials as a Function of Composition," Appl. Phys. Lett. Vol.95., No.7., 2009.
- [77] T.Chattopadhyay., J.X.Boucherle., H.G.Vonschnering., "Neutron Diffraction Study on the Structural Phase Transition in GeTe," J. of Phys. C. Solid State Phys., 1987.
- [78] H. Jiang., K. Guo., H. Xu., Y. Xia., K. Jiang., F.Tang., J.Yin., Z. Liu., "Preparation and characterization of GeTe₄ thin films as a candidate for phase change memory applications," J.of App. Phys.,pp-no-1-3., March 2011.
- [79] T.Singh., R.R.Mansour., "Characterization of Phase Change Material Germanium Telluride for RF Switches," 48th European Microwave Conference, pp.no 475-478, Sept.2018.
- [80] K.H. Kim., Y.K. Kyoung., J.H. Lee., Y.N. Ham., S.J. Choi., "Evolution of the Structural and Electrical Properties of GeTe under Different Annealing Conditions," J. of Electronic Materials., Vol 24, no.1., pp.no. 78-82., 2013.
- [81] M.R.King., B.P.Wagner., E.B.Jones., N.E.Hinnawy., P.Borodulin., S.R. Mclaughlin., J.S. Mason. Jr., R.S. Howell., M.J. Lee and R.M. Young., "Development of Cap-free Sputtered GeTe Films for Inline Phase Change Switch based RF Circuits," J.Vac.Sci.Tech., pp.no. 1-5., June 2014.
- [82] A.C. Galca, F. Sava, I.D. Simandan, C. Bucur, V. Dumitru, C. Porosnicu, C. Mihai, A. Velea, "Structural and Optical Properties of Optimized Amorphous GeTe Films for Memory Applications," Journal of Non-Crystalline Solids, Vol. 499, pp.no. 1-7, 2018.

- [83] R.Y.Kim., H.G.Kim., "Structural Properties of Ge₂Sb₂Te₅ Thin Films by Metal Organic Chemical Vapor Deposition for Phase Change Memory Applications," App. Phys. Lett., Vol. 89, 2006.
- [84] R.Y.Kim., H.G.Kim., S.G.Yoon., "Characterization of Ge_{1-x}Te_x Chalcogenide Thin Films Deposited by MOCVD for Phase Change Memory Applications," J. of Electrochemical Soc., Vol. 155, No. 2, Dec 2007
- [85] P.S.Chen., W.J.Hunks., M.Stender., T.Chen., G.T.Stauf., C.Xu., J.F.Roeder., "CVD of Amorphous GeTe Thin Film," MRS Online Proceedings Library, 2007.
- [86] J.I.Lee., H.Park., S.L.Cho., Y.L.Park., B.J.Bae., J.H.Park., H.G.An., J.S.Bae., D.H.Ahn., Y.T.Kim., H.Horii., S.A.Song., J.C.Shin., S.O.Park., H.S.Kim., U.I.Chung., J.T.Moon., B.I.Ryu., "Highly Scalable Phase Change Memory with CVD GeSbTe for Sub 50nm Generation," 2007 IEEE Symposium on VLSI Tech., 2007.
- [87] N.E.Hinnawy., P.Borodulin., B.P.Wagner., M.R.King., J.S. Mason. Jr., E.B Jones., S.R. Mclaughlin., V.Veliadis., M.Snook., M.E. Sherwin., R.M. Young., M.J. Lee., "A Four-Terminal, Inline, Chalcogenide Phase-Change RF Switch using an Independent Resistive Heater for Thermal Actuation," IEEE Elec. Dev. Lett., Vol.34, no.10, pp.no. 1313-1315., Oct 2013.
- [88] R.M.Young., N.E.Hinnawy., P.Borodulin., B.P.Wagner., M.R.King., E.B Jones., R.S. Howell., M.J. Lee., "Thermal Analysis of an Indirectly Heat Pulse Non-Volatile Phase Change Material Microwave Switch," J. of App. Phys., pp-no-1-6., August 2014.

- [89] J.R.Creighton., W.G.Breiland., D.D.Koleske., G.Thaler., M.H.Crawford., "Emissivity-Correcting Mid-Infrared Pyrometry for Group – III Nitride MOCVD Temperature Measurement and Control," J. of Crystal Growth, Vol.310, pp.no 1062-1068, 2008.
- [90] M.Wang., F.Lin., M.R.Zadeh., "Need a Change? Try GeTe: A Reconfigurable Filter Using Germanium Telluride Phase Change RF Switches," IEEE Microwave Magazine, Vol. 17, No. 12, pp.no. 70-79, Dec. 2016,
- [91] M.R.Zadeh., M.Wang., "Advanced Reconfigurable RF/Microwave Electronics," IEEE Radio and Wireless Symposium, pp.no 13-15, 2017.
- [92] P.Mahanta., M.Munna., R.A.Coutu.Jr., "Performance Comparison of Phase Change Materials and Metal – Insulator Transition Materials for Direct Current and Radio Frequency Switching Applications," Technologies 6, Vol. 48, No. 2, 2018.
- [93] Y.Shim., G.Hummel., M.R.Zadeh., "RF Switches Using Phase Change Materials," IEEE 26th International Conference on Micro Electro Mechanical Systems (MEMS), pp.no. 237-240, 2013.
- [94] A.Ghalem., A.Hariri., C.Guines., D.Passerieux., L.Huitema., P.Bolndy., A.Crunteanu., "Arrays of GeTe Electrically Activated RF Switches," IEEE MTT-S Int. Microw. Work. Series on Adv. Mat. and Proc. for RF and THz Appl., pp.no 1-3, 2017.
- [95] N.E.Hinnawy., P.Borodulin., B.P.Wagner., M.R.King., J.S.Mason., E.B.Jones., V.Veliadis., R.S.Howell., R.M.Young., M.J.Lee., "A 7.3 THz Cut-Off Frequency, Inline, Chalcogenide Phase-Change RF Switch Using and Independent Resistive Heater for Thermal Actuation," IEEE Comp. Semi. Int. Cir. Symp. (CSICS), 2013.

- [96] M.Wang, Y.Shim and M.R.Zadeh, "A Low-Loss Directly Heated Two-Port RF Phase Change Switch," in IEEE Electron Device Letters, Vol. 35, No. 4, pp.no 491-493, April 2014.
- [97] M.Wang and M.R.Zadeh, "Directly Heated Four-Terminal Phase Change Switches," 2014 IEEE MTT-S International Microwave Symposium, pp. 1-4, 2014.
- [98] J.S.Moon., H.C. Seo., D.Le., "Development Toward High-Power Sub-1-Ohm DC-67 GHz RF Switches using Phase Change Materials for Reconfigurable RF Front-End," IEEE MTT-S IMS, pp.no 1-3., 2014.
- [99] J.S.Moon., H.C.Seo., D.Le., H.Fung., A.Schmitz., T.Oh., S.Kim., K.A.Son., D.Zehnder., B.Yang., " 11 THz Figure-of-Merit Phase Change RF Switches for Reconfigurable Wireless Front-Ends," IEEE MTT-S IMS, pp.no 1-4, 2015.
- [100] T.Singh., R.R.Mansour., "Reconfigurable PCM GeTe Based Latching 6-Bit Digital Switches Capacitor Bank," 15th European Microwave Integrated Circuits Conf., pp.no 93-96., 2021.
- [101] L.Li., "Experimental Investigation of Integrated Tunable Passive Microwave Devices," PhD Dissertation University of Dayton, 2020.
- [102] N.Hosseinzadeh., J.F.Buckwalter., " A Compact, 37% Fractional Bandwidth Millimeter-Wave Phase Shifter Using a Wideband Lange Coupler for 60-GHz and E-Band Systems," IEEE CSICS, pp.no. 1-4, 2017.
- [103] R.Platonov., A.Altynnikov., A.Kozyrev., "A Tunable Beamforming Ferroelectric Lens for Millimeter Wavelength Ranges," Coatings, Vol.10, No.2, 2020.

- [104] K.Marubishi., H.Mizutani., K.Ohata., "Design and Performance of a Ka-band Monolithic Phase Shifter Utilizing Nonresonant FET Switches," IEEE Transaction on Microwave Theory and Techniques, Aug. 2000.
- [105] F. Ellinger., H.Jackel., W.Bachtold., "Varactor-Loaded Transmission-Line Phase Shifter at C-Band Using Lumped Elements," IEEE Transaction on Microwave Theory and Techniques, Apr. 2003.
- [106] F. Ellinger., R.Vogt., W.Bachtold., "Ultracompact Reflective-Type Phase Shifter MMIC at C-Band with 360° Phase-Control Range for Smart Antenna Combining," IEEE Journal of Solid-State Circuits, Vol. 37, No. 4, pp.no 481–486, Apr. 2002.
- [107] C. F. Campbell., S.A.Brown., "A Compact 5-Bit Phase-Shifter MMIC for K-Band Satellite Communication Systems," IEEE Transaction on Microwave Theory and Techniques, Vol. 48, No.12, pp.no 2652–2656, Dec. 2000.
- [108] D.W.Kang., S.Hong., "A 4-bit CMOS Phase Shifter Using Distributed Active Switches," IEEE Transaction on Microwave Theory and Techniques, Vol. 55, No. 7, July 2007.
- [109] B.W.Min, and G.M.Rebeiz, "Ka-Band BiCMOS 4-Bit Phase Shifter with Integrated LNA for Phased Array T/R Modules," IEEE/MTT-S Int. Microwave Symp., pp.no. 479–482, June 2007.
- [110] T. Singh and R. R. Mansour, "Loss Compensated PCM GeTe-Based Latching Wideband 3-bit Switched True-Time-Delay Phase Shifters for mmWave Phased Arrays," in IEEE Transactions on Microwave Theory and Techniques, Vol. 68, No. 9, pp.no. 3745-3755, Sept. 2020,

- [111] [W. Lee., S. Hong, "Ka-band inductor-shared SPnT DPnT switches and their applications to TTD phase shifter," IEEE Trans. Microw. Theory Techn., Vol. 67, No. 7, pp.no. 2546–2554, Jul. 2019.
- [112] T. Singh, N. K. Khaira and R. R. Mansour, "Thermally Actuated SOI RF MEMS-Based Fully Integrated Passive Reflective-Type Analog Phase Shifter for mmWave Applications," IEEE Transactions on Microwave Theory and Techniques, Vol. 69, No. 1, pp.no 119-131, Jan. 2021.
- [113] A.K.S.A.Aziz., M.B.Kassem., R.R.Mansour, "Design and Characterization of Compact Digital RF MEMS Capacitors and Phase Shifters in CMOS 0.35 μm Technology," J. Micromech. Microeng. Vol. 30., No. 4, 2020.
- [114] S. Abdulazhanov, Q. H. Le, D. K. Huynh, D. Wang, G. Gerlach and T. Kampf, "A mmWave Phase Shifter Based on Ferroelectric Hafnium Zirconium Oxide Varactors," IEEE MTT-S International Microwave Workshop Series on Advanced Materials and Processes for RF and THz Applications (IMWS-AMP), pp.no 175-177, 2019.
- [115] D. Mercier., A.N.Martin., H.Sibuet., C.Baret., J.Chautagnat., C.Dieppedale., C.Bonnard., J.Guillaume., G.Le.Rhun., C.Billard., P.Gardes., P.Poveda., "X Band Distributed Phase Shifter Based on Sol-Gel BCTZ Varactors," European Radar Conference (EURAD), pp.no 382-385, 2017.
- [116] M.B.Kassem., R.R.Mansour., S.S.Naeini., "A Novel Latching RF MEMS Phase Shifter," 44th European Microwave Conference, pp.no 1612-1615, 2014.
- [117] S. Kumar, A. Govil, A. Bhattacharyya., D. Dutta, "A Wide-Range Tunable Bandpass Filter cum Sinusoidal Oscillator using a New Current-Controlled

Resistor," IEEE International Symposium on Circuits and Systems (ISCAS), Vol.2, pp.no. 220-223,1999.

[118] G. Leuzzi, V. Stornelli, S. Del Re, L. Pantoli, "High Quality Factor Integrable Bandpass Filter by using Tunable Active Inductor," Workshop on Integrated Nonlinear Microwave and Millimetre-Wave Circuits, pp.no. 1-4, 2011.

[119] V. Radisic, Y.Qian, R. Cocciolo, T. Itoh, " Novel 2-D Photonic Bandgap Structure for Microstrip Lines." IEEE Microwave Guide Wave Lett., Vol. 8, pp.no. 69-71, Feb. 1998.

[120] E. Yablonovitch., "Photonic Band-Gap Structure," J. Opt. Soc. Amer. B. Opt. Phys., Vol. 10, pp.no. 283-295, Feb. 1993.

[121] Y. Qain, F.R. Yang, T. Itoh, "Characteristics of Microstrip Lines on a Uniplanar Compact PBG ground plane," Asia- Pacific Microwave Conf. Dig., pp.no. 589-592. Dec. 1998.

[122] Y. Qain, T. Itoh, "Planar Periodic Structures for Microwave and Millimeter Wave Circuit Applications," in IEEE MTT-S Int. Microwave Symp. Dig., pp.no. 1533-1536. June 1999.

[123] Y. Qian, V. Radisic., T. Itoh, "Simulation and Experiment of Photonic Band-Gap Structures for Microstrip Circuits," Proceedings of 1997 Asia-Pacific Microwave Conference, Vol. 2, pp.no. 585-588, 1997.

[124] L. H. Weng, Y. C. Guo, X.W. Shi, X. Q. Chen., "An Overview on Defected Ground Structure," Progress in Electromagnetic Research B, Vol.7, pp.no. 173-189, 2008.

- [125] D. Ahn, J. Park, C. Kim, J. Kim, Y. Qian., T. Itoh, "A Design of the Low-Pass Filter using the Novel Microstrip Defected Ground Structure," in IEEE Transactions on Microwave Theory and Techniques, Vol. 49, No. 1, pp.no. 86-93, Jan. 2001.
- [126] K.Annam., S.K.Khah., S.Dooley., C.Cerny., G.Subramanyam., "Experimental Design of Bandstop Filters Based on Unconventional Defected Ground Structures," Microwave and Optical Technology Lett., Vol. 58, No. 12, pp.no. 2969-2973., Dec. 2016.
- [127] K. Annam., "Design of Bandstop Filters Using Defected Ground Structures," MS thesis, University of Dayton, 2015.
- [128] H. Yue., "Reconfigurable Passive RF/Microwave Components," PhD Dissertation, University of Dayton, 2016.
- [129] D.J. Woo, T.K. Lee, J.W.Lee, C.S.Pyo and W.K.Choi, "Novel U-slot and V-slot DGSs for Bandstop Filter with Improved Q factor," in IEEE Transactions on Microwave Theory and Techniques, Vol. 54, No. 6, pp.no. 2840-2847, June 2006.